Electrical-Thermal Energy Transfer and Energy Conversion in Semiconductor Nanowires

SHI LIHONG

(M.Sc., Soochow University,P.R. China)

A THESIS SUBMITTED

FOR THE DEGREE OF DOCTOR OF PHILOSOPHY

DEPARTMENT OF PHYSICS

NATIONAL UNIVERSITY OF SINGAPORE

2011

I would like to dedicate this doctoral dissertation to my parents. They gave me inexhaustible encourage and help when I am in trouble. Although my mother has no opportunity to receive higher education; however, she makes her best effort to support me to realize my dream. My father always supports me quietly when I face big troubles.

Acknowledgements

I am most indebted to my supervisor Professor Li Baowen and co-supervisor Professor Zhang Gang, for their invaluable advices, patience, kindness and encouragement throughout my Ph.D. candidature. I cannot grow up to be an independent researcher without their help. Professor Li provided me good guidance in my research topic and he is also very concerned about my life especially when I am in trouble.

Professor Zhang took care more of the details of my research works, such as research idea, numerical methods. His earnest, preciseness and brightness give me a deep impression and light my passion of research intrest. He gives me a lot of help when I am at loss in the research road.

I would also like to express my appreciation to Prof. Wang Jian-Sheng for his help in my module.

Meanwhile, I would like to thank my seniors Dr. Li Nianbei, Dr. Yang Nuo, Dr Wu Xiang, Mr. Yao DongLai, and my group members, Mr Ren Jie, Mr Chen Jie, Mr Zhang Lifa, Ms Zhang Kaiwen, Ms Ni Xiaoxi, Mr Zhang Xun, Ms Ma

Jing, Ms Zhu GuiMei, Mr Feng Ling and all members in Prof. Li Baowen research group. I cannot enjoy myself so much in the past four fruitful years of my Ph. D. life without them.

Finally I would like to express my deepest thankfulness to my father and mother. They are always there to encourage me whenever I was trapped in trough, and ask me to remain humble when I am faced by a contemporary success. I cannot express more of gratitude to my parents who always keep the greatest faith in me.

Table of Contents

Acknowledgements ii

Abstract vii

Publications xi

List of Tables xii

List of Figures xiii

1 Introduction 1

1.1 General Description of Seebeck Effect and Peltier Effect 1

1.2 General Description of Thermoelectric Figure of Merit ZT 4

1.3 Methods to Improve The Thermoelectric Figure of Merit ZT . . . 6

1.3.1 Reduction of Thermal Conductivity 6

1.3.2 Improvement of Thermal Power Factor 11

1.4 Thermoelectric Figure of Merit ZT in Nanostructured Systems . . 16

1.4.1 ZT in Nanowires and Superlattices 16

1.4.2 ZT in Nanocomposites 18

1.5 Outline of Thesis 21

2 Theoretical Models and Numerical Methods 23

2.1 Boltzmann Transport Equation 24

2.2 Semiclassical Ballistic Transport Equation 28

2.3 Density Functional Theory 29

3 Thermoelectric Figure of Merit in [110]Si NWs, [110]$Si_{1-x}Ge_x$ NWs and [0001] ZnO Nanowires 33

3.1 Introduction 35

3.2 Computation Methods 39

3.3 Size Dependent Thermoelectric Properties of Silicon Nanowires . . . 40

3.4 Large Thermoelectric Figure of Merit in $Si_{1-x}Ge_x$ Nanowires 49

3.5 Impacts of Phase Transition on Thermoelectric Figure of Merit in [0001] ZnO Nanowires 57

3.6 Thermoelectric Figure of Merit in Ga-Doped [0001]ZnO Nanowires . 65

4 Significant Enhancement of Thermoelectric Figure of Merit in [001] $Si_{0.5}Ge_{0.5}$ Superlattice Nanowires 77

4.1 Introduction 78

4.2 Computation Methods 80

4.2.1 Results and Discussion 83

4.2.2 Summary 100

5 Conclusions and Outlook 102

5.1 Conclusive Remarks 103

5.2 Outlook to Future Research Perspective 106

5.2.1 The Phonon-Drag Effect on Thermoelectric Figure of Merit in Semiconductor Nanowires 107

Bibliography **109**

Abstract

Thermoelectric phenomena, Seebeck effect, Peliter effect and Thomas effect, involve the conversion between the thermal energy and electrical energy. The thermoelectric materials play an important role in solving the energy crisis. The performance of the thermoelectric materials is evaluated by the thermoelectric figure of merit ZT(=$S^2\sigma/\kappa\ T$), here S is the Seebeck coefficient, σ is the electrical conductivity, κ is the thermal conductivity, where κ_e and κ_{ph} are the electronic and phonon contribution to the thermal conductivity, respectively; T is the absolute temperature.

Recent advances in semiconductor nanowires have provided a new path to improve the thermoelectric performance. In this thesis, we firstly combine the Boltzmann Transport Theory and the first principle method to investigate the size dependence of thermoelectric properties of silicon nanowires (SiNWs). With cross section area increasing, the electrical conductivity increases slowly, while the Seebeck coefficient reduces remarkably. This leads to a quick reduction of cooling power factor with diameter. Moreover, the figure of merit also decreases with transverse size. Our results demonstrate that in thermoelectric application, NW with small diameter is preferred.We also predict that isotopic doping can increase the value of ZT

significantly. With 50% ^{29}Si doping ($^{28}Si_{0.5}{}^{29}Si_{0.5}$ NW), the ZT can be increased by 31%.

Besides the Si NWs, we also use first-principles electronic structure calculation and Boltzmann transport equation to investigate composition effects on the thermoelectric properties of silicon-germanium $Si_{1-x}Ge_x$ NWs. The power factor and figure of merit in n-type $Si_{1-x}Ge_x$ wires are much larger than those in their p-type counterparts with the same Ge content and doping concentration. Moreover, the maximal obtainable figure of merit can be increased by a factor of 4.3 in n-type $Si_{0.5}Ge_{0.5}$ NWs, compared with the corresponding values in pure silicon nanowires (SiNWs). Given the fact that the measured ZT of n-type SiNW is $0.6 - 1.0$, we expect ZT value of n-type $Si_{1-x}Ge_x$ NWs to be $2.5 - 4.0$.

Recently, Znic Oxide (ZnO) nanowires (NWs) have shown promise for nanodevice applications. However, rare researches are concerning about the thermoelectric properties of ZnO wires. In this thesis, we use the first-principle electronic structure calculation and Boltzmann transport equation to investigate the impacts of phase transition and Gallium (Ga) doping on the thermoelectric properties of [0001] ZnO NWs. The phase transition has played an important role in electronic conduction and thermal conduction in ZnO NWs, but this effect on thermoelectric is still unclear. Our results show that the electronic band gap of ZnO NWs for Wurtzite (W) phase is larger than that of Hexagonal (H) phase. For a certain carrier concentration, the Seebeck coefficient S for W-phase is larger than that for H-phase, while electrical conductivity with H-Phase is much higher than that of W-Phase because of the higher electron mobility in H-Phase. There is an optimal carrier concentration to achieve the maximum value of power factor P for both W and H

phases. The maximum value of P (P_{max}) for H phase ($P_{max} = 1638\mu W/m - K^2$) is larger than that of W phase ($P_{max} = 1213\mu W/m - K^2$) due to its high electrical conductivity. Provided that the thermal conductivity for H phase is about 20% larger than that for W phase, the maximum achievable value of figure of merit ZT for H phase is larger than that for W phase (1.1 times).

We also study the impact of the Ga doping effect on the thermoelectric properties of [0001] ZnO NWs. Our results show that the thermoelectric performance of the Ga-doped ZnO ($Zn_{1-x}Ga_xO$) NWs is strongly dependent on the Ga contents. The maximum achieved room-temperature thermoelectric figure of merit in $Zn_{1-x}Ga_xO$ can be increased by a factor 2.5 at Ga content is 0.04, compared with the corresponding pure ZnO wires.

Finally, we investigate the thermoelectric figure of merit in [001] $Si_{0.5}Ge_{0.5}$ superlattice (SL) nanowires (NWs). In this work, we combine the charge transport and the phonon transport to study the interface effect on the thermoelectric properties of this SL NWs. For the charge transport, we use *Transiesta* package, which is based on the Density Functional Theory (DFT) and nonequilibrium Green's Functions (NEGF) to calculate the charge transmission across the SL NWs; For the phonon transport, we use the DFT, which is implemented by the *Siesta* package, to obtain the force-constant matrix. We use the nonequilibrium Green's Functions (NEGF) to calculate the phonon transmission in this SL NWs. Our results show that the maximum values of power factor and thermoelectric figure of merit in n-type $Si_{0.5}Ge_{0.5}$ wires are larger than those in p-type counterparts with the same period length. Furthermore, the largest values of ZT ($(ZT)_{max}$)achieved in n-type $Si_{0.5}Ge_{0.5}$ wires is 4.7 at the period length is $0.54nm$, which is 5.0 times larger than

that in n-type pure Si NWs ($ZT = 0.94$), while $(ZT)_{max}$ for p-type wires is 2.7 at the same period length, which is 4.5 times larger than that of p-type pure Si NWs ($ZT = 0.6$).

Publications

[1]: Lihong. Shi, Donglai. Yao, Gang Zhang,and Baowen Li, "Size Dependent Thermoelectric Properties of Silicon Nanowires", *Appl. Phys. Lett.*, **95**, 063102(2009).

[2]: Lihong Shi,Donglai. Yao, Gang Zhang, and Baowen Li, "Large Thermoelectric figure of merit in Si1-xGex nanowires", *Appl. Phys. Lett.*, **96**, 173108 (2010).

[3]:Lihong Shi, Jie Chen, Gang Zhang, and Baowen Li, "Thermoelectric figure of merit in [0001] Ga-doped ZnO nanowires", Physics Letters A **376** (2012) 978 − 981.

[4]:Lihong Shi, Jinwu Jiang, Gang Zhang, and Baowen Li, "High Thermoelectric figure of merit in SiGe Superlattice Structured Nanowires, ", Nano Letters revising (2012).

[5]Lihong Shi, Lei Gao, " Subwavelength imaging from a multilayered structure containing interleaved nonspherical metal-dielectric composites " ,*Phys. Rev. B* **77**, 195121 (2008).

[6]Lihong Shi, Lei Gao, Sailing He and Baowen Li," Superlens from metal-dielectric composites of nonspherical particles ",*Phys. Rev. B*, **76**, 045116 (2007)

List of Tables

3.1 The charge mobility in $Si_{1-x}Ge_x$ alloys ($n = 1.2 \times 10^{20} cm^{-3}$) for different Ge content x. The mobility values are calculated from Ref.[67] 54

List of Figures

1.1 (a) Schematic of thermoelectric power generation; (b) a typical thermoelectric device; and (c) an example demonstration of thermoelectric power generation. 3

1.2 History of the improvement of thermoelectric figure of merit, ZT, at $300K$. (from Ref [6]) 5

1.3 Measured thermal conductivity of different diameter Si nanowires. 7

1.4 Thermal conductivity of SiNWs versus the percentage of randomly doping isotope atoms at $300K$. SiNWs are along the (100) direction with cross sections of (3×3) unit cells (lattice constant is $0.543nm$). The results, by the $Nosé - Hoover$, method coincide with those by Langevin methods indicating that the conclusions are independent of the heat bath used. 9

1.5 Thermal conductivity of the superlattice SiNWs versus the period length at $300K$. SiNWs are along the (100) direction with cross sections of (3×3) unit cells (lattice constant is $0.543nm$). 10

1.6 Thermopower calculation plotted along with experimental data (black points) from a 20-nm-wide Si nanowire p-type doped at $3\times10^{19}(cm^{-3})$. 13

1.7 Calculated normalized Seebeck distribution versus energy for heavily doped bulk n-type $Si_{80}Ge_{20}$. Low energy electrons reduce the total Seebeck coefficient. 13
1.8 Schematic of the effect of a resonant level on the electronic density of states (DOS). 15
1.9 Temperature dependence of ZT of $10\AA/50\AA$ p-type Bi_2Te_3/Sb_2Te_3 superlattice compared to those of several recently reported materials 17
1.10 Low (a) and high (b) magnification TEM images of the hot pressed nanostructured $Si_{95}Ge_5$ sample. 19

3.1 (a) σ vs cross sectional area with different carrier concentration. (b) S vs cross sectional area with different carrier concentration. (c)σ vs carrier concentration with fixed cross section area of $1.1nm^2$. (d) S vs carrier concentration with fixed area of $1.1nm^2$. 43
3.2 DOS for SiNWs with three different transverse dimensions from 1.1 to $17.8nm^2$. The red dotted lines are drawn to guide the eyes. . . . 44
3.3 (a) Thermal power factor of SiNW vs carrier concentration with three different transverse dimensions. (b) Maximum power factor vs cross sectional area. (c) N_{max} vs cross sectional area. (d) Size dependence of the maximum room temperature cooling power density of SiNW with length of $1\mu m$. 45

3.4 (a) Thermal conductivity due to electrons vs carrier concentration for SiNWs with different transverse dimensions. (b) ZT vs carrier concentration for different isotope-doped SiNWs ($^{28}Si^{29}_{1-x}Si_x$ NWs) with fixed cross section area of $2.3nm^2$. (c) ZT_{max} vs the concentration of ^{29}Si atom. (d) N_{max} vs the concentration of ^{29}Si doping atom. 46
3.5 The electronic band gap shift for $Si_{1-x}Ge_x$ NWs vs Ge contents x from 0 to 1. 51
3.6 σ vs Ge content x with different carrier concentration for n-type and p-type wires(a);S vs Ge content with different carrier concentration for n-type and p-type wires (b). 52
3.7 Thermal power factors of $Si_{1-x}Ge_x$ NWs vs carrier concentration with three different Ge contents for n-type and p-type wires (a). Maximum power factors vs Ge content for n-type and p-type wires (b) 53
3.8 $ZT_{Si_{1-x}Ge_x}/ZT_{Si}$ vs the Ge content x for n-type $Si_{1-x}Ge_x$ wires. . 56
3.9 The geometry for the optimized ZnO nanowires with four different diameters for both W phase and H phase (top view and side view);Red: O atom; Gray: Zn atom. 59
3.10 The electronic band gap for wire A, B, C,D for both W phase and H phase. 60
3.11 σ vs n_e (a); S vs n_e (b)for both W phase and H phase. 61
3.12 The electronic band structure for W phase (a)and H phase (b). (Dashed line for Fermi energy level.) 62

3.13 The power factor vs carrier concentration (n_e) for both W phase (solid line) and H phase (dashed line) (a); The relative value of ZT(H)/ZT(W) vs carrier concentration (n_e)(b) 63
3.14 The atomic structure of ZnO nanowires with diameter of $0.7nm$;(a)is top view and (b)is side view;Red: O atom; Gray: Zn atom. 67
3.15 The total DOS for $Zn_{1-x}Ga_xO$ NWs for (a) $x = 0$;(b)0.04;(c) 0.08. The Fermi energy is set to 0. The dashed magenta line is used to guide the eyes. 68
3.16 The averaged electronic band gap for $Zn_{1-x}Ga_xO$ NWs and carrier concentration versus Ga contents. 69
3.17 σ , S vs Ga content x. 70
3.18 Thermal power factor of $Zn_{1-x}Ga_xO$ NWs versus Ga contents. . . 71
3.19 Relative value of phonon Thermal conductivity for $Zn_{1-x}Ga_xO$ NWs compared with that for pure ZnO wires versus doping contents. 72
3.20 Relative value of ZT for $Zn_{1-x}Ga_xO$ NWs compared with that for pure ZnO wires versus the Ga content 73

4.1 The geometry of the $Si_{0.5}Ge_{0.5}$ superlattice nanowires with the period length $L = 1.08nm$; Yellow:Si atom; Green:Ge atom; White:H atom. 83
4.2 Hole transmission for the $Si_{0.5}Ge_{0.5}$ superlattice(SL) nanowires(NWs). The energy scale is relative to the valence band edge. 85
4.3 Electron transmission for the $Si_{0.5}Ge_{0.5}$ superlattice(SL) nanowires(NWs) and pure Si NWs. The energy scale is relative to the conduction band edge. 86

4.4 Projected density of states (PDOS) on Si and Ge atoms for the p-type SL NWs.The energy scale is relative to the valence band edge. 87
4.5 Projected density of states (PDOS) on Si and Ge atoms for the n-type SL NWs.The energy scale is relative to the conduction band edge. 88
4.6 Hole conductance for SL NWs and pure Si NWs.The energy scale is relative to the valence band edge. 89
4.7 Electronic conductance for SL NWs and pure Si NWs. The energy scale is relative to the conduction band edge. 90
4.8 Seebeck coefficient of holes in the valence band for both SL NWs and pure Si NWs. The energy scale is relative to the valence band edge. 91
4.9 Seebeck coefficient of electrons in the conduction band for both SL NWs and pure Si NWs. The energy scale is relative to the conduction band edge. 92
4.10 Thermal power factor versus energy in the valence band. The energy scale is relative to the valence band edge. 93
4.11 Thermal power factor versus energy in the conduction band. The energy scale is relative to the conduction band edge. 94
4.12 P_{max} versus period length L for SL NWs. 95
4.13 λ_p and λ_e versus period length L for SL NWs. 97
4.14 ZT versus energy μ for both SL NWs and Si NWs. 98
4.15 The maximum values of ZT (ZT_{max}) versus period length L 99

Chapter 1

Introduction

1.1 General Description of Seebeck Effect and Peltier Effect

The energy crisis that fossil fuel supplies decrease and the world demand increases will become a major society problem in the $21st$ century. Thermoelectric phenomena involve the conversion between the thermal energy and electrical energy and provide a method for heating and cooling materials. Thermoelectric materials are able to convert the heat into electricity, which is based on the Seebeck effect. The Seebeck effect is discovered by Thomas Johann Seebeck in 1821. The phenomenon of the Seebeck effect can be explained as follows: when a temperature gradient is applied to a material, the charge carriers (electrons or holes) at the hot side have

more thermal energy than those at the cold side. They will diffuse from the hot side to the cold side. In the end, there are more carriers at the cold side than those at the hot side, and the inhomogeneous charge distribution causes an opposite electric field to the diffusion direction. When the rate at which carriers move from the hot side to the cold side is balanced by the rate at which the carriers move from the cold side to the hot side due to the induced electric field, the equilibrium is reached and the electrochemical is formed according to a temperature gradient. This electrochemical is known as the Seebeck voltage and the Seebeck coefficient is defined as the amount of the voltage generated per unit temperature gradient ($S = \frac{\triangle V}{\nabla T}$, S is the Seeebck coefficient; $\triangle V$ is the Seebeck voltage;∇T is the temperature gradient). When the material is connected to a circuit, the electrochemical potential will drive a current to perform the electrical work, which is called thermoelectric power generation [1–3] (See Figure 1.1).

The thermoelectric device is shown in Figure 1.1. For these devices, there are many legs of alternating n-type and p-type materials, which allow a current to flow through each leg sequentially while heat flows through each leg in parallel. The commercial thermoelectric module is shown in Figure 1.1. For the power applications, the modules will be subjected to the temperature difference using a flame as a heat source and a large aluminum block as the cold side heat sink. This temperature gradient will create an electrochemical potential difference between the hot side and the cold side of the thermoelectric material which drives a current around the circuit, lighting up the LEDs.

Thermoelectric materials are also capable of converting the electricity into heat, which is called the Peltier effect, which is discovered by Jean-Charles Peltier in

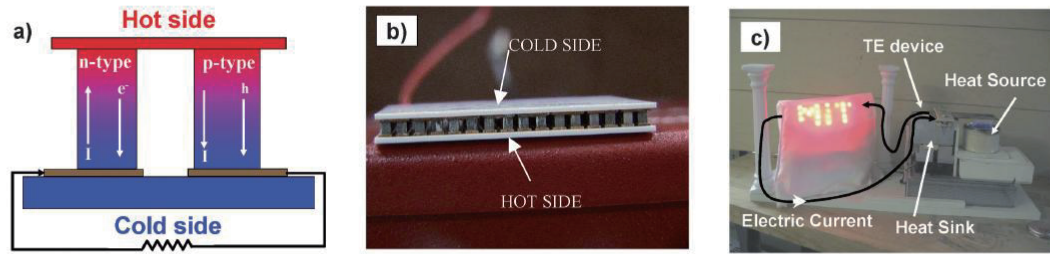

Figure 1.1: (a) Schematic of thermoelectric power generation; (b) a typical thermoelectric device; and (c) an example demonstration of thermoelectric power generation.(from Ref [3])

1834. For the Peltier effect, the heat is absorbed or emitted at the interfaces of the materials when the current is across a circuit. The Peltier coefficient is related to the Seebeck coefficient and is defined as the amount of the thermal energy is carried by per charge ($\Pi = S \times T$, Π is the Peltier coefficient; S is the Seebeck coefficient; T is absolute temperature.). Whether the heat is absorbed or emitted depends on the sign of the difference between the Peltier coefficients and the direction of the current. If the current is in one direction, the junction will exact heat [1–3], which can produce the thermoelectric refrigeration; If the current is in the other direction, the junction will absorb heat, which can act as a heat jump.

1.2 General Description of Thermoelectric Figure of Merit ZT

Thermoelectric materials are defined as these materials that are able to generate the power using the Seebeck effect or refrigerate using the Peltier effect. The performance of the thermoelectric materials is characterized by the figure of merit ZT ($= S^2\sigma/\kappa T$)[4], here S is the Seebeck coefficient, σ is the electrical conductivity and κ is the thermal conductivity, where κ_e and κ_{ph} are the electronic and phonon contribution to the thermal conductivity, respectively; T is the absolute temperature [5]. ZT can be increased by increasing the power factor or decreasing κ. However, in conventional materials, it is difficult to improve ZT. First, a simple increase in S for general materials will lead to a simultaneous decrease in σ. Also, an increase in σ leads to a comparable increase in the electronic contribution to κ [3]. Therefore, over the 3 decades, from the $1960s - 1990s$, the value of ZT could not be increased significantly and the best thermoelectric materials are Bi_2Te_3 and its alloy family with $ZT = 1.0$. There has been no breakthrough in the increase of ZT until the year 2000 [6] (See Figure 1.2). From the year 2000, the large value of ZT is achieved in nanoscaled materials, such as nanowires, thin films, superlattices and so on. Why these nanoscaled materials can have large ZT ? The reasons are: firstly, many interfaces are introduced in these nanoscaled materials and these interfaces are able to scatter phonons more effectively than electrons; Secondly, the Seebeck coefficient S and electrical conductivity σ can be increased independently in those materials.

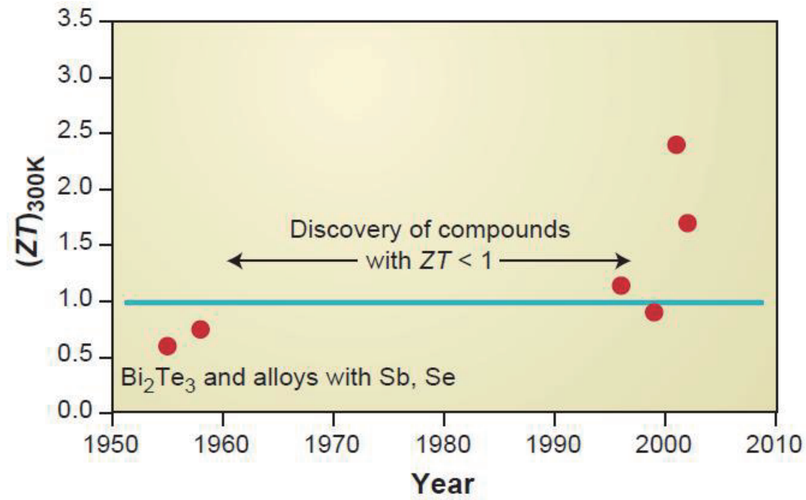

Figure 1.2: History of the improvement of thermoelectric figure of merit, ZT, at $300K$. (from Ref [6])

During a very long period, many research groups have made considerable effort to improve the thermoelectric efficiency of materials. In general, there are two important methods to improve the value of ZT. The first convention way is to reduce the thermal conductivity of the materials while the electrical properties are not affected. This method has been widely used in recent years. For example, using the nanoscaled materials is the typical way to reduce the thermal conductivity and thus increasing the value of ZT. The electrical properties in nanoscaled materails always remain unchanged compared with their bulk materials. The other way is to increase the thermal power factor with reducing the thermal conductivity. In some particular nanoscaled materials, the improvement of power factor has also been found. In the following, we will give a detailed introduction of these two methods.

1.3 Methods to Improve The Thermoelectric Figure of Merit ZT

1.3.1 Reduction of Thermal Conductivity

In the above sections, it is mentioned that an alternative way to increase ZT is to reduce the thermal conductivity without affecting electronic property. Moreover, ultra-low thermal conductivity is also required to prevent the back-flow of heat from the hot end to the cool end. Therefore, the reduction of thermal conductivity is crucial in thermoelectric applications. Due to the size effects and the high surface to volume ratio, the thermal properties of nanostructured materials are very different from that of the bulk materials. Volz and Chen investigated the thermal conductivity of silicon nanowires based on molecular dynamic simulations using the Green-Kubo method, and they found that thermal conductivity of individual silicon nanowires is more than 2 orders of magnitude lower than the bulk value [7, 8]. Li *et al.* have also reported a significant reduction of thermal conductivity in silicon nanowires compared to the thermal conductivity in bulk silicon experimentally [9]. This is due to the following facts. Firstly, the low frequency phonons, whose wavelengths are longer than the length of a nanowire, cannot survive in nanowires. Therefore, the low frequency contribution to thermal conductivity, which is very substantial and significant in bulk material, is largely reduced. Secondly, due to the large surface to volume ratio, boundary scattering in quasi-1D structures is also significant. More experimental and theoretical activities have been inspired to

explore this direction, including the theoretical prediction of the thermal conductivity of Ge nanowires [10], molecular dynamics simulation of nanofilms,[11]and experimental measurement of the thermal conductivity of $Si/SiGe$ superlattice nanowires.[12]. Liang and Li [92] have proposed an analytical formula including surface scattering and the size confinement effects of phonon transport to describe the size dependence of thermal conductivity in NWs and other nanoscale structures. In recent experiments,[14, 15] Hochbaum and Boukai have reported that large thermoelectric figure of merit has been achieved in SiNWs, which is about a 100-fold improvement over the value of bulk silicon. Moreover, Donadio and Galli [16] have investigated heat transport in SiNWs systematically, by using molecular dynamics simulation, lattice dynamics, and Boltzmann transport equation calculations.

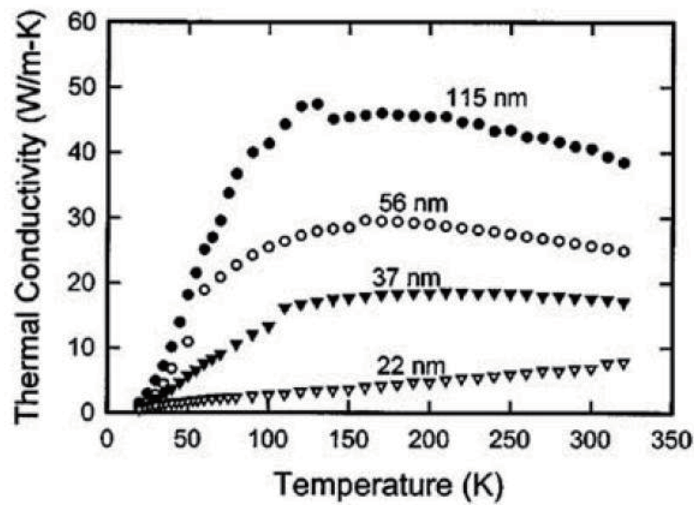

Figure 1.3: Measured thermal conductivity of different diameter Si nanowires.(from Ref [12])

The low thermal conductivity in nanostructures has attracted much attention due to its good thermoelectric applications. In order to achieve better thermoelectric

performance, further reduction of the thermal conductivity in nanostructures is the key point. Although the thermal conductivity of Si NWs is lower than that of bulk Si, it is still larger than the reported ultralow thermal conductivity achieved in layered materials [17]. Yang *et al.* proposed to use two isotope doping methods to reduce the thermal conductivity of SiNWs. The first one is to dope SiNWs with isotope impurity randomly. The second one is to to build isotopic superlattice structured SiNWs. Their results show that the thermal conductivity of SiNWs can be reduced exponentially by isotopic defects at room temperature. The thermal conductivity reaches the minimum, which is about 27% of that of pure ^{28}Si NW, when doped with 50% isotope atoms. The thermal conductivity of isotopic-superlattice structured SiNWs depends clearly on the period of superlattice. At a critical period of 1.09nm , the thermal conductivity is only 25% the value of pure Si NW. An anomalous enhancement of thermal conductivity is observed when the superlattice period is smaller than this critical length [18].

The isotopic doping effect on the thermal conductivity of graphene nanoribbons is studied by classical molecular dynamics simulation with quantum correction [19]. It is found that in low isotopic doping region, the thermal conductivity decreases rapidly with increasing doping, and 10% doping can yield 50% reduction of the value of thermal conductivity; while in the high isotopic doping region, the thermal conductivity decreases slowly with further increasing doping. The underlying mechanism is that a single isotopic doping center can localize phonon modes which will reduce thermal transport. In addition to the isotope randomly doping, the thermal conductivity of isotopic superlattice graphene nanoribbons was also studied [20]. The thermal transport property of the isotopic superlattice graphene

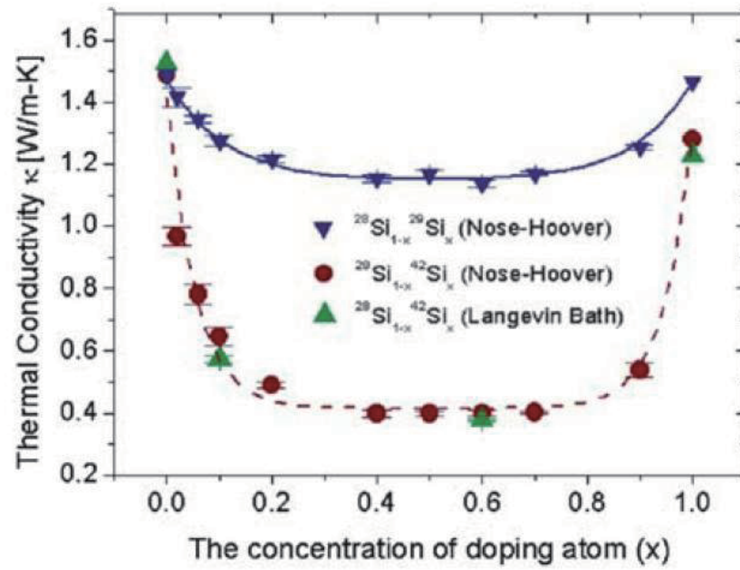

Figure 1.4: Thermal conductivity of SiNWs versus the percentage of randomly doping isotope atoms at $300K$. SiNWs are along the (100) direction with cross sections of (3×3) unit cells (lattice constant is $0.543nm$). The results, by the $Nosé - Hoover$, method coincide with those by Langevin methods indicating that the conclusions are independent of the heat bath used.(from Ref [18])

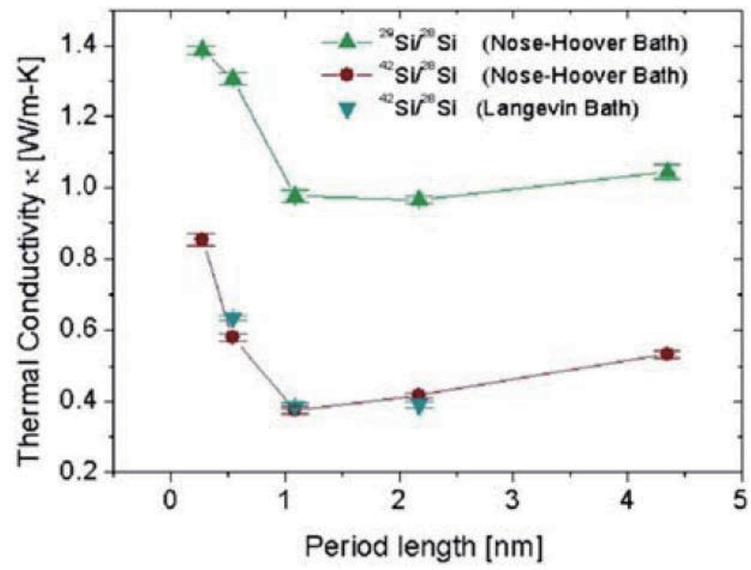

Figure 1.5: Thermal conductivity of the superlattice SiNWs versus the period length at $300K$. SiNWs are along the (100) direction with cross sections of (3×3) unit cells (lattice constant is $0.543nm$).(from Ref [18])

strongly depends on the superlattice period length and the isotopic mass. With the period length decreases, the thermal conductivity undergoes a transition from decreasing to increasing, which is explained by analyzing the phonon transmission coefficient, and a larger mass difference induces smaller thermal conductivity.

Besides the isotopic doped semiconductor nanostructures, the compound semiconductors also have low thermal conductivity. Silicon and germanium alloy ($Si_{1-x}Ge_x$) is of particular interest for its thermoelectric applications. Chen *et al.* have proposed to dope Ge atoms in the Si NWs to reduce the thermal conductivity of Si NWs. They found that the thermal conductivity reaches the minimum, which is about 18% of that of pure Si NW, when Ge content is 50%. More interesting, with only 5% Ge atoms $Si_{0.95}Ge_{0.05}$ NW, the thermal conductivity of Si NWs is reduced to 50%. The reduction of thermal conductivity mainly comes from the localization of phonon modes due to random scattering [21].

1.3.2 Improvement of Thermal Power Factor

Since the reduction in the lattice thermal conductivity has been realized in nanostructures, further increase in the thermoelectric figure of merit requires the improvement of the thermal power factor ($P = S^2\sigma$). In general, there are three main methods in this aspect. The first method is to increase the mobility of materials. The mobility in nanostructures can be influenced by the grain boundaries. If we can reduce the negative effect of the grain boundaries on the mobility in the fabrication process, it is possible to enhance ZT. The Kanatzidis group has recently found that nanostructure PbTe with encapsulated nanodots made of both

Pb and Sb has an increased mobility over that of the bulk PbTe, resulting in a ZT a factor of two larger than that of bulk PbTe [22]. The second method is to increase the Seebeck coefficient by the introduction of the phonon drag effect and energy filtering. On the one hand, for the phonon drag effect, with the electron and phonon collision, the momentum is transferred from the phonons to the electrons, which gives rise to the phonon-drag thermopower (Seebeck coefficient) [23], which has also been confirmed in experiment. Boukai *et al.* found that there is a peak of the Seebeck coefficient, S, in Si NWs from the phonon drag effect at around $T = 200K$, where they can achieve a value of ZT = 1.0. [15]. The Seebeck coefficient from the phonon-drag effect in Si NWs is shown in Figure 1.6. The blue triangle curve is the measured electronic Seebeck coefficient and the black dotted curve is the measured total Seebeck coefficient. The red curve is the theoretical calculation of phonon-drag thermopower. It is obvious from the figure that the phonon-drag thermopower is dominant. On the other hand, the energy filtering can be understood from Figure 1.7. In this figure, the calculated Seebeck coefficient distribution versus energy for heavily doped bulk n-type $Si_{80}Ge_{20}$ is shown. If the transport of those low energy electrons, which will reduce the total Seebeck coefficient, is minimized, the value of the Seebeck coefficient will be increased greatly [3]. Shakouri and coworkers have studied the energy filtering both theoretically and experimentally. They reported that a InGaAs/InGaAlAs superlattice has shown an increase in the power factor because of the energy filtering effects [24]. Moreover, it is reported that an increase in the Seebeck coefficient due to the energy filtering effects is also found in bulk nanstructured PbTe-based materials [25, 26].

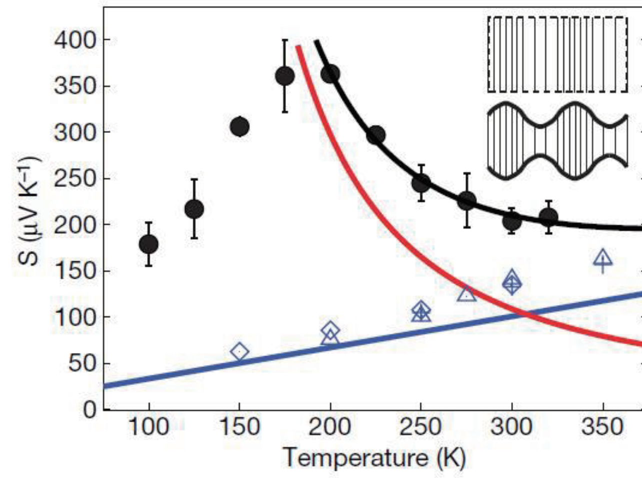

Figure 1.6: Thermopower calculation plotted along with experimental data (black points) from a 20-nm-wide Si nanowire p-type doped at $3 \times 10^{19} (cm^{-3})$.).(from Ref [15])

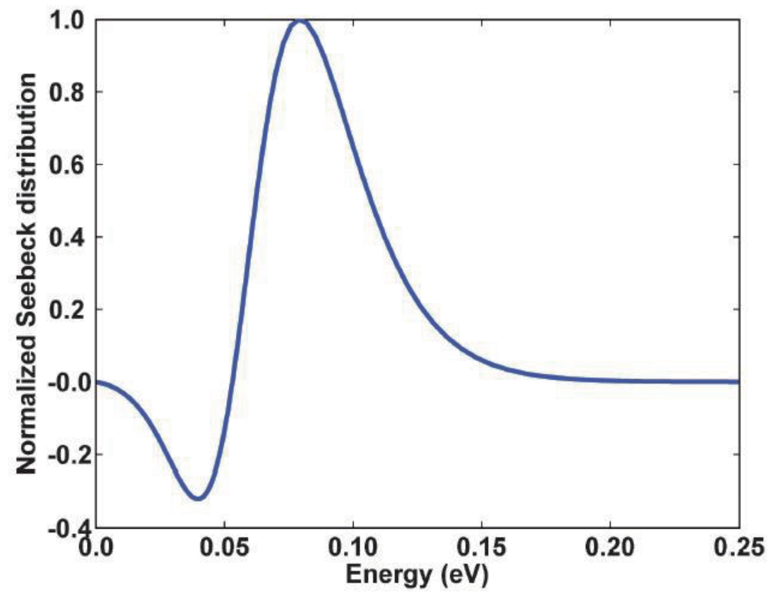

Figure 1.7: Calculated normalized Seebeck distribution versus energy for heavily doped bulk n-type $Si_{80}Ge_{20}$. Low energy electrons reduce the total Seebeck coefficient.).(from Ref [3])

The third method is to increase the Seebeck coefficient by using the impurity band energy levels. In most doped semiconductors, the impurity atoms will introduce the states with energies into the band gap. If the electrons (or holes) are close to the conduction band or valence band edges, they can be thermally activated into the conduction band and valence band to conduct, which will result in a peak in the density of states . Figure 1.8 shows the density of states with the introduction of the impurity levels. If the Fermi energy level is very close to this resonant level of density of states, an increase in the Seebeck coefficient is expected. Mahan and Dresselhaus [27, 28] have theoretically predicted that the thermoelectric properties could be enhanced by the increase in the density of states. Heremans and coworkers have recently demonstrated that with the use of the resonant level in bulk Tl-doped PbTe, a significant increase in the Seebeck coefficient over the bulk materials is achieved in experiment [29]. By the introduction of Tl atoms into bulk PbTe, there is a resonant level produced, which is close to the valence band edges of the bulk PbTe. Moreover, the Fermi level is also near the valence band edges in p-type PbTe, and thus the Seebeck coefficient is greatly enhanced. They are able to obtain a ZT = 1.5 by 2% Tl concentration doped in PbTe, which is twice larger than in bulk p-type PbTe. After that we have discussed the methods to improve the thermoelectric figure of merit in nanomaterials, we will turn in to report the achieved ZT in semiconductor nanowires, superlattices, and nanocomposites in the following sections.

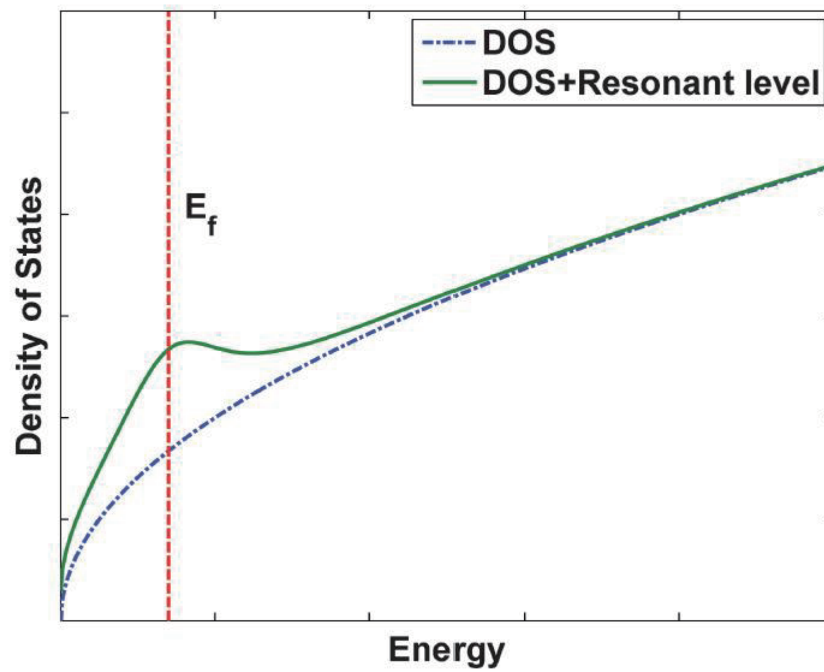

Figure 1.8: Schematic of the effect of a resonant level on the electronic density of states (DOS).).(from Ref [3])

1.4 Thermoelectric Figure of Merit ZT in Nanostructured Systems

1.4.1 ZT in Nanowires and Superlattices

Early in 1993, L.D. Hick *et al.* proposed that the theoretical models in $1D$ conductor (quantum wires) system [28] and in periodic $2D$ quantum-well system [4] could improve the values of ZT, which has also been demonstrated in experiment[30, 31]. They attributed this increase in ZT to the quantum confinement effects. Today semiconductor nanowires (NWs) and superlattices (SLs) have attracted much attention due to their fascinating thermoelectric applications. Large values of ZT can be found in NWs and SLs. The main reason is that significant reduction in the thermal conductivity due to the strong phonon scatterings from the boundary scatterings and interface scatterings is found in NWs and SLs, respectively (this has been discussed in the above sections. For example, Hochbaum *et al.* fabricated the Si nanowires (Si NWs) to achieve a value of ZT about 0.6 at room temperature, which is two orders magnitude larger than that in bulk Si [14], because that the thermal conductivity in Si NWs is much smaller than that in bulk Si due to the strong phonon scatterings from the rough surfaces of Si NWs. Venkatasubramanian *et al.* demonstrated that Bi_2Te_3/Sb_2Te_3 superlattices show a large enhancement in ZT up to 2.4 at room temperature when p-doped, and that ZT 1.4 [32]is obtained in n-type $Bi_2Te_3/Bi_2Te_{2.83}Sb_{0.17}$ superlattices (See Figure 1.9). Harman *et al.* used n-type PbSeTe/PbTe-based quantum dot superlattice structures to

achieve ZT 1.3 − 1.6 at room temperature [33].

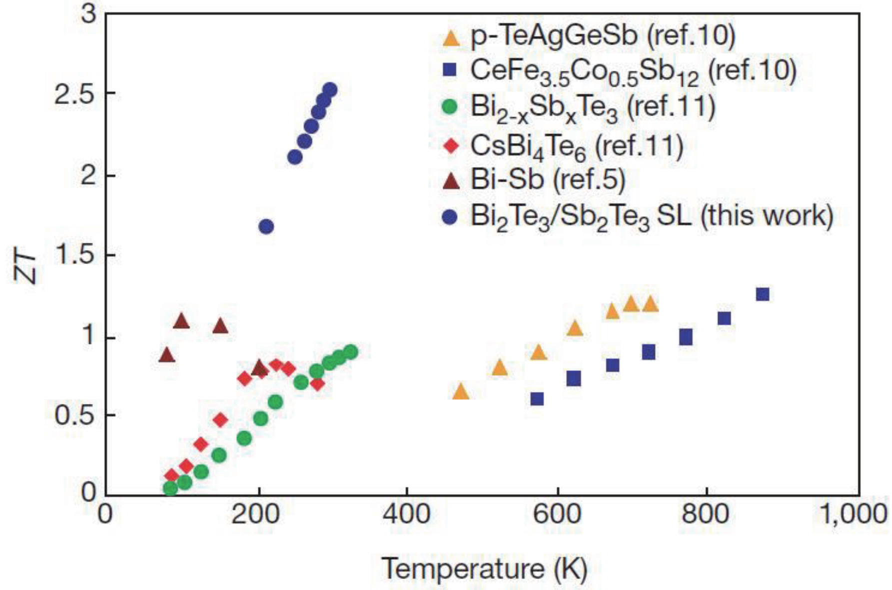

Figure 1.9: Temperature dependence of ZT of 10Å/50Å p-type Bi_2Te_3/Sb_2Te_3 superlattice compared to those of several recently reported materials.(from Ref [32])

Besides experimental work, there is much theoretical work focusing on the thermoelectric properties of NWs. Vo *et al.* investigated the effects of the growth direction and doping on the thermoelectric figure of merit ZT in thin Si NW by using ab initio electronic band structure calculations and Boltzmann Transport Equation. They aimed to obtain an optimal ZT by tuning the growth direction and doping in p-type and n-type Si NWs. Their results show that only by reducing the ionic thermal conductivity by about 2 or 3 orders of magnitudes with respect to bulk values, one may attain ZT larger than 1, for 1 or 3 nm wires, respectively. They also found that ZT of p-doped wires is considerably smaller than that of their n-doped counterparts with the same size and geometry [34].

1.4.2 ZT in Nanocomposites

Besides that the large ZT can be realized in both superlattices and nanowires, at the present time, a number of research groups are developing nanocomposite materials to increase ZT. The reasons are :(1) the reduction in the thermal conductivity is more than electrical conductivity by boundary scattering, and (2) the increase in S is more than the decrease in the electrical conductivity, and thus yielding an increase in the power factor. Nanocomposite thermoelectric materials have shown the improved performance compared with their corresponding bulk materials in experiment [35–38]. Silicon and Germanium nanocomposites (SiGe) have attracted much attention due to its large ZT. Wang *et al.* [39] reported that by using a nanostructure approach, a peak ZT of about 1.3 at $900^{o}C$ in an n-type nanostructured $Si_{80}Ge_{20}$ bulk alloy has been achieved.The enhancement of ZT comes mainly from a significant reduction in the thermal conductivity caused by the enhanced phonon scattering from the increased density of nanograin boundaries. The enhanced ZT makes such materials attractive in many applications such as solar, waste heat conversion into electricity. Joshi *et al* also reported that they could achieve the value of ZT (= 0.95) in p-type $Si_{80}Ge_{20}$ bulk alloy [40]. The enhancement of ZT is due to a large reduction of thermal conductivity caused by the increased phonon scattering at the grain boundaries of the nanostructures combined with an increased power factor at high temperatures. Zhu *et al* found that at 5% Ge replacing Si is very efficient in scattering phonons shorter than 1 nm, resulting in a further thermal conductivity reduction by a factor of 2 , thereby leading to a thermoelectric figure of merit 0.95 for $Si_{95}Ge_{05}$, similar to that of large grained $Si_{80}Ge_{20}$alloys [41]. The TEM image for the nanostructured $Si_{95}Ge_{5}$

sample is shown in Figure 1.10.

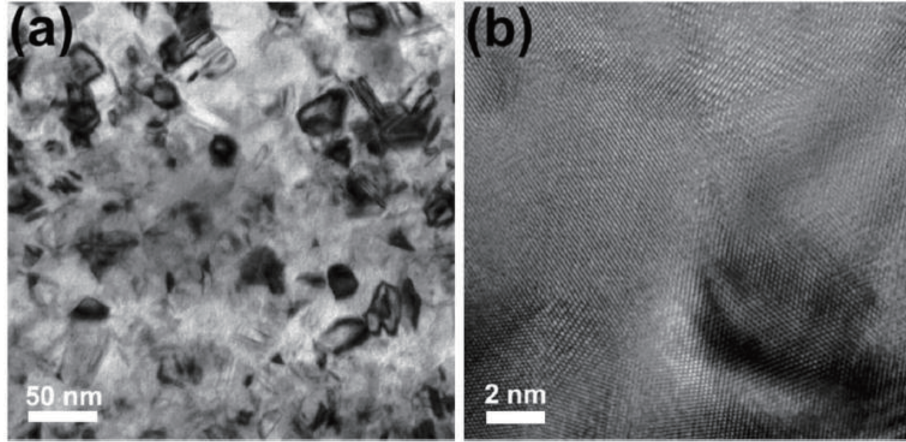

Figure 1.10: Low (a) and high (b) magnification TEM images of the hot pressed nanostructured $Si_{95}Ge_5$ sample.(from Ref [41])

Besides the experimental work, there are a lot of theoretical works concerning about the thermoelectric figure of merit in nanocomposites. These model calculations provide an important guide for the design and choice of processing parameters in the preparation of nanocomposite structures. For example, Minnich *et al* used the Boltzmann transport equation and the relaxation time approximation to study the thermoelectric properties of n-type and p-type SiGe nanocomposites. They considered the strong grain-boundary scattering mechanism in nanocomposites using phonon and electron grain-boundary scattering models. Their results from this analysis are in excellent agreement with recently reported measurements for the n-type nanocomposite. Their results also indicate that an improvement in mobility is possible by reducing the number of defects or reducing the number of trapping states at the grain boundaries [42]. Hao et al. investigate the thermoelectric properties of Si nanocmposites using Monte Carlo simulations and combine the phonon

modeling with electron modeling to predict the thermoelectric figure of merit (ZT) in silicon nanocomposites. The value of ZT they can be obtained is about 1.0 at $1173K$ when the grain size is reduced to $10nm$. Their results show the potential of achieving a large ZT in bulk Si by the nanocomposites [43]. In this thesis, we focus on the investigation of the thermoelectric property of semiconductor nanwires. In Chapter 2, we will turn into discussing the theoretical models and numerical methods, which have been used to study the the thermoelectric properties of nanowires.

1.5 Outline of Thesis

The dissertation is divided into 5 chapters.

Chapter 1 provides the background information, including the description of the Seebeck effect, Peltier effect and thermoelectric figure of merit (ZT). The literature review of the ZT in nanostructures is also presented.

Chapter 2 introduces the theoretical models and numerical methods. Both the Boltzmann transport equation and semiclassical ballistic transport equation are presented.

Chapter 3 to Chapter 4 represent the main study of the works relevant to my Ph. D. research project. The collaboration-ship of the presented works, if any, will be credited at the end of respective chapters.

Chapter 3 studies the size dependent the thermoelectric properties of silicon nanowires, examines the composition effects on the thermoelectric properties of silicon-germanium $Si_{1-x}Ge_x$ nanowires (NWs) and investigates the impact of the phase transition and Gallium (Ga) doping effect on the thermoelectric properties of [0001] ZnO nanowires.

Chapter 4 studies the significant enhancement of the thermoelectric figure of merit in [001] $Si_{0.5}Ge_{0.5}$ superlattice nanowires.

Chapter 5 summarizes the whole dissertation by correlating the individual chapters (Chapter 2 to Chapter 4), and draws a general conclusion of my Ph. D. research

project. Some remarkable points will be highlighted, and further works, either on agenda or still in mind, will be prospected in hope of meliorating and enriching the whole story.

Chapter 2

Theoretical Models and Numerical Methods

In this chapter, we will discuss theoretical models and numerical methods, which are used to study the thermoelectric properties of semiconductor nanowires. For the charge (electrons and holes) transport, in the diffusive regime (the system size is much larger than the mean free path), the convention theory is the Boltzmann Transport Equation (BTE), while for the ballistic regime (the system size is much less than the mean free path.), the semiclassical ballistic transport theory is widely used. In order to obtain the solutions of the BTE and semiclassical ballistic transport theory, the first principle method is applied to calculate the important input parameters, such as the electronic band structure and electronic density of

states. Either the first principle method or ab initio is based on the density functional theory(DFT). In the following sections, we will give a brief introduction of the basic concepts of the density functional theory. And for the phonon transport, two main numerical methods are used: Molecular Dynamics Simulation (MD)and Nonequilibrium Green's Function (NEGF). In this thesis, we will not discuss these two methods and we only focus on the discussion on the BTE, semiclassical ballistic transport theory and DFT.

2.1 Boltzmann Transport Equation

The semiclassical transport coefficient is based on the solutions of steady-state Boltzmann Transport Equation (BTE) via the relaxation time approximation. Hicks and Dresselhaus predicted the thermoelectric properties of $3D$ bulk materials $2D$ quantum wells [4] and $1D$ conductors [28] with the solutions of the Boltzmann transport equation (BTE). In Hicks' calculations, they used the BTE to obtain the thermoelectric transport coefficients under the single-band approximation, which are unable to give the accurate description of the systems, especially the atomic systems. Besides that, from the recent work [44] , the power factor described with the single-band approximation is invalid even in the large nanostructures. The multi-band approximation should be considered in order to obtain the accurate results. Considering these aspects, the first principle method and ab initio calculation have been widely used to obtain electronic properties of nanostructures. For instance, Vo *et al.* combined the ab initio electronic band structure and the $1D$

Boltzmann transport equation to investigate the thermoelectric properties of Si N-Ws with $1nm$ and $3nm$ diameter [34]. In their calculations, they used the density functional theory (DFT) to calculate the electronic band structure and density of states of the Si NWs. The combination of DFT and Boltzmann transport equation has been widely used to study the thermoelectric properties of atomic structures [34, 45]. In the following, we will start to discuss Boltzmann transport equation,

When there is perturbation imposed in the systems, for a steady state, there is a balance between the effects of the fields and the scattering processes. The Fermi-Dirac distribution $f(E)$ is a function of the wave vector $\vec{k}$ and the position vector $\vec{r}$ of the charge carriers. Under the relaxation time approximation, the change of $f(E)$ can be expressed as follows [5]:

$$\frac{f(E) - f_0(E)}{\tau_e} = -\dot{\vec{k}}\frac{\partial f(E)}{\partial \vec{k}} - \dot{\vec{r}}\frac{\partial f(E)}{\partial \vec{r}} \tag{2.1}$$

where f and f_0 are the perturbed and unperturbed distribution functions, respectively. The equation of $f - f_0$ should be solved in terms of the electric field and the temperature gradient. E is the electron energy. Here, we assume that all the fields and flows are in the direction of the x -axis. If $|f - f_0| \ll f_0$, we can replace f by f_0 on the right-hand side of Equation (2.1). Then the Fermi-Dirac distribution will be dependent on the displacement through both the electric field and temperature gradient, we can obtain that

$$\frac{f(E) - f_0(E)}{\tau_e} = v(k)\frac{\partial f_0(E)}{\partial E}(\frac{\partial \mu}{\partial x} + \frac{E - \mu}{T}\frac{\partial T}{\partial x}), \tag{2.2}$$

where $v(k) = \frac{1}{\hbar}\frac{\partial E}{\partial k}$ is the velocity of carriers in the x-direction. μ is the Fermi energy. τ_e is the relaxation time, which is a complex parameter, with the relation to the scattering processes, including the boundary scattering, impurity scattering, electron-phonon scattering and so on. $D(E)$ is the electronic density of states. It is a bit difficult to get a reliable relaxation time. In some previous works and our work, we obtain this relaxation time by fitting the electronic mobility from the experimental data for the electrical conductivity. The number of carriers per unit volume in the range of energy from E to $E + dE$ is $f(E)D(E)dE$, therefore, the electric current density j is:

$$j = -\int_0^\infty ev(k)f(E)D(E)dE = -\int_0^\infty e\tau_e v(k)v(k)\frac{\partial f_0(E)}{\partial E}(\frac{\partial \mu}{\partial x} + \frac{E-\mu}{T}\frac{\partial T}{\partial x})D(E)dE \tag{2.3}$$

And the electric field ξ is given by $\frac{\partial \mu}{\partial x}/e$ and it is assumed that $\frac{\partial T}{\partial x} = 0$, the electrical conductivity is written as follows:

$$\sigma = j/\xi = -\int_0^\infty e^2\tau_e v(k)v(k)\frac{\partial f_0(E)}{\partial E}D(E)dE \tag{2.4}$$

In order to define the Seebeck coefficient S, we should make Eq. 2.3. to be zero. S is equal to $\frac{\partial \mu}{\partial x}[e(\frac{\partial T}{\partial x})]^{-1}$, which is given by:

$$S = \frac{1}{eT}\frac{\int_0^\infty \tau_e v(k)v(k)\frac{\partial f_0(E)}{\partial E}(E-\mu)D(E)dE}{\int_0^\infty \tau_e v(k)v(k)\frac{\partial f_0(E)}{\partial E}D(E)dE} \tag{2.5}$$

The heat flow per unit cross-section area from carriers ,J, is given by

$$J = \int_0^\infty v(k)(E-\mu)f(E)D(E)dE \tag{2.6}$$

The electronic thermal conductivity is given by:

$$\begin{aligned}
\kappa_e &= -J/\frac{\partial T}{\partial x} \\
&= \frac{1}{e^2T}[\int_0^\infty e^2 v(k)v(k)\tau_e(-\frac{\partial f_0(E)}{\partial E})(E-\mu)^2 D(E)dE \\
&- \frac{(\int_0^\infty e^2\tau_e v(k)v(k)\frac{\partial f_0(E)}{\partial E}(E-\mu)D(E)dE)(\int_0^\infty e^2\tau_e v(k)v(k)\frac{\partial f_0(E)}{\partial E}(E-\mu)D(E)dE)}{\int_0^\infty e^2\tau_e v(k)v(k)(-\frac{\partial f_0(E)}{\partial E})D(E)dE}
\end{aligned} \tag{2.7}$$

The above equations are applied to all the dimension, including $3D$, $2D$ and $1D$ cases. In our calculations, we assume that

$$\frac{1}{2}m^* v(k)v(k) = E \tag{2.8}$$

here m^* is the effective mass. Then we can obtain the expressions of the thermoelectric transport coefficients in one dimensional nanowires [46–48]. The electrical conductivity σ, the electronic thermal conductivity κ_e and the Seebeck coefficient S can be written as :

$$\sigma = \Lambda^{(0)} \tag{2.9}$$

$$\kappa_e = \frac{1}{e^2T}[\Lambda^{(2)} - \Lambda^{(1)}(\Lambda^{(0)})^{-1}\Lambda^{(1)}] \tag{2.10}$$

$$S = \frac{1}{eT}(\Lambda^{(0)})^{-1}\Lambda^{(1)} \tag{2.11}$$

$$\Lambda^{(n)} = e^2\tau(2/m^*)\sum_{E_k}\Delta E\frac{\beta exp[\beta(E_k-\mu)]}{[1+exp[\beta(E_k-\mu)]]^2}D(E_k)E_k(E_k-\mu)^{(n)} \tag{2.12}$$

where e is the charge of carriers, T is the temperature, $\beta = \frac{1}{k_BT}$ (k_B is the Boltzmann constant). E_k is the electron energy, τ is the relaxation time, m^* is the effective mass of the charge carrier, μ is the electron chemical potential and $D(E_k)$ is the density of states and it can be obtained from the first principle method or ab initio calculation, which will be introduced in the following sections.

2.2 Semiclassical Ballistic Transport Equation

For the ballistic regime, the expressions of transport coefficients are very similar to Eq. (2.9) to Eq.(2.12), which are based on the solutions to the Boltzmann transport equation (BTE). The set of the semiclassical ballistic transport equations is widely used to investigate the thermoelectric property of Si NWs [49], graphene nanoribbons [50]. The transport coefficients can be expressed as the following:

The electronic conductance :

$$G_e = e^2L^{(0)}(\mu) \tag{2.13}$$

The electronic thermal conductance :

$$\kappa_e = \frac{1}{T}[L^{(2)}(\mu) - L^{(1)}(\mu)[L^{(0)}(\mu)]^{-1}L^{(1)}(\mu)] \tag{2.14}$$

The Seebeck coefficient:

$$S = \frac{1}{eT}(L^{(0)}(\mu))^{-1}L^{(1)}(\mu) \tag{2.15}$$

$$L_m(\mu) = \frac{2}{h}\int_{-\infty}^{\infty} dET_e(E)(E-\mu)^{(m)}(-\frac{\partial f(E)}{\partial E}) \tag{2.16}$$

Here e is the charge. μ is Fermi energy. h is the Planck constant. E is the electron energy. T is the absolute temperature. $f(E)$ is the Fermi-Dirac distribution. $T_e(E)$ is electron(or hole)transmission. It is able to be achieved by Transiesta package, which is based on DFT and NEGF. In the following section, we will introduce the density functional theory (DFT).

2.3 Density Functional Theory

Density Functional Theory (DFT) has been the dominant method for the quantum mechanical simulation of periodic systems. It is widely used in the calculation of electronic band structure, density of states, energy surfaces and so on. In this section, we will give the basic concepts of density functional theory (DFT). From the quantum mechanics, the wave function can determine the total energy of the

systems $E[\Psi(r_1, r_2, r_3.....r_N)]$. In 1964, Hohenburg and Kohn proved the two theorems [51], which are named as $Hohenberg - Kohn$ (H-K)theorems. The first theorem is stated as follows: the electron density determines the external potential (to within an additive constant), which is given by:

$$E[\Psi(r_1, r_2, r_3.....r_N)] \longrightarrow E[\rho(r)] \tag{2.17}$$

And the second theorem is stated as follows: If the electron density $\rho(r)$ is not for ground state, then $E_{G.S.}[\rho(r)] \geq E_{G.S.}[\rho_{G.S.}(r)]$. We will try different electron density $\rho(r)$ to achieve the minimum energy $E_{G.S.}(\rho(r))$ and we also confirm this electron density to be the ground-state electron density. The H-K theorems only prove the existence of $E_{G.S.}(\rho(r))$ and do not show the definite expressions and equations. From the energy functional, the total energy contains three terms: the kinetic energy, the interaction with the external potential and electron-electron interactions, we can write them as:

$$E[\rho(r)] = T[\rho(r)] + V_{ext}[\rho(r)] + V_{ee}[\rho(r)] \tag{2.18}$$

The interaction of external potential is expressed as:

$$V_{ext}[\rho(r)] = \int \widehat{V_{ext}} \rho(r) dr \tag{2.19}$$

The kinetic energy and the electron-electron interaction is still unknown. Kohn and

Sham proposed the following approach to approximate the kinetic and electron-electron functionals [52]. They introduced a fictitious system of N noninteracting electrons to be described by a single determinant wave function in N orbitals ϕ_i. In this system the kinetic energy and electron density are known exactly from the orbitals:

$$T[\rho(r)] = -\frac{1}{2}\sum_{i}^{N} < \phi_i|\nabla^2|\phi_i > \tag{2.20}$$

The ground state density is :

$$\rho(r) = \sum_{i}^{N} |\phi_i|^2 \tag{2.21}$$

The electron-electron interaction will include the classical Coulomb interaction (Hartree energy)and exchange-correlation functional. The Coulomb interaction is expressed as:

$$V_H[\rho] = \frac{1}{2}\int \frac{\rho(\overrightarrow{r_1})\rho(\overrightarrow{r_2})}{|\overrightarrow{r_1} - \overrightarrow{r_2}|} d\overrightarrow{r_1} d\overrightarrow{r_2} \tag{2.22}$$

The exchange-correlation functional is written as:

$$E_{xc}[\rho] = \int \rho(r)\varepsilon_{xc}(\rho(r))dr \tag{2.23}$$

where ε_{xc} is the local charge density. The exchange and correlation energy density of the uniform electron gas density ρ is in the local density approximation (LDA).

Within LDA, ε_{xc} is a function of the local value of density. Another mostly used accurate approximation is the generalised gradient approximation (GGA). Within GGA, the energy functional that depends on both the density and its gradient.

Chapter 3

Thermoelectric Figure of Merit in [110]Si NWs, [110]$Si_{1-x}Ge_x$ NWs and [0001] ZnO Nanowires

In this chapter, we use the first-principle method and Boltzmann transport equation to study the thermoelectric figure of merit in silicon nanowires(SiNWs), $Si_{1-x}Ge_x$ NWs and [0001] ZnO nanowires. Firstly, we investigate size dependent thermoelectric properties of silicon nanowires. It is found that with cross section area increasing, the electrical conductivity increases slowly, while the Seebeck coefficient reduces remarkably. This leads to a quick reduction of cooling power factor with diameter. Moreover, the figure of merit also decreases with transverse size.

Our results demonstrate that in thermoelectric application, NW with small diameter is preferred.We also predict that isotopic doping can increase the value of ZT significantly.With 50% ^{29}Si doping ($^{28}Si_{0.5}{}^{29}Si_{0.5}NW$), the ZT can be increased by 31%.

Secondly, we study large figure of merit in $Si_{1-x}Ge_x$ nanowires. We investigate composition effects on the thermoelectric properties of silicon-germanium $Si_{1-x}Ge_x$ nanowires (NWs). The power factor and figure of merit in n-type $Si_{1-x}Ge_x$ wires are much larger than those in their p-type counterparts with the same Ge content and doping concentration. Moreover, the maximal obtainable figure of merit can be increased by a factor of 4.3 in n-type $Si_{0.5}Ge_{0.5}$ NWs, compared with the corresponding values in pure silicon nanowires (SiNWs). Given the fact that the measured ZT of n-type SiNW is $0.6-1.0$, we expect ZT value of n-type $Si_{1-x}Ge_xNWs$ to be $2.5-4.0$.

Finally, we study the impacts of the phase transition and Gallium doping on the thermoelectric properties of [0001] ZnO nanowires.Phase transition has played an important role in electronic conduction [53, 54] and thermal conduction in ZnO NWs [55], but this effect on thermoelectric is still unclear. Our results show that the electronic band gap of ZnO NWs for Wurtzite (W) phase is larger than that of Hexagonal (H) phase. For a certain carrier concentration, the Seebeck coefficient S for W-phase is larger than that for H-phase, while electrical conductivity with H-Phase is much higher than that of W-Phase because of the higher electron mobility in H-Phase. There is an optimal carrier concentration to achieve the maximum value of power factor P for both W and H phases. The maximum value of P (P_{max}) for H phase ($P_{max} = 1638\mu W/m-K^2$) is larger than that of W phase

($P_{max} = 1213\mu W/m - K^2$) due to its high electrical conductivity. In Ref [55], it is referred that the thermal conductivity for H phase is about 20% larger than that for W phase. Combined the calculations of power factor and the thermal conductivity, the maximum achievable value of figure of merit ZT for H phase is larger than that for W phase (1.1 times).

Furthermore, we also study the impacts of the Gallium doping on the thermoelectric properties of [0001] ZnO nanowires. It is found that the thermoelectric performance of the Ga-doped ZnO ($Zn_{1-x}Ga_xO$) NWs is strongly dependent on the Ga contents. The maximum achieved room-temperature thermoelectric figure of merit in $Zn_{1-x}Ga_xO$ can be increased by a factor 2.5 at Ga content is 0.04, compared with the corresponding pure ZnO wires. Our work provides design rules for possible ZnO NW arrays based piezoelectric, optoelectronic and thermoelectric hybrid energy generator.

3.1 Introduction

Thermoelectric material plays an important role in solving the energy crisis. The cooling efficiency is given by the figure of merit,ZT (= $S^2\sigma/\kappa$ T), here S is the Seebeck coefficient,σ is the electrical conductivity, T is the absolute temperature, and $\kappa = \kappa_e + \kappa_p$ is the thermal conductivity, where $\kappa_e$and κ_p are the electron and phonon lattice vibration contribution to the thermal conductivity, respectively.

Nanostructured materials have been proposed to enhance thermoelectric figure of

merit ZT (Refs. [28, 32, 33, 56]) due to both enhancement in the power factor through increasing the density of states near the Fermi energy level and reduction in the thermal conductivity. Silicon nanowire (SiNW) has attracted broad interests in recent years due to its ideal interface compatibility with Si based electronic technology and the potential applications.[57, 58] It has been demonstrated that the thermal conductivity of SiNW can be 100 times smaller than that of bulk silicon [7, 9, 14]. Vo et al.[34] have studied the impacts of growth direction and doping on the thermoelectric figure of merit in SiNWs by using ab initio electronic structure calculations. In addition to the growth direction and carrier concentration, it has been demonstrated that the electronic structure of Si NW also depends on the transverse size remarkably. [34, 59–61]. Moreover, it is well established that isotope doping is an efficient way to reduce the thermal conductivity.[18, 62, 63] In this chapter, we will investigate the impacts of size and isotope concentration on thermoelectric property of SiNW.

Besides SiNW, it has also been demonstrated that $Si_{1-x}Ge_xNW$ is a promising candidate for high-performance thermoelectric application [21]. It has been observed experimentally that when the Ge content in $Si_{1-x}Ge_x$ nanocomposites increases from 5% to 20%, the thermal conductivity decreases obviously [41]. However, at the same time, the power factor also decreases, and induces uncertainty in the change in figure of merit ZT. Although a number of studies have been reported recently about the thermal and thermoelectric properties of $Si_{1-x}Ge_x$ nanocomposites and nanowire,[21, 40, 41, 64–68] it is still not clear on the quantitative impact of the composition on the thermoelectric performance. In this chapter, we will investigate the composition dependence of the thermoelectric properties of

$Si_{1-x}Ge_xNWs$.

Besides the convention thermoelectric materials, such as Si NWs and $Si_{1-x}Ge_x$ NWs, the exploration of other thermoelectric materials is also very important for the improvement of thermoelectric figure of merit in materials. Recently, Znic Oxide (ZnO) nanowires (NWs) have shown promise for nanodevice applications. The high surface-to-volume ratio of NWs is important for many applications, such as gas sensors. Through the coupling of piezoelectric and semiconducting properties of ZnO, nanoscale mechanical energy can be converted into electrical energy by using ZnO NW arrays [69]. Moreover, compared to traditionally TiO_2 films, ZnO NW arrays are considered promising anode material for photovoltaic device because of the highly controllable single-crystalline morphology which provides direct electron transport pathway [70–72].In addition to piezoelectric and optoelectronic applications, thermoelectric effect is also an important part of the solution to the energy crisis by converting waste heat into electricity. To our best knowledges, rare researches are concerning about the thermoelectric properties of ZnO NWs [73]. Phase transition has played an important role in electronic conduction [53, 54] and thermal conduction in ZnO NWs [55]. Zhang *et al* found that the direct to indirect band gap transition occurs in ultrathin [0001] ZnO nanowires under the uniaxial compression. Their results show that all ZnO nanowires exhibit direct band gap in wurtzite (W) structure and indirect band gap in hexagonal (H) structure. For the same wire, the band gap in hexagonal structure is smaller than that in W structure[54]. Kulkarni *et al* used Green-Kubo approach to study the impacts of phase transition on the thermal conductivity in ZnO nanowires[55]. Their results show that the thermal conductivity in hexagonal (H) structure is

20% high than that in wurtzite (W) structure. However, the impacts of the phase transition on the thermoelectric properties in ZnO nanowires is still unclear. In this chapter, we use the $1D$ transport theory and the first-principle method to investigate the impacts of the phase transition on the thermoelectric properties of [0001]ZnO nanowires.

Besides the impacts of phase transition on the thermoelectric property in ZnO nanowires, it is found that the study of the thermoelectric property of ZnO ceramics has been motivated by the reports of the improved electrical conductivity and reduced thermal conductivity by employing elements (Al, Ga, Mn) as dopants[74–76]. In the Al and Ga dually doped ZnO ceramics, ZT is about twice of that of pure ZnO, which can arrive 0.65 at $1247K$ [74]. A natural question comes promptly: Can we obtain a piezoelectric, optoelectronic and thermoelectric hybrid energy generator based on ZnO NWs? And how to improve the thermoelectric property of ZnO NWs? Although there are a few researches focusing on the electrical properties of ZnO NWs [77–80], rare researches are concerning about the thermoelectric properties of ZnO NWs [73]. In this chapter, we will answer these questions through investigations with the first-principle method and $1D$ Boltzmann transport Theory (BTE), to explore the impacts of Ga doping on the thermoelectric performance of $Zn_{1-x}Ga_xO$ NWs.

3.2 Computation Methods

In this chapter, we combine the first principle method and $1D$ Boltzmann transport equation (BTE)to investigate the thermoelectric properties of semiconductor nanowires. The electrical conductivity σ, electronic thermal conductivity κ_e and Seebeck coefficient S are obtained from the electronic structure with the solution of 1-Dimensional Boltzmann transport equation:

$$\sigma = \Lambda^{(0)} \tag{3.1}$$

$$\kappa_e = \frac{1}{e^2 T}[\Lambda^{(2)} - \Lambda^{(1)}(\Lambda^{(0)})^{-1}\Lambda^{(1)}] \tag{3.2}$$

$$S = \frac{1}{eT}(\Lambda^{(0)})^{-1}\Lambda^{(1)} \tag{3.3}$$

$$\Lambda^{(n)} = e^2\tau(2/m^*)\sum_k \Delta E \frac{\beta exp[\beta(E_k - \mu)]}{[1 + exp[\beta(E_k - \mu)]]^2} D(E_k)E_k(E_k - \mu)^{(n)} \tag{3.4}$$

where e is the charge of carriers, T is the temperature, E_k is the electron energy, τ is the relaxation time, m^* is the effective mass of the charge carrier, μ is the electron chemical potential and $D(E_k)$ is the density of states. The relaxation time τ, is a complex function of the electronic structure, temperature and carrier concentrations.

3.3 Size Dependent Thermoelectric Properties of Silicon Nanowires

In this section, we investigate the thermoelectric properties of silicon nanowires. We focus on SiNWs oriented along the [110] direction since small diameter SiNWs have been observed to grow experimentally mostly along this direction. We studied SiNWs with rectangular cross section shape, which can be fabricated experimentally [34, 61, 81]. For each NW, the atomic structure is initially constructed from diamond structured bulk silicon. Then, all the Si atoms that fall within a virtual cage are selected while silicon atoms falling outside this virtual cage are removed. The dimensions of the NWs were varied by changing the virtual cages. Here the transverse dimension of SiNW is characterized by A - the cross section area, which is ranging from $1nm^2$ to about $18nm^2$. The corresponding diameter D is from 1.7 to $6.1nm$. Here D is defined as the largest distance between the terminating hydrogen atoms in the cross section plane. The surface dangling bonds were terminated with hydrogen atoms placed at a standard bond length of $1.48\AA$ that eliminate artificial dangling bonds. This H-termination model without surface reconstruction is widely used to study the size effect on electronic structure of SiNWs [59]. A supercell approach is adopted where each wire is periodically repeated along the growth direction [110]. The size of the supercells in the transverse plane is so large as to avoid interaction between the SiNW and its images in neighboring cells ($> 15\AA$ from surface to surface). In this work, the density functional derived tight-binding method (DFTB) [82, 83] is used. The DFTB has high computational efficiency and

allows the simulation of bigger systems than conventional density functional theory (DFT) at a reasonable computational time and with similar accuracy. In this work, the structural relaxation is performed using a conjugate gradient method. The atomic force tolerance of $3\times10^{-4}eV$ is applied. Self-consistent charge tolerance is $10^{-5}au$. The accuracy of DFTB method in SiNW band structure calculation has been demonstrated [59, 84].

The goal of our work is to determine the qualitative effect of SiNW's transverse dimension on its thermoelectric property. So here we obtain the values of τ by fitting the calculated mobility to measured electrical conductivity data of SiNW. As the lack of experimental electrical conductivity data on diameter dependence, here we use the experimental data of SiNW with fixed diameter of $48nm$ ($n = 1.7\times 10^{19}cm^{-3}$, $\sigma = 588(\Omega cm)^{-1}$), from Ref. [14]), and obtain $\tau = 4.3\times10^{16}s$. Then, we use the dependence relation [85] between the mobility and carrier concentration in bulk silicon to calculate the carrier concentration dependent relaxation time. For example, $\tau = 1.7 \times 10^{15}s$ for $n = 1.0 \times 10^{17}cm^{-3}$, and $\tau = 9.7 \times 10^{16}s$ for $n = 5.0 \times 10^{17}cm^{-3}$. As ZT of n-doped SiNWs is considerably larger than that of their p-doped counterparts, we only study n-doped wires in this work. The carrier concentration is defined as $n = \int_0^\infty D(E-\mu)\times f(E-\mu)dE$, where $f(E)$ is the Fermi distribution function. In this model, n corresponds to the concentration of charge in a system that is artificially doped by varying the chemical potential while assuming a fixed band structure. With the change in μ, the carrier concentration changes, and induces the corresponding modification in thermoelectric property.

Figures 3.1(a) and 3.1(b) show the size effects on σ and S with different electron concentration. σ increases slightly as the diameter increases, while the Seebeck

coefficient S decreases remarkably. The size dependence arises from quantum confinement effect on the electronic band structure. Figure 3.2 shows the density of states (DOS) of intrinsic SiNWs. It is obvious that the larger the dimension of the wire the smaller the band gap. However, as the electron band gap converges quickly with transverse dimension increases [34, 59–61]. σ only has an obvious size dependence in very small size less than $5nm^2$. In contrast, Seebeck coefficient S decreases with increasing of size remarkably. Besides the electronic band gap, Seebeck coefficient S also depends on the detailed band structure, in which narrow DOS distribution is preferred [64, 86]. In SiNW, the large numbers of electronic states in narrow energy ranges can lead to large S. With the transverse dimension increases, the sharp DOS peaks widen and reduces S. The increase in transverse dimension has two effects on band structure: reduce the band gap; and widen the sharp DOS peaks, both have negative impacts on Seebeck coefficient. So the Seebeck coefficient decreases quickly with transverse size increasing. In addition to the transverse size dependence, both S and σ depend on carrier concentration. As shown in Figs. 3.1(c) and 3.1(d), S decreases as the carrier concentration increases, while σ increases as more carriers are available to transport charge.

In thermoelectric application, the power factor P ($P = S^2\sigma$), is an important factor influencing the thermoelectric performance directly. Figure 3.3(a) shows the power factor versus carrier concentration. There is an optimal carrier concentration N_{max} yielding the maximum attainable value of P_{max}. As SiNW area increases, the P_{max} decreases (Fig 3.3(b)), and N_{max} shifts to lower carrier concentration (Fig. 3.3(c)). The slow increase of σ is offset by obvious decreasing in S ($P = S^2\sigma$), as a result the power factor reduces with size increasing. In Fig.3.3(b), at small size, the

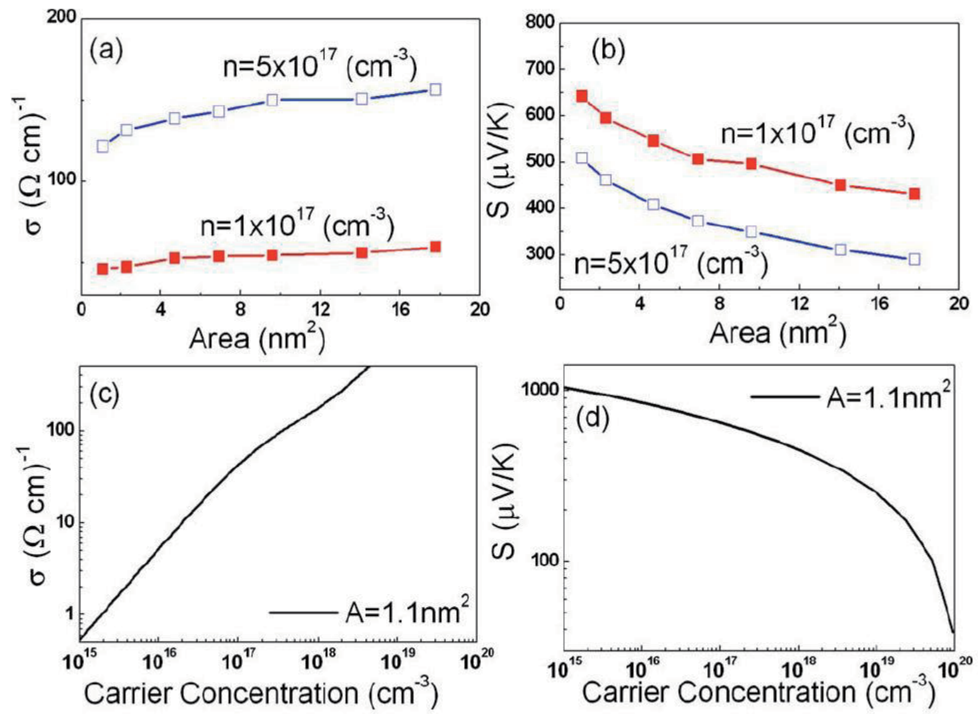

Figure 3.1: (a) σ vs cross sectional area with different carrier concentration. (b) S vs cross sectional area with different carrier concentration. (c)σ vs carrier concentration with fixed cross section area of $1.1nm^2$. (d) S vs carrier concentration with fixed area of $1.1nm^2$.

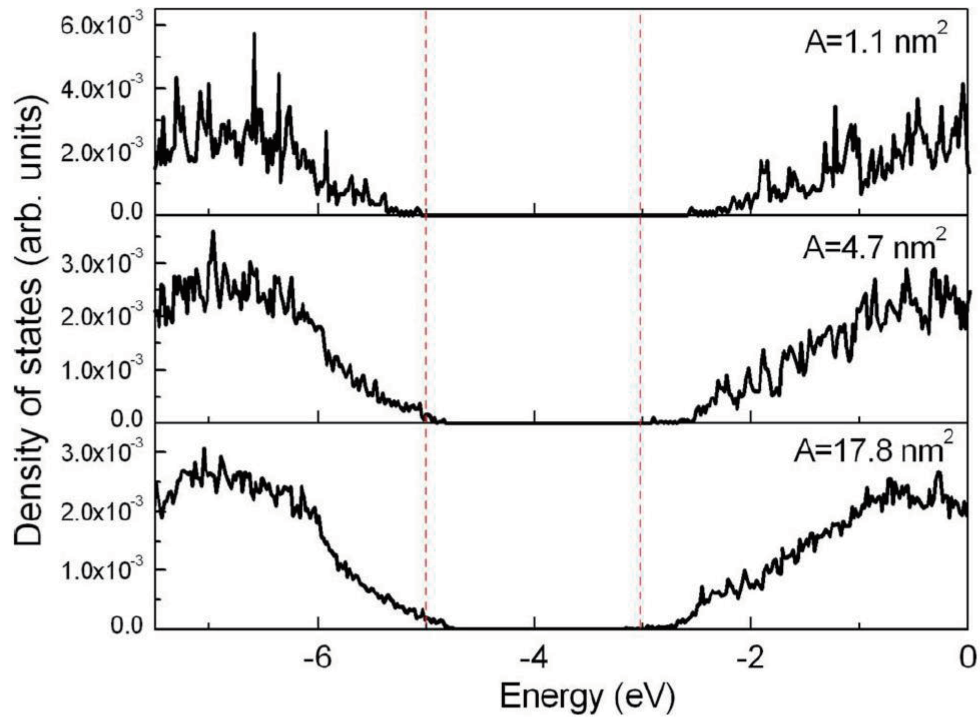

Figure 3.2: DOS for SiNWs with three different transverse dimensions from 1.1 to $17.8nm^2$. The red dotted lines are drawn to guide the eyes.

small increases of cross section area can induce large reduction on power factor. For example, with the cross section area increases from 1.1 to 4.7nm^2, the power factor decreases with about 4300$\mu W/mK^2$. In contrast, the power factor versus cross section area curves are almost flat when cross section area increases from 14.1 to 17.8nm^2.

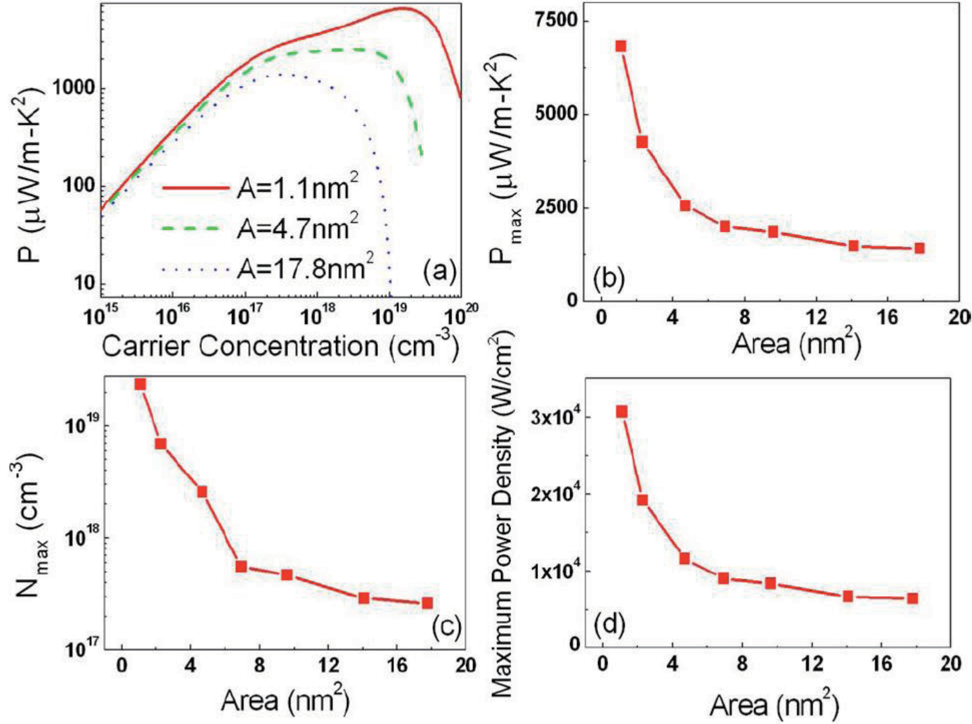

Figure 3.3: (a) Thermal power factor of SiNW vs carrier concentration with three different transverse dimensions. (b) Maximum power factor vs cross sectional area. (c) N_{max} vs cross sectional area. (d) Size dependence of the maximum room temperature cooling power density of SiNW with length of 1μm.

The power factor (P) is related to the cooling power density (PD) of a thermoelectric cooler. In the practical application, the maximal cooling power density is given by $PD_{max} = 1/2(S^2\sigma/L)T^2$, [87], T is the environment temperature around

the SiNW, and L is the length of the SiNW. In our analysis, we consider SiNW with length of $1\mu m$. Figure 3.3 (d) shows the size dependence of maximal cooling power density versus the cross section area at room temperature. Even for thick SiNW with cross section area of $17.8nm^2$, the maximal cooling power density, $6.4 \times 10^3 W/cm^2$, is about six times larger than that of SiGeC/Si superlattice coolers,[88] ten times larger than that of $Si/Si_{1-x}Ge_x$ cooler,[89] and six hundred times larger than that of commercial TE module.[90]

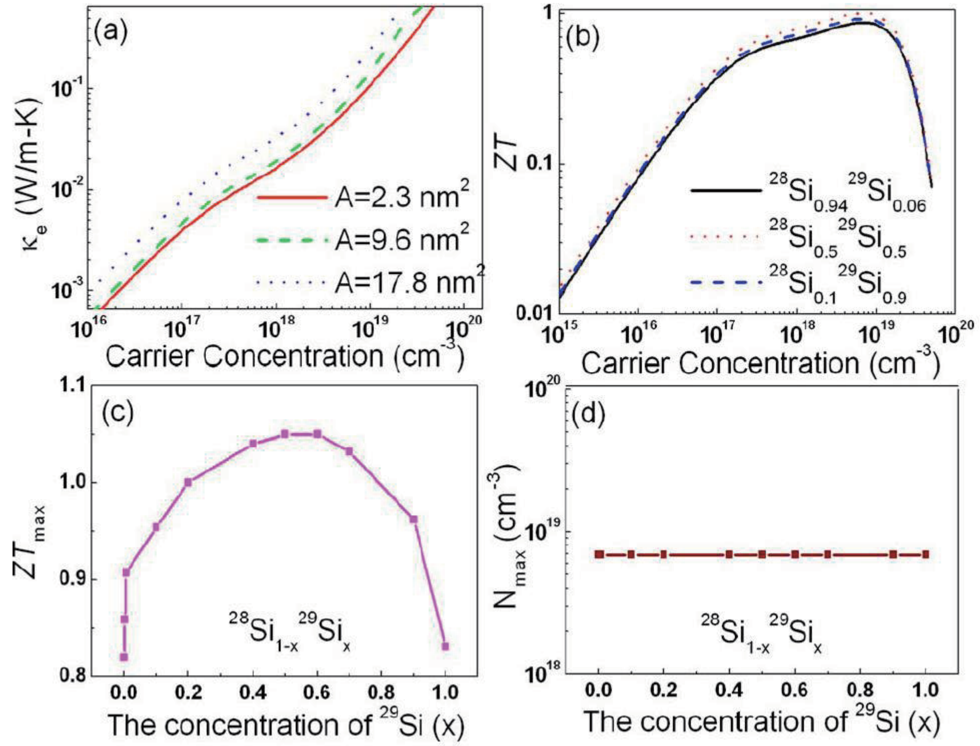

Figure 3.4: a) Thermal conductivity due to electrons vs carrier concentration for SiNWs with different transverse dimensions. (b) ZT vs carrier concentration for different isotope-doped SiNWs ($^{28}Si^{29}_{1-x}Si_x$ NWs) with fixed cross section area of $2.3nm^2$. (c) ZT_{max} vs the concentration of ^{29}Si atom. (d) N_{max} vs the concentration of ^{29}Si doping atom.

The figure of merit, ZT is another important factor for thermoelectric materials.

In the calculation of ZT, both electron and phonon contribute to the total thermal conductivity. Figure 3.4(a) shows the dependence of electron thermal conductivity calculated from Eq. 1 on carrier concentration. It is clear that κ_e increases with carrier concentration, and SiNW with larger diameter is with higher κ_e. And κ_p of SiNW increases with diameter increases remarkably until the diameter is larger than about hundreds nanometers.[91, 92] Thus κ increases with transverse dimension. Combine the size dependence of the power factor, as shown in Fig. 3.3 (b), we can conclude that ZT will decrease when the NW diameter increases. However, at present, there is no consensus in the literature about quantitative expression of size dependence of lattice (phonon) thermal conductivity in thin SiNWs, which limits the study of size effect on ZT quantitatively.

Besides diameter impact, the isotope doping is an important method to tune the thermal conductivity of nanomaterials. [18] In this work, we focus on the isotope doping effect on ZT of SiNW ($^{28}Si_{1-x}{}^{29}Si_x$ NWs) with fixed cross section area of $2.3nm^2$. From molecular dynamics calculation,[18] κ_p of pure ^{28}Si NW is $1.49W/mK$. In Fig. 3.4(a) it is obvious that with the carrier concentration we studied here, κ_p is much larger than κ_e. Using our calculated S, σ, κ_e from Eq. (1), and κ_p value from Ref. [18] calculated by using nonequilibrium molecular dynamics method, $Stillinger-Weber$ (SW) potential and $Nosé-Hoover$ /Langevin heat bath, more details in Ref. [18], the dependence of ZT on carrier concentration is shown in Fig.3.4 (b). Similar to the power factor, there exists one optimal carrier concentration N_{max} yielding the maximum attainable value of ZT_{max}. Moreover, the isotope doping concentration changes the value of ZT_{max} remarkably. Figures 3.4(c) and 3.4(d) show the dependence of ZT_{max} and N_{max} on concentration of Si.

The ZT_{max} values increase with ^{29}Si concentration, reach a maximum and then decreases. In the case of $^{28}Si_{0.8}{}^{29}Si_{0.2}NW$, namely, 20% ^{29}Si, its ZT_{max} increase with 15% from that of pure $^{28}SiNW$. And with 50%^{29}Si doping ($^{28}Si_{0.5}{}^{29}Si_{0.5}NW$), the ZT_{max} can increase with 31% . The carrier concentration N_{max} to attain ZT_{max} is independent on the isotope concentration, as the ^{29}Si doping only changes the lattice vibration and has no effect on the electronic structures in our calculations.

In summary, we have investigated the size dependence of thermoelectric properties of [110] oriented SiNWs. It is found that with cross section area increasing, the electrical conductivity increases as the reduction in band gap. In contrast to the weak size dependence of electrical conductivity, the Seebeck coefficient reduces remarkably with transverse dimension. This leads to a quick reduction of cooling power factor with diameter. At small size, the small increases of cross sectional area can induce large reduction in power factor. For example, with the cross section area increases from 1.1 to $4.7nm^2$, the power factor decreases with about $5000\mu W/m-K^2$. In contrast to the high sensitivity at the small size range, the power factor is almost constant when cross-sectional area increases from 14.1 to $17.8nm^2$. Even for thick SiNW ($A > 12nm^2$) with typical length of $2\mu m$, its cooling power density is hundreds times of that of conventional thermoelectric materials. Moreover, the figure of merit, ZT also decreases with increasing of transverse size. Our results demonstrated that in SiNW thermoelectric application, NW with small diameter is preferred. In addition to the size effect, we also present the prediction that the isotopic doping can increase the ZT value. With 50%^{29}Si doping ($^{28}Si_{0.5}{}^{29}Si_{0.5}NW$, with $A = 2.3nm^2$), the ZT can be increased 31%, from 0.81 to 1.06. Our results demonstrate that isotope doping is a promising method

to enhance ZT of SiNWs further.

3.4 Large Thermoelectric Figure of Merit in $Si_{1-x}Ge_x$ Nanowires

We focus on $Si_{1-x}Ge_x$ NWs oriented along the [110] direction with rectangular cross section area of $2.3nm^2$. The Si atoms are randomly substituted by Ge atoms. The surface dangling bonds are terminated with hydrogen atoms. The size of the supercells in the transverse plane is large enough ($> 15\AA$)from surface to surface). Here the density functional theory (DFT)) calculations are carried out by DMOL package.[93] The DFT calculations are performed by using generalized gradient approximation with the functional parameterized by Perdew, Burke, and Ernzerhof.[94] And the double-numerical-polarization basis set is employed. Self consistent field calculations are done with a convergence criterion of 10^{-6} hartree on the total energy. The Brillouin zone integration is performed using a $6 \times 6 \times 6$ Monkhorst-Pack k-point grid. All the structures are fully optimized with a convergence criterion of $0.002hartree/\AA$ for the forces and $0.005\AA$ for the displacement. A real-space cutoff of $4.0\AA$ for the atom-centered basis set is chosen to increase computational efficiency while not significantly affecting the magnitude of interatomic forces or the total energies. The Gaussian smearing of electron density is applied with the energy range of $0.1eV$.

The electrical conductivity σ, the thermal conductivity due to electrons κ_e, and the

Seebeck coefficient S, are obtained from the electronic structure with the solution of one-dimensional Boltzmann transport equation as described in Ref. [[46]]. Here we use the experimental data of n-type $Si_{0.95}Ge_{0.05}$ alloy ($n = 1.5 \times 10^{20} cm^{-3}$, $\sigma = 3400 Scm^{-1}$ from Ref. [[41]], and the dependence relation [67] between the mobility and carrier concentration in $Si_{1-x}Ge_x$ alloys to calculate the carrier concentration dependent relaxation time. The carrier concentration is defined as:$n = \int_0^\infty D(E) f(E) dE$, where $f(E)$ is the Fermi distribution function.

Figure 3.5 shows the Ge content (x) dependence of the electronic band gap. Bulk Si and Ge are indirect band gap semiconductors with the valence-band-maximum located at the Γ point. In bulk silicon, its conduction-band-minimum (CBM) located on Δ line (from Γ point to X point), while in bulk Ge, its CBM is on the λ line (from Γ point to L point). Therefore in bulk $Si_{1-x}Ge_x$ alloy, with x increases from 0 to 1, there is a transition in the location of CBM. However, for pure Si(Ge) nanowire, it has direct band gap due to the quantum confinement effect [59]. Thus in the $Si_{1-x}Ge_x$ NWs, there is no transition in the location of CBM. In order to reduce the fluctuation, the results are averaged over five realizations. With the Ge content increases, the averaged band gap decreases. This is consistent with the experimental observed energy band gap in single crystalline $Si_{1-x}Ge_x$ NWs [95]. However, in Ref. [95], the band gap of pure Ge NW is about $0.4eV$ less than that in pure Si NW, while the calculated value is $0.2eV$ here. This is because the commonly used DFT methods underestimate the value of band gap by about 50% [96]. In the calculations of thermoelectric properties, the DOS of specific NW structure is used which has the corresponding band gap mostly close to the average band gap value.

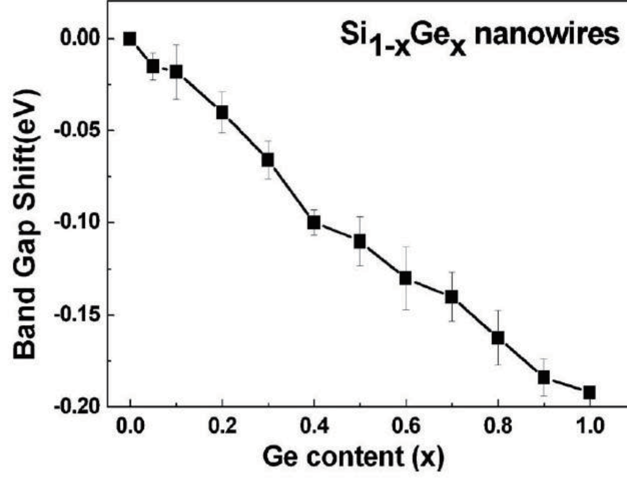

Figure 3.5: **The electronic band gap shift for $Si_{1-x}Ge_x$ NWs vs Ge contents x from** 0 **to** 1**.**

Figure 3.6 shows the Ge content dependence of σ and S with different electron concentration for $Si_{1-x}Ge_x$ NWs. Here we choose the heavily doped case because the maximum ZT is expected to occur for high carrier concentration, which has been confirmed experimentally,[40, 41, 64] and also to reduce the unknown effects of the band-gap uncertainty on the calculated values of S.[97, 98] In n-type wires ($n = 1.0 \times 10^{20} cm^{-3}$), σ decreases with x, reaches a minimum, and then increases. However, in p-type wires, σ increases almost monotonically as the Ge content increases. The different trends of σ can be explained from their charge mobility. In general considerations, there are three dominant scattering mechanisms in $Si_{1-x}Ge_x$ composites as follows [67]:alloy, acoustic phonon, and impurity scatterings. The total mobility is $\mu^{-1} = \mu_V^{-1} + \mu_{alloy}^{-1}$, where μ_V is related to the combination of acoustic phonon and impurity scatterings, and μ_{alloy} is the contribution from alloy scattering, respectively [67]. As shown in Table I, μ_{alloy} decreases

as x increases remarkably, reaches a minimum at $x = 0.5$ and then increases. While μ_{PV} and μ_{NV} increases with x monotonically, with μ_{NV} is about twice of μ_{PV}. So in p-type wires, μ_{PV} is the dominant contribution to μ_{total}, and μ_{total} increases with x monotonically. However, in n-type wires the alloy scattering dominates the system, thus μ_{total} decreases with x first, and then increases when $x = 0.4$. Figure 3.6(b) shows that the Seebeck coefficient S decreases as the Ge content increases.

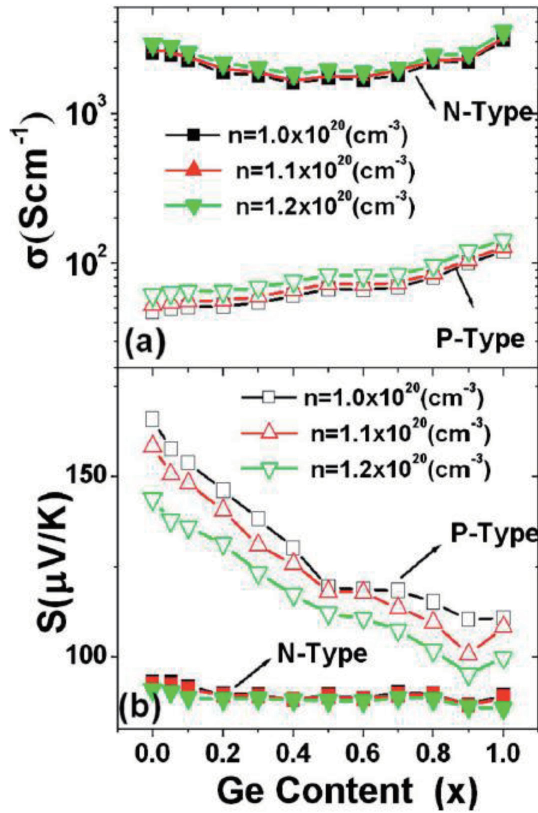

Figure 3.6: (a) σ vs Ge content x with different carrier concentration for n-type and p-type wires; (b)S vs Ge content with different carrier concentration for n-type and p-type wires.

Figure 3.7 shows the power factor P ($P = S^2\sigma$) versus carrier concentration. There is an optimal carrier concentration N_{max} yielding the maximum attainable value

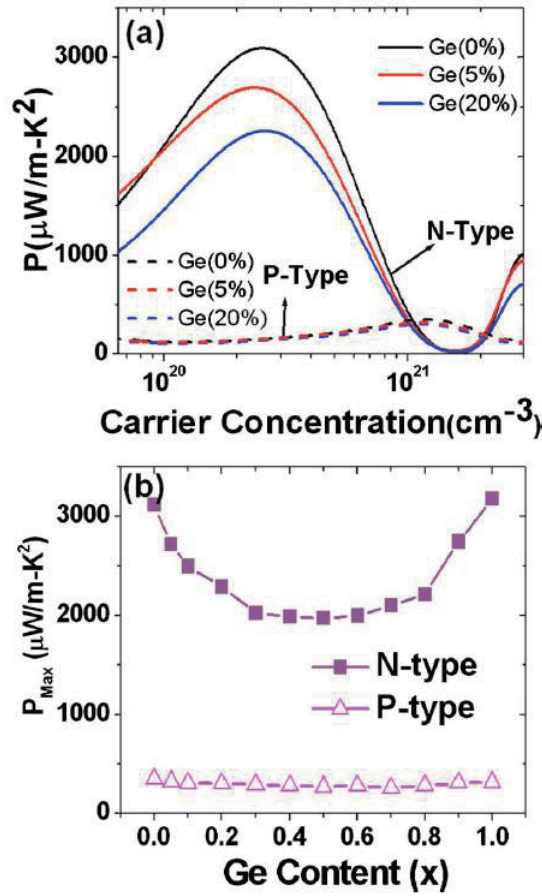

Figure 3.7: Thermal power factors of $Si_{1-x}Ge_x$ NWs vs carrier concentration with three different Ge contents for n-type and p-type wires (a). Maximum power factors vs Ge content for n-type and p-type wires (b).

of P_{max}. Here, N_{max} is around $n = 2.0 \times 10^{20} cm^{-3}$ for n-type wires and $n = 1.0 \times 10^{21} cm^{-3}$ for p-type wires. As the Ge content increases, for n-type wires, P_{max} decreases remarkably until $x = 0.5$, and then increases with x as shown in Fig. 3(b). For p-type wires, P_{max} decreases (Fig. 3(b)) as the Ge content increases monotonically until $x = 0.8$. The large fluctuation is partially due to the effects of the band-gap uncertainty on the calculated values.[97, 98] However, the power factor of p-type wire is much smaller (only about 15%) than that in its n-type counterpart because of the reduced charge mobility in p-type wires as shown in Table 3.1.

Table 3.1: The charge mobility in $Si_{1-x}Ge_x$ alloys ($n = 1.2 \times 10^{20} cm^{-3}$) for different Ge content x. The mobility values are calculated from Ref.[67]

x	$\mu_{alloy}(cm^2/VS)$	$\mu_{PV}(cm^2/VS)$	$\mu_{NV}(cm^2/VS)$	$\mu_{PTOT}(cm^2/VS)$	$\mu_{NTOT}(cm^2/VS)$
0.0	4000.4	40.24	87.94	39.84	86.05
0.05	834.13	41.91	89.64	39.90	80.93
0.2	248.13	48.33	96.85	40.50	69.81
0.4	166.12	56.70	105.52	42.31	64.61
0.5	160.02	60.05	110.02	43.76	65.41
0.6	167.54	64.82	114.89	46.76	68.19
0.8	257.92	76.23	123.52	58.83	83.50
0.9	484.00	80.73	128.06	69.03	100.92
1.0	4000.41	80.92	132.48	79.31	128.23

ZT is the most important factor for thermoelectric materials. In the calculation of ZT, both electron and phonon contributions to the total thermal conductivity are counted. The phonon thermal conductivity has been investigated with molecular dynamics simulations, it is quite remarkable that with only 5% Ge atoms ($Si_{0.95}Ge_{0.05}$) NW, its thermal conductivity can be reduced 50% [21] The similar thermal conductivity reduction (by a factor of 2) is also observed experimentally in nanostructured silicon with a 5% replacement of Si by Ge.[41] And it is found that[46] phonon thermal conductivity dominates the thermal transport property. As different doping (p-type or n-type) only have various changes in the electronic property but the same impact on the lattice vibration, so the phonon thermal conductivity of p-type nanowire should be close to that of n-type wire. For instance, the room temperature thermal conductivity of p-type nanostructured $Si_{80}Ge_{20}$ is from 2.3 to 2.6W/mK [40], while the room temperature thermal conductivity of n-type nanostructured $Si_{80}Ge_{20}$ is from 2.2 to2.5W/mK [64]. As shown in Fig. 3.7, the ZT of n-type wire is about six to seven times of that of p-type nanowire. In the next section, we only show the Ge content dependent ZT of n-type NW.

Using our calculated power factor, and the relative phonon thermal conductivity κ_{SiGe} /κ_{Si}, here κ_{Si} and κ_{SiGe} are thermal conductivities of SiNW and $Si_{1-x}Ge_x$ NW, respectively from Ref. [21], the dependence of $ZT_{Si_{1-x}Ge_x}$ /ZT_{Si} on Ge content x is shown in Fig. 3.8 The $ZT_{Si_{1-x}Ge_x}$ /ZT_{Si} values increase with Ge content, reach a maximum and then decreases. In the case of $Si_{0.8}Ge_{0.2}$ NW, namely, 20% Ge, $ZT_{Si_{1-x}Ge_x}$ /ZT_{Si} is about 3.0. And with 50% Ge atoms ($Si_{0.5}Ge_{0.5}$ NW), the $ZT_{Si_{1-x}Ge_x}$ /ZT_{Si} can be as high as 4.3. The similar dependence of ZT is also observed in p-type wire. This phenomenon can be understood as the following.

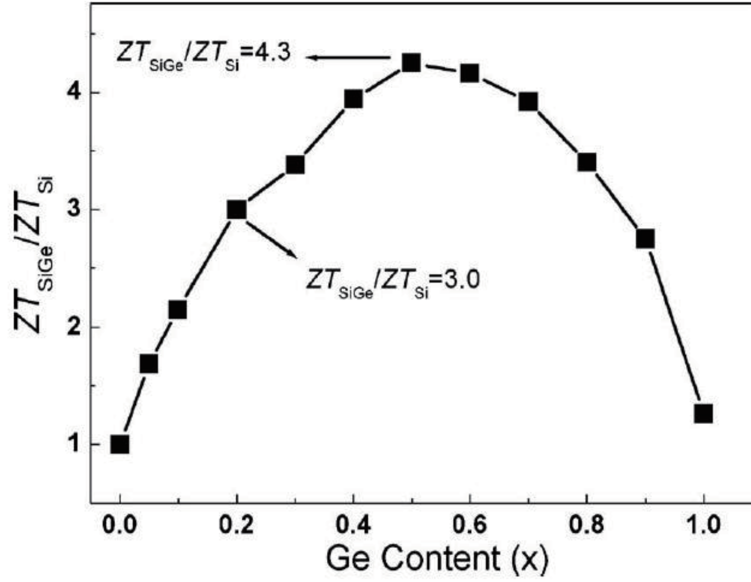

Figure 3.8: $ZT_{Si_{1-x}Ge_x}$ $/ZT_{Si}$ vs the Ge content x for n-type $Si_{1-x}Ge_x$ wires.

ZT is contributed by both power factor and thermal conductivity. As we discussed (refer to Fig. 3.7), in n-type $Si_{1-x}Ge_x$ NWs, the maximum obtainable power factor (P_{max}) decreases remarkably with Ge content to $x = 0.5$, and then increases slowly. The curve of thermal conductivity (refers to Ref. [21]) also decreases first to reach a minimum and then increases. However, when $0 \leq x \leq 0.5$, the reduction in thermal conductivity is much larger than the reduction in power factor, thus results in the increasing of ZT with Ge content. Our calculation results indicate that in comparison with the SiNWs, the ZT could be increased by a factor of 4.3 in n-type $Si_{1-x}Ge_x$ NWs. Given the fact that the experimental measured ZT of n-type SiNW is about 0.6 1.0, we may obtain ZT of about 2.5 4.0 in n-type $Si_{1-x}Ge_x$ NW.

In summary, a remarkable composition impact on the thermoelectric properties

of $Si_{1-x}Ge_x$ NWs is observed. We also found that the ZT in n-type wires is about six to seven times larger than that in p-type wires. Moreover, by tuning the Ge contents, ZT can be increased by a factor of 4.3 in n-type $Si_{0.5}Ge_{0.5}$ NWs. Our results demonstrate that n-type $Si_{1-x}Ge_x$ NWs are promising thermoelectric materials to achieve $ZT > 3$. Although the ZT of p-type $Si_{1-x}Ge_x$ NWs is higher than that of the p-type pure Si NWs, it is much lower than that of its n-type counterpart. In practical application, good thermoelectric performance for both n-type and p-type legs of a thermoelectric device are required. Improved ZT of p-type $Si_{1-x}Ge_x$ NWs deserves further investigation.

3.5 Impacts of Phase Transition on Thermoelectric Figure of Merit in [0001] ZnO Nanowires

We focus on on ultrathin ZnO nanowires oriented along the [0001] direction. The atomic structures are initially constructed from bulk wurzite (W)structure of ZnO solid. The geometry is relaxed to its closest minimum total energy. A supercell approach is adopted where each wire is periodically repeated along the growth direction. The size of the supercells in the transverse plane is large enough ($> 15\AA$ from surface to surface). Two repeated unit cells are required in the growth direction. The relaxed supercell length along the wire axis is about $10.4\AA$ for W structure and $8.2\AA$ for H structures, respectively, which is the same as Ref [53].The diameter of W-structured nanowire we considered is from $0.7nm$ to $1.4nm$ and that of

H-structured nanowires is from $0.7nm$ to $1.8nm$. . In this work, the density functional theory (DFT) calculations are carried out by $DMol3$ package [93].The DFT calculations are performed by using generalized gradient approximation with the functional parameterized by Perdew, Burke, and Ernzerhof [94]. And the double-numerical-polarization basis set is employed. Self-consistent field calculations are done with a convergence criterion of 10^{-6} hartree on the total energy. The Brillouin zone integration is performed using a $1 \times 1 \times 16$ Monkhorst-Pack k-point grid. All the structures are fully optimized with a convergence criterion of $0.002 hartree/\mathring{A}$. for the forces and $0.005\mathring{A}$ for the displacement. A real-space cutoff of $4.0\mathring{A}$ for the atom-centered basis set is chosen to increase computational efficiency while not significantly affecting the magnitude of inter-atomic forces or the total energies. The Gaussian smearing of electron density is applied with the energy range of $0.1eV$.

The electrical conductivity σ , the thermal conductivity due to electrons κ_e, and the Seebeck coefficient S, are obtained from the electronic structure with the solution of one-dimensional Boltzmann transport equation as described in Ref. [46, 47]. Here we use the experimental data of film [low carrier concentration, $20 - 30(\Omega cm)^{-1}$ from Ref. [100]] and the dependence relation [101] between the mobility and carrier concentration to calculate the carrier concentration dependent relaxation time. The carrier concentration is defined as:$n = \int_0^\infty f(E)D(E)dE$, where $f(E)$ is the Fermi distribution function.

Figure 3.9 shows the geometry for the optimized ZnO nanowires with different diameters for both W phase and H phase. From wire A to wire D, the diameter increases.

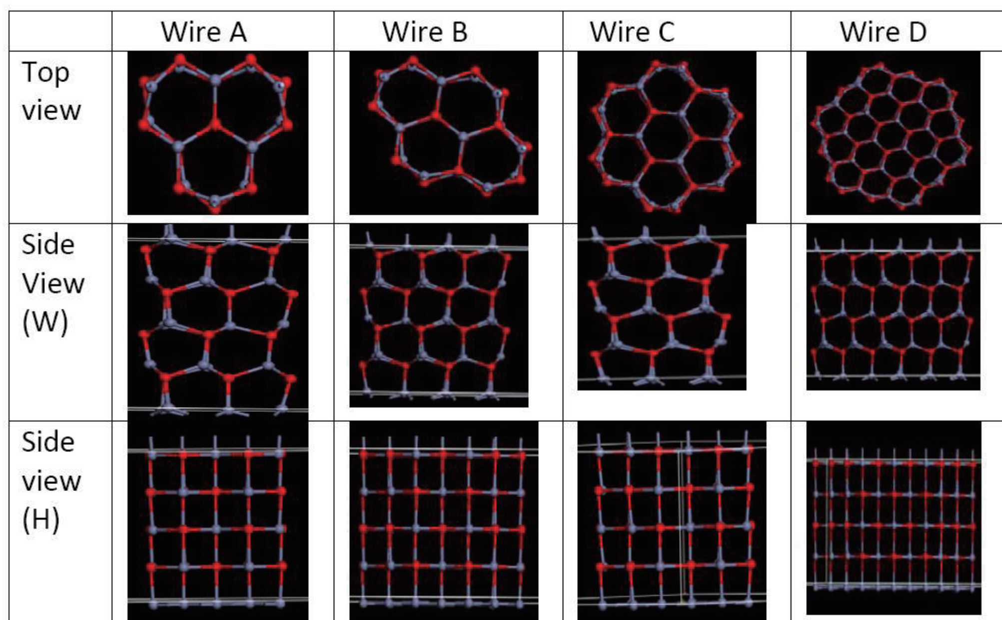

Figure 3.9: The geometry for the optimized ZnO nanowires with four different diameters for both W structure and H structure (top view and side view);Red: O atom; Gray: Zn atom.

Figure 3.10 shows the electronic band gap for wire A-D for both W phase and H phase. The electronic band gap deceases with the diameter increases (from wire A-D) For the same wire, the electronic band gap for W phase is larger than that of H phase, which has also been confirmed in Ref [53].

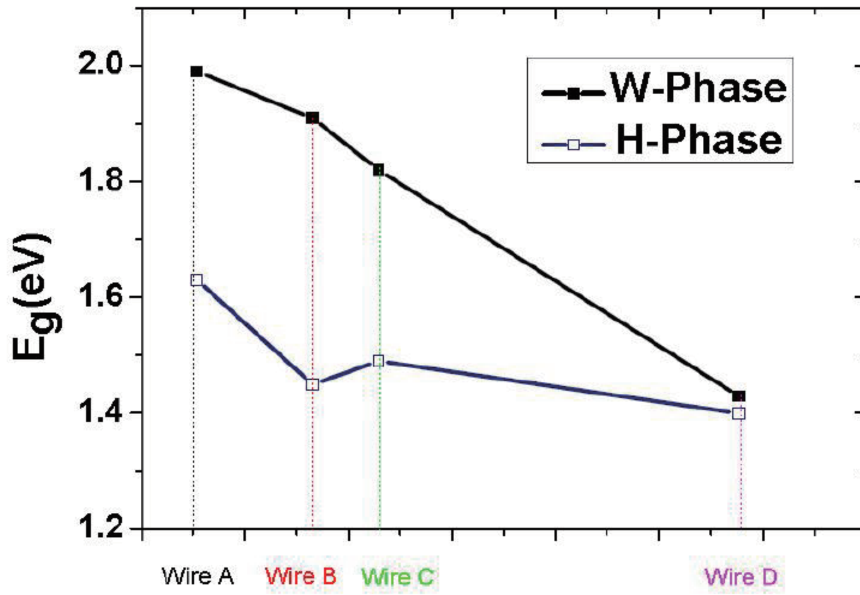

Figure 3.10: The electronic band gap for wire A, B, C,D for both W phase and H phase.

Figure 3.11(a) shows the electrical conductivity ,σ vs carrier cincentration for both the W phase and H phase. σ increases with the carrier concentration increases for both of the two phases. For a certain carrier concentration(n_e), σ for H phase is larger than that for W phase. It is attributed from the smaller effective mass for H-phase with the large dispersion of the lowest conduction band in the electronic band structure (See Figure 3.12). Figure 3.11(b) shows the Seebeck coefficient (S) vs carrier concentration. S decreases with the carrier concentration increases for the two phases. For a certain carrier conectration, S for W phase is larger than

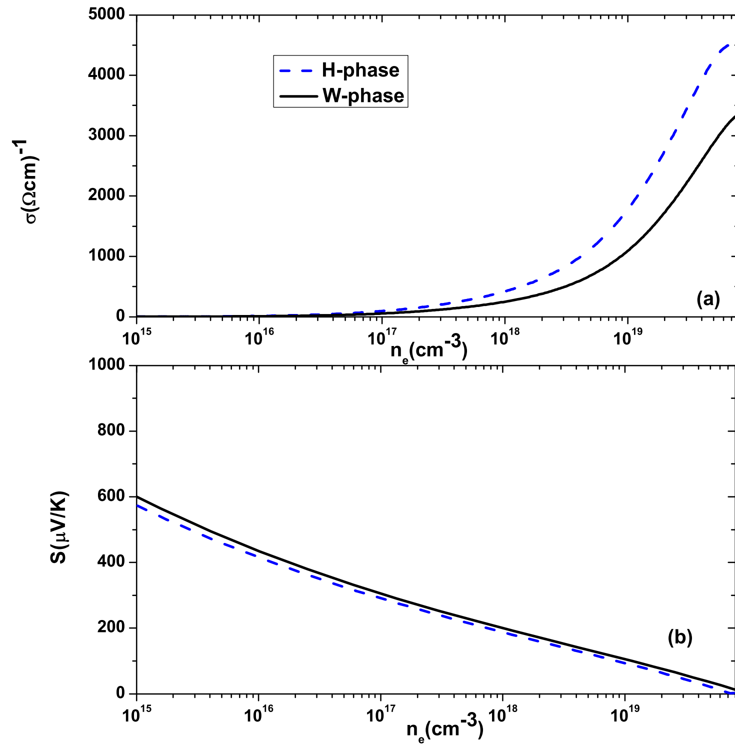

Figure 3.11: σ vs n_e (a); S vs n_e for both W phase and H phase.

that for H phase. It is because that the larger electronic band gap, the larger S.

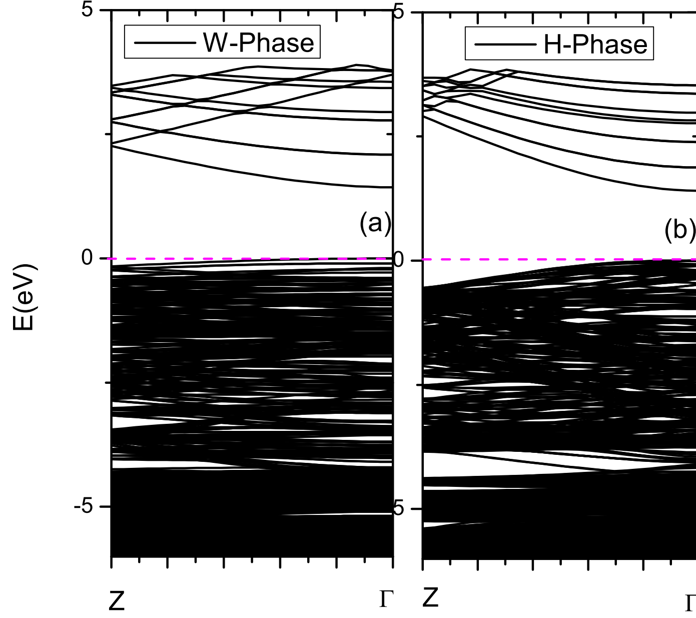

Figure 3.12: The electronic band structure for W phase (a)and H phase (b). (Dashed line for Fermi energy level.)

Combine with the calculation of σ and S, the power factor ($P = S^2\sigma$) vs n_e (carrier concentration) for both W phase and H phase is shown in Figure 3.13(a).There is an optimal carrier concentration N_{max} to achieve the maximum value of the power factor for both the two phases. The maximum value of the power factor for H phase is larger than that of W phase due to its high electrical conductivity. The N_{max} for ZT is located at $6.5 \times 10^{18}(cm^{-3})$ for H-phase and $7.09 \times 10^{18}(cm^{-3})$ for W-phase. The thermal conduction is also influenced by the phase transition. The total thermal conductivity contains both the electronic thermal conductivity and phonon thermal conductivity. Here, the electronic thermal conductivity can be

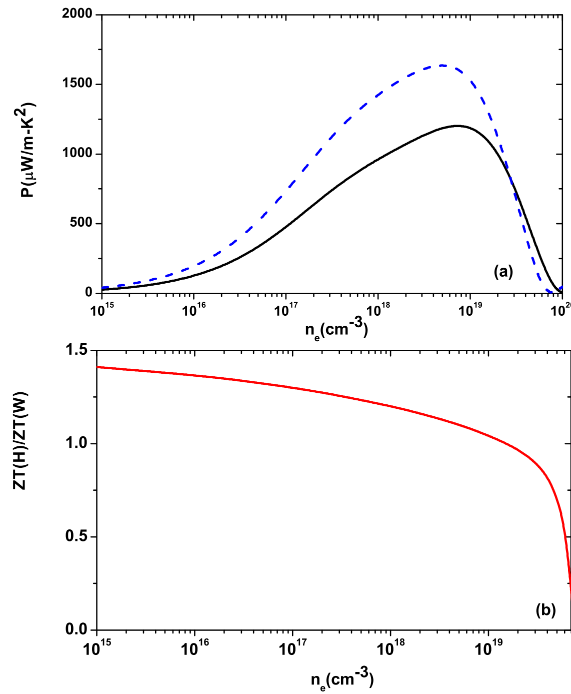

Figure 3.13: The power factor vs carrier concentration for both W phase (solid line) and H phase (dashed line) (a) ; The relative value of ZT(H)/ZT(W) vs carrier concentration (n_e)(b)

neglected compared with that of the phonon thermal conductivity. The phonon thermal conductivity for H-phase is 20% higher than that for W-phase in Ref. [55]. Combined with the calculation of power factor and the thermal conductivity, we obtain the thermoelectric figure of merit ZT for both W-phase and H-Phase. Figure 3.13(b) shows the relative value of ZT for both W-phase and H-Phase vs n_e(carrier concentration). The achieved ZT for H-phase is a bit larger than that for W-phase in most range of carrier concentration because of the larger power factor from the high electrical conductivity. The maximum achievable value of figure of merit ZT for H phase is larger than that for W phase (1.1 times).

In this section, we use the Boltzmann transport equation and first principle method to investigate the thermoelectric properties in [0001] ZnO nanowires. Our results show that the electronic band gap of ZnO NWs for Wurtzite (W) phase is larger than that of Hexagonal (H) phase. For a certain carrier concentration, the Seebeck coefficient S for W-phase is larger than that for H-phase, while electrical conductivity with H-Phase is much higher than that of W-Phase because of the higher electron mobility in H-Phase. There is an optimal carrier concentration to achieve the maximum value of power factor P for both W and H phases. The maximum value of P (P_{max}) for H phase ($P_{max} = 1638\mu W/m - K^2$) is larger than that of W phase ($P_{max} = 1213\mu W/m - K^2$) due to its high electrical conductivity. The maximum achievable value of figure of merit ZT for H phase is larger than that for W phase ($1.1 times$). Our work provides design rules for possible ZnO NW arrays based piezoelectric, optoelectronic and thermoelectric hybrid energy generator.

3.6 Thermoelectric Figure of Merit in Ga-Doped [0001]ZnO Nanowires

We focus on ultrathin NWs oriented along the [0001] direction with the diameter about $0.7nm$. The atomic structure of NW is initially constructed from bulk wurzite structure of ZnO solid. The Zn atoms are randomly substituted by Ga atoms and the geometry is relaxed to its closest minimum total energy. A supercell approach is adopted where each wire is periodically repeated along the growth direction. The size of the supercells in the transverse plane is large enough ($> 15\mathring{A}$ from surface to surface). Two repeated units along the growth direction are required for NWs and the relaxed supercell length along the wire axis is about $10.4\mathring{A}$ [53]. The total atom number of pure ZnO NWs is 52, with 26 Zn atoms and 26 Oxide atoms. In this work, the density functional theory (DFT) calculations are carried out by $DMol3$ package [93].The DFT calculations are performed by using generalized gradient approximation with the functional parameterized by Perdew, Burke, and Ernzerhof [94]. And the double-numerical-polarization basis set is employed. Self-consistent field calculations are done with a convergence criterion of 10^{-6} hartree on the total energy. The Brillouin zone integration is performed using a $1 \times 1 \times 16$ Monkhorst-Pack k-point grid. All the structures are fully optimized with a convergence criterion of $0.002hartree/\mathring{A}$ for the forces and $0.005\mathring{A}$ for the displacement. A real-space cutoff of $4.0\mathring{A}$ for the atom-centered basis set is chosen to increase computational efficiency while not significantly affecting the magnitude of inter-atomic forces or the total energies. The Gaussian smearing of electron density is applied with the energy range of $0.1eV$.

The electrical conductivity σ , the thermal conductivity due to electrons κ_e, and the Seebeck coefficient S, are obtained from the electronic structure with the solution of one-dimensional Boltzmann transport equation as described in Ref. [46, 47]. Here we use the experimental data of film [low carrier concentration σ $(20-30)(\Omega cm)^{-1}$, $n = 6.0 \times 10^{20}(\Omega cm)^{-1}$ from Ref. [100]] and the dependence relation [101] between the mobility and carrier concentration to calculate the carrier concentration dependent relaxation time. The carrier concentration is defined as:$n = \int_0^\infty f(E)D(E)dE$, where $f(E)$ is the Fermi distribution function.

Figure 3.14 show the atomic structure of the NW for $x = 0.04$ with the replacement of one Zn atom [(a)and (b)are for top view and side view, respectively]. $x = 0.08$ and 0.12 correspond to two and three Zn atoms are substituted with Ga atoms, respectively. Figure 3.15 shows the total density of states (DOS) of $Zn_{1-x}Ga_xO$ NWs ($x = 0(a), 0.04(b), 0.08(c)$). For pure ZnO NW ($x = 0$), the O 2$s$ states are located around $-18eV$, which have little interaction with the other valence band. The valence band consists of two main states, Zn 3d and O 2p orbitals. The Zn 4s states dominate the conductance band. With the Ga content (x) increase, on the one hand, there is charge transfer from Zn 4s states to O 2p states, thus results in the shift of the center of gravity of the DOS at the O sites towards the low energy regions and the Fermi energy level into the conduction band (See Fig. 3.15), which indicates the n-type characteristics of $Zn_{1-x}Ga_xO$ wires. And on the other hand, the dopant states, (Ga 4s states and Ga 3d states) appear following the O 2s states. Similar phenomena can be observed in Ga-doped bulk ZnO [102].

Figure 3.16 shows the Ga content (x) dependence of electronic band gap and carrier concentration. It is obvious that for each Ga content, the band gap values depend

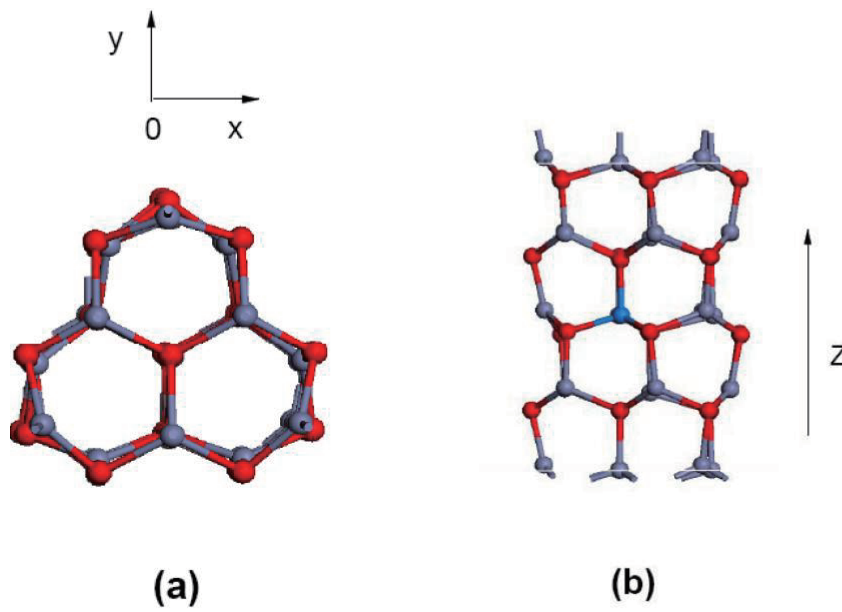

Figure 3.14: The atomic structure of ZnO nanowires with diameter of 0.7nm;(a)is top view and (b)is side view; Red: O atom; Gray: Zn atom; Blue: Ga atom.

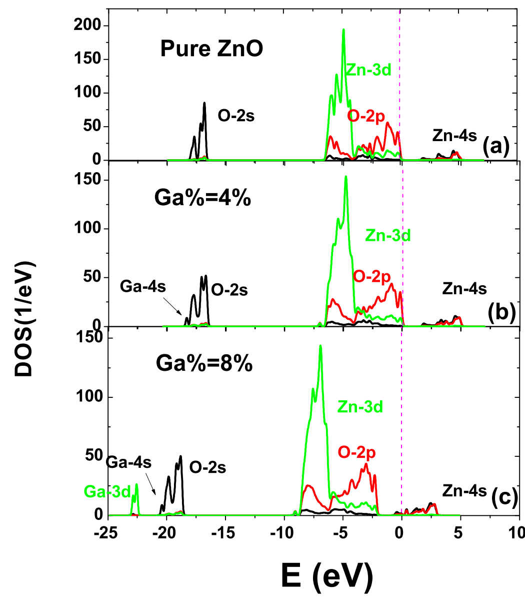

Figure 3.15: The total DOS for $Zn_{1-x}Ga_xO$ NWs for (a) $x = 0$;(b)0.04;(c) 0.08. The Fermi energy is set to 0. The dashed magenta line is used to guide the eyes.

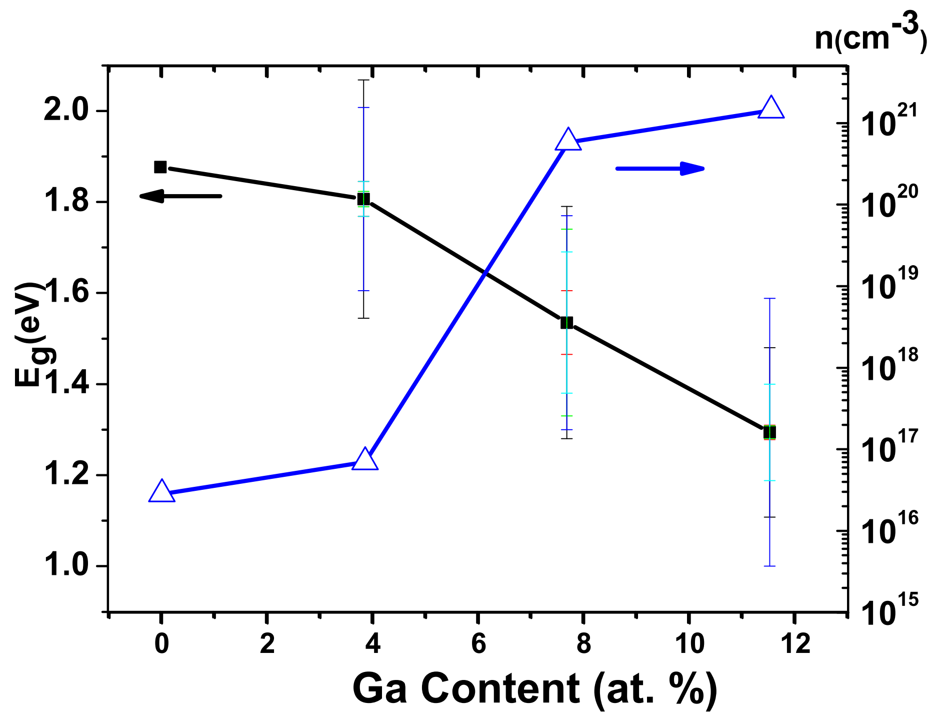

Figure 3.16: The averaged electronic band gap for $Zn_{1-x}Ga_xO$ NWs and carrier concentration versus Ga contents.

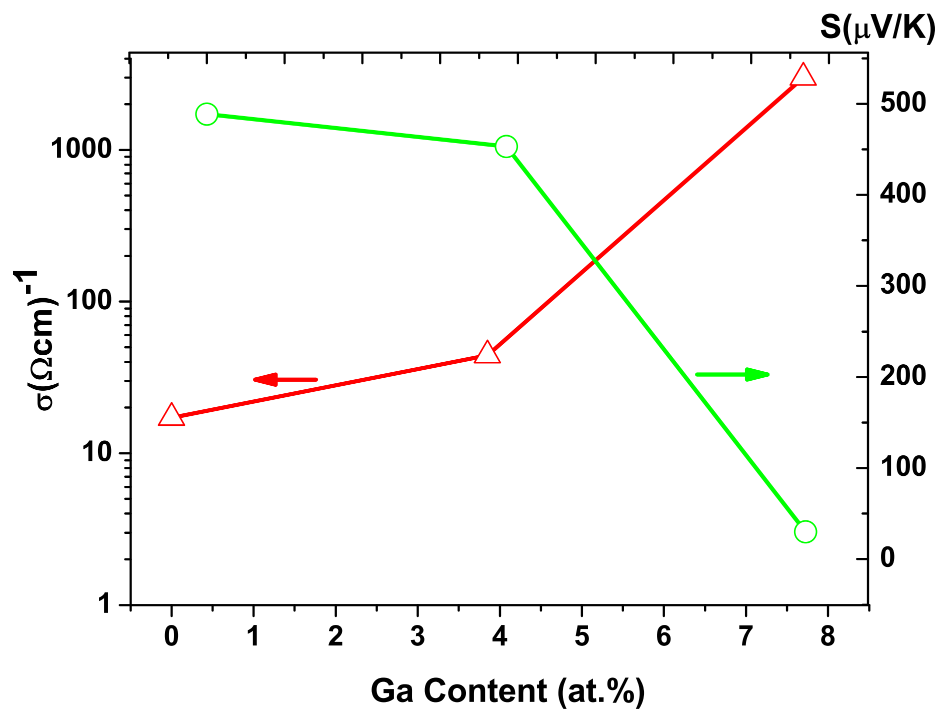

Figure 3.17: σ , S vs Ga content x.

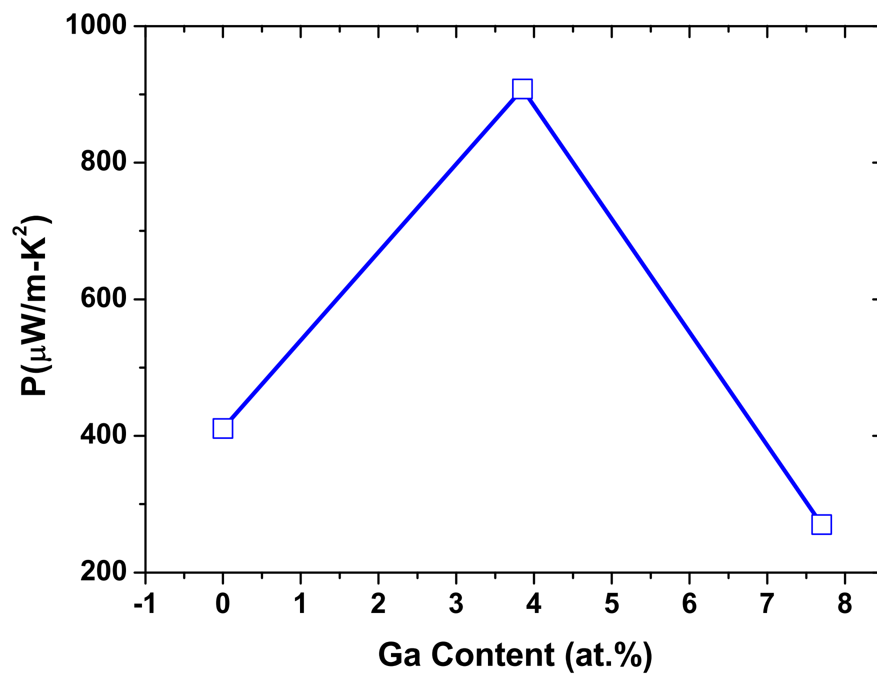

Figure 3.18: Thermal power factor of $Zn_{1-x}Ga_xO$ NWs versus Ga contents.

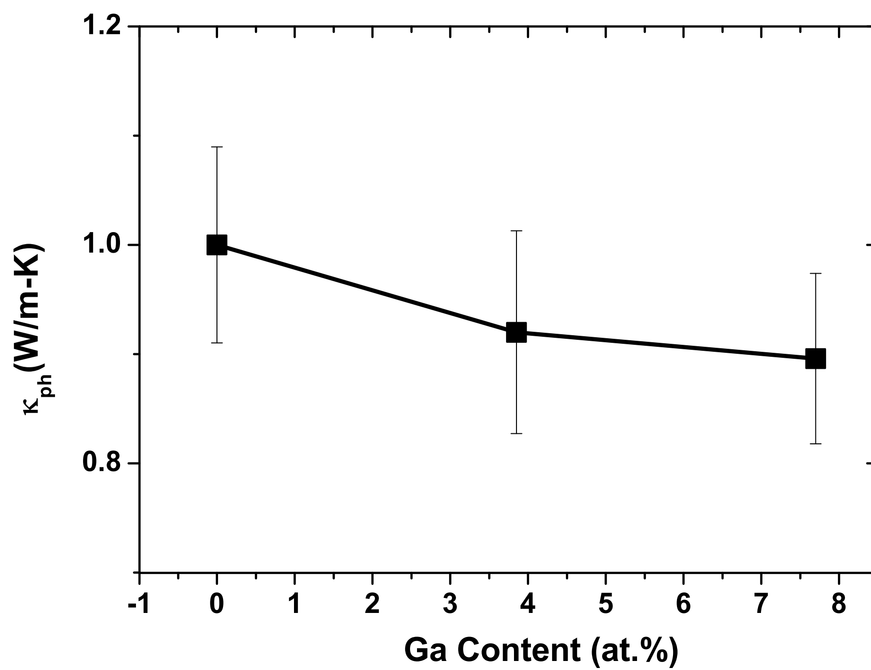

Figure 3.19: Relative value of phonon Thermal conductivity for $Zn_{1-x}Ga_xO$ NWs compared with that for pure ZnO wires versus doping contents.

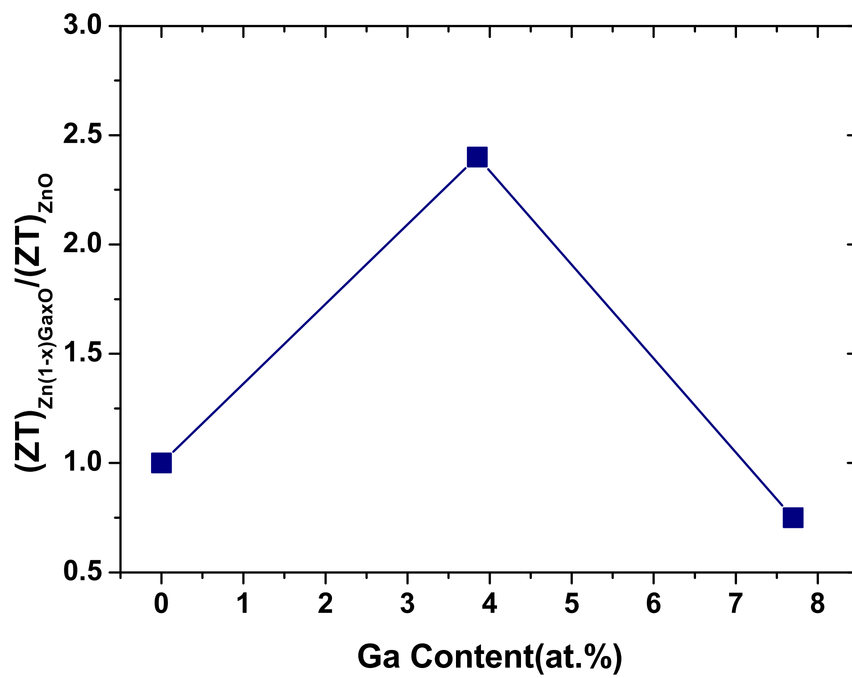

Figure 3.20: Relative value of ZT for $Zn_{1-x}Ga_xO$ NWs compared with that for pure ZnO wires versus the Ga content.

on the detailed atomic structures. In order to reduce the fluctuation, the results are averaged by over five realizations as we did in SiGe NWs [47]. With Ga content (x) increase, the averaged band gap decreases. This is consistent with the experimental observed energy band gap in [103]. In the following calculation of the thermoelectric properties, the DOS of specific NW structure is used, which is most stable with the lowest total energy. The carrier concentration increases as the Ga content increase. We can obtain a high electron concentration about $1.43 \times 10^{21} (cm^{-3})$ at $x = 0.12$. However, the maximum electron concentration achieved in ZnO NWs via doping method is about in the order of $10^{20} (cm^{-3})$ [104], and thus the maximum Ga doped content (x) we consider in our paper can not exceed 0.08 ($n = 6.0 \times 10^{20} (cm^{-3})$). Figure 3.17 shows the Ga content dependence of σ and S. σ increases and S decreases as the Ga content increases because there are more charge transport. At low carrier concentration range, the Seebeck coefficient is about $400\mu V/K$, which is in good agreement with the experimental observation in Ref. [73]. Figure 3.18 shows the power factor ($P = S^2\sigma$) versus the Ga content. There is an optimal Ga content ($x = 0.04, n = 1.0 \times 10^{17} (cm^{-3})$) yielding the maximum attainable value of power factor ($P_{max} = 908\mu W/m - K^2$).

ZT is one of the central physical quantities that determine the efficiency of thermoelectric application. In the calculation of ZT, both electron and phonon contributions to the total thermal conductivity are counted. To calculate the phonon thermal conductivity of $Zn_{1-x}Ga_xO$ NW by using molecular dynamics simulations, the potential that describes the interactions between the atoms is needed,[55]. However, there is no consensus in the literature about the potential that describes the interactions between Ga atom and Zn, O atoms. In the $Zn_{1-x}Ga_xO$ NW,

compare to the original Zn atom, the doped Ga atom has different atomic mass and different interaction with the neighboring atoms. Through the investigation of thermal conductivity by using molecular dynamics simulation, it has been demonstrated that the difference in atomic mass has larger impact on thermal conductivity than the different interaction does [21]. Thus here we use the Buckingham potential[99] to describe the atomic interaction in $Zn_{1-x}Ga_xO$. In the molecular dynamics simulation, there are 20 unit cells in the longitudinal direction which corresponds to a length of $10.4nm$, and the wire diameter is $0.7nm$, the same as that in the DFT calculation. Figure 3.19 shows the phonon thermal conductivity decreases as the Ga content increases. Compare to the 60% thermal conductivity reduction (with $x = 0.1$) in $Si_{1-x}Ge_x$ NW, the thermal conductivity reduction in $Zn_{1-x}Ga_xO$ NW is only about 10%, due to the small difference in atomic masses between Zn and Ga atoms [18].

Combined with the calculations of the power factor and the phonon thermal conductivity, we show the Ga content dependent ZT in Figure 3.20. The value of ZT firstly increases with the Ga content, reaches a maximum value at $x = 0.04$, which is 2.5 times larger than that of pure ZnO wires, and then decreases. This phenomena can be explained as follows: ZT is contributed by both power factor and thermal conductivity. With Ga content (x) increase, the power factor increases, reaches a maximum value at $x = 0.04$ and then decreases. The curve of the thermal conductivity decreases with the Ga content increase. However, when $0 \leq x \leq 0.04$, the increase in the power factor is larger than the reduction in the thermal conductivity, thus results in the increase in ZT with the Ga content. And when $0.04 \leq x \leq 0.08$, the reduction in the thermal conductivity can not offset

the reduction in the power factor, thus results in the decrease in ZT with the Ga content. It is worth to mention that the optimal carrier concentration yielding the maximum attainable value of ZT is $1.0 \times 10^{17} cm^{-3}$. This low carrier concentration suggests that the high thermoelectric performance of Ga-doped ZnO NW can be realized by using reliable fabrication technology.

In summary, we have investigated the Ga content dependent thermoelectric properties of $Zn_{1-x}Ga_xO$ nanowires. It is found that the thermoelectric performance is strongly dependent on the Ga content. The Ga doping reduced the thermal conductivity of ZnO NW, down to less than 90% at Ga content of 0.08. The maximum attainable ZT corresponds to a optimal Ga content of $x = 0.04$, which is 2.5 times of that of the pure ZnO wires. Our work provides design rules for possible ZnO NW arrays based piezoelectric, optoelectronic and thermoelectric hybrid energy generator.

Chapter 4

Significant Enhancement of Thermoelectric Figure of Merit in [001] $Si_{0.5}Ge_{0.5}$ Superlattice Nanowires

In this chapter, we combine the density functional theory (DFT) and nonequilibrium Green's Function (NEGF) to investigate the thermoelectric properties of [001] $Si_{0.5}Ge_{0.5}$ superlattice (SL) nanowires (NWs)with diameter $1.2nm$. Firstly, we would like to achieve the enhanced thermoelectric figure of merit ZT in the SL NWs compared with that of pure Si NWs. Our results show that for the charge

transport(electrons and holes), the charge transmission of the SL NWs is decreased sharply compared with pure Si NWs. The Si NWs have higher electronic conductance and lower Seebeck coefficient. As a result, the optimal thermal power factor of pure Si NWs is higher than that of SL NWs. While for the phonon transport, a large reduction of phonon thermal conductance is found in SL NWs compared with that in pure Si NWs. Secondly, we investigate the effect of the interfaces of SL NWs on the thermoelectric figure of merit ZT. The maximum value of optimal thermal power factor occurs at the period length $L = 0.54nm$. And the phonon thermal conductance curve firstly decreases with the period length L increase, reaching a minimum value at $L = 0.54nm$, and then increases when further increasing L. Finally, the ZT curve firstly increases, reaching a maximum value at $L = 0.54nm$ and then decreases with the further increase of L. A large enhancement of ZT is found in our studied SL NWs. For n-type SL NWs, the achieved maximum value of ZT is 4.7, which is 5.0 times larger than that of pure Si NWs ($ZT = 0.94$), while for p-type wires, the achieved maximum value of ZT is 2.7, which is 4.5 times larger than that of pure Si NWs ($ZT = 0.6$).

4.1 Introduction

Superlattice(SL) Nanowires(NWs)have been fabricated experimentally with tens and hundreds of diameters. Superlattice(SL) Nanowires(NWs) have recently attracted broad interest in recent years due to their fascinate applications in photonics,electronics and phononics [105–107]. The SL NWs can act as nanobarcodes [105], nanolasters [106], $1D$ waveguide and resonant tunneling diodes [107]. The

SL NWs have also exhibited more advantages than the conventional $1D$ nanowires [28] and $2D$ superlattices [30, 32] due to their strong quantum confinement effects. The SL NW is attractive especially in the thermoelectric applications because the interface between two different NW's materials can scatter the phonons strongly, thus reducing the thermal conductivity. The thermal conductivity of SL NWs is widely studied. Yang *et al*[18] used the isotopic-superlattice structured Si NWs to reduce the thermal conductivity with the molecular dynamics simulations. They found that at a critical period of SL NWs, the thermal conductivity is only 25% of the pure Si NWs. Chen *et al.* [21] also used the molecular dynamics simulations to investigate the reduction in the thermal conductivity of the silicon(Si) and germanium(Ge) superlattice nanowires. Their work show that at a critical period length, the thermal conductivity is only one sixth of the pure Si NWs. In conclusion, using the SL NWs could effectively reduce the thermal conductivity of nanowires.

The thermoelectric performance is evaluated by the dimensionless thermoelectric figure of merit ZT ($= \frac{S^2 G_e}{\lambda} T$). Here, S is the Seebeck coefficient, G_e is the electronic conductance, T is the absolute temperature and λ is the thermal conductance. $\lambda = \lambda_e + \lambda_p$, where λ_e is the electronic contribution to the thermal conductance and λ_p is the phonon contribution to the thermal conductance. A low thermal conductance is required for a high thermoelectric figure of merit ZT. As a result, the SL NWs are good candidates for the thermoelectric applications because of their low thermal conductivity. Several theoretical work have also been concerned with the thermoelectric properties of the SL NWs. Dresselhaus *et al* [108] used the Boltzmann transport equation to investigate the thermoelectric property of superlattice nanowires. They found that thermoelectric properties of SL NWs

were influenced by period length, wire diameter, growth direction and the length ratio of the two different segments. They predicted that values of ZT higher than 4 and 6 could be obtained in $PbSe/PbS$ and $PbTe/PbSe$ superlattice nanowires. In their work, the superlattice nanowires are expected to enhance the thermal power factor beyond the conventional nanowires and superlattices.

In this work, we combine the density functional theory (DFT) and nonequilibrium Green's Function (NEGF) to investigate the thermoelectric properties of $Si_{0.5}Ge_{0.5}$ superlattice nanowires with diameter about $1.2nm$. Firstly, we aim to study the interface effects on the thermoelectric properties of the SL NWs. For the electronic conduction, we combine the Density Functional theory (DFT) and nonequilibrium Green's Function (NEGF), which is implemented in TRANSIESTA package, to obtain the electronic transmission, while for the phonon conduction, we use the density functional theory (DFT), which is implemented by Siesta package, to obtain the force-constant matrix, and then calculate the phonon transmission. This method is widely used to investigate the electron transport and phonon transport in nanostructured systems. Markussen *et al.* used this method to compute the electron and phonon transmission in the disordered silicon nanowires (Si NWs) [109]and surface-decorated Si NWs [110].

4.2 Computation Methods

We focus on the [001] $Si_{0.5}Ge_{0.5}$ superlattice(SL) nanowires (NWs), which contains the alternative Si and Ge layers with the varied period length in the longitude

direction. The NWs have the fixed total length with four unit cells of bulk Si (192 atoms) and their diameter is about $1.2nm$. The surface dangling bonds are terminated with Hydrogen (H) atoms. In order to investigate the transport properties of the SL NW, we devise a two probe system, $Si/Si_{0.5}Ge_{0.5}SLNW/Si$. The central region $Si_{0.5}Ge_{0.5}$ SL NW is connected by two semi-infinite Si electrodes, whose surfaces are also terminated with Hydrogen(H) atoms.

For the charge (electrons and holes) transport, we use the Transiesta package, which is based on the density functional theory (DFT) and nonequilibrium Green's Function (NEGF) to calculate the electrons'(holes')transmission of the SL NWs when the applied voltage is zero. All the structures are fully relaxed until the force on each atom is less than $0.04eV/\AA$. The single-zeta plus polarization (SZP) basis set is employed. The Brillouin zone Integration is performed using Gama point grid.We use norm-conserving pseudopotentials and the local density approximation for exchange correlation energy. For the phonon transport, we use the density functional theory (DFT), which is implemented by Siesta package, to obtain the force-constant matrix. We use nonequilibrium Greens-Function (NEGF) to calculate the phonon transmission function of Si/NW/Si. In order to obtain the accurate phonon transmission, we use Double-zeta (DZ) basis set and all the structures are fully relaxed until forces on each atom are less than $0.01eV/\AA$.

We use the ballistic transport equations to study the thermoelectric properties of the SL NWs. This method is widely used to investigate the thermoelectric properties of the SL NWs, [50, 109, 110]. The transport coefficient can be written as follows:

The electronic conductance:

$$G_e = e^2 L^{(0)}(\mu) \tag{4.1}$$

The electronic thermal conductance:

$$\lambda_e = \frac{1}{T}[L^{(2)}(\mu) - L^{(1)}(\mu)[L^{(0)}(\mu)]^{-1}L^{(1)}(\mu)] \tag{4.2}$$

The Seebeck coefficient:

$$S = \frac{1}{eT}(L^{(0)}(\mu))^{-1}L^{(1)}(\mu) \tag{4.3}$$

$$L_m(\mu) = \frac{2}{h}\int_{-\infty}^{\infty} dET_e(E)(E-\mu)^{(m)}(-\frac{\partial f(E)}{\partial E}) \tag{4.4}$$

Here e is the charge. μ is the chemical potential. h is the Planck constant. E is the electron (or hole) energy. T is the absolute temperature. $T_e(E)$ is electron(or hole)transmission. $f(E)$ is the Fermi-Dirac distribution.

The phonon thermal conductance λ_p is given by:

$$\lambda_p(T) = \frac{\hbar^2}{2\pi k_B T^2}\int_0^{\infty} d\omega\omega^2 T_{ph}(\omega)\frac{e^{\frac{\hbar\omega}{k_BT}}}{(e^{\frac{\hbar\omega}{k_BT}}-1)^2} \tag{4.5}$$

where ω is phonon frequency; T_{ph} is phonon transmission;

4.2.1 Results and Discussion

Figure 4.1 shows the geometry of the $Si_{0.5}Ge_{0.5}$ superlattice (SL) nanowires (NWs) at the period length $L = 1.08nm$. The period length $L = 0.27nm$, $0.54nm$, $1.08nm$ and $2.16nm$ are denoted by $SG1, SG2, SG3, SG4$.

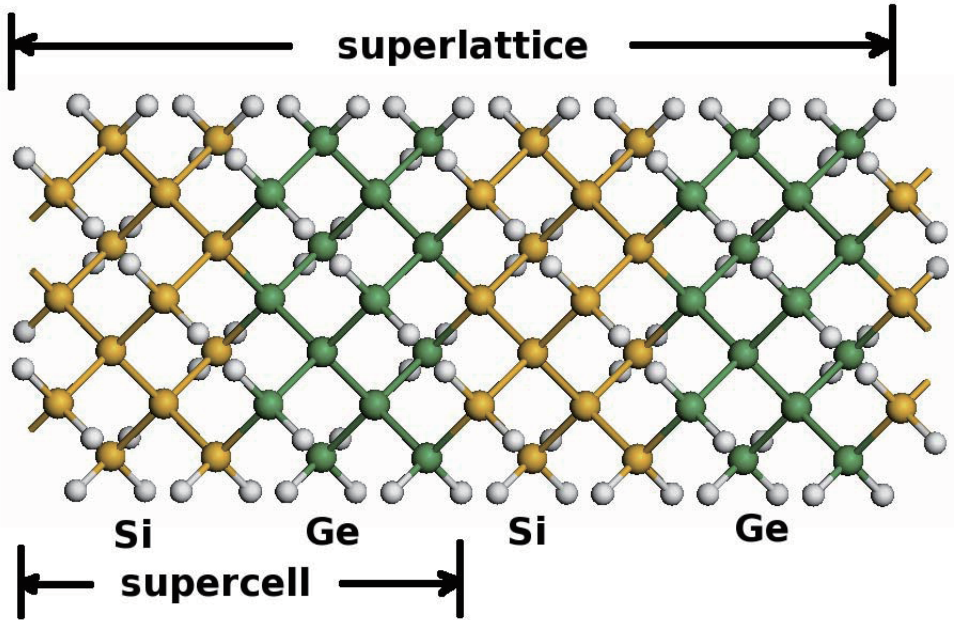

Figure 4.1: The geometry of the $Si_{0.5}Ge_{0.5}$ superlattice nanowires with the period length $L = 1.08nm$; Yellow:Si atom; Green:Ge atom; White:H atom.

Figure 4.2 and 4.3 show the hole and electron transmission spectra $T(E)$ versus energy for $Si_{0.5}Ge_{0.5}$ superlattice (SL) nanowires (NWs) and pure Si NWs. It is found that for pure Si NWs, both the hole and electron transmission have the perfect transmission, while for the SL NWs, the hole and electron transmission decrease sharply due to the scatterings from different atoms. Moreover, the transmission for the cases $L = 0.27nm$ and $L = 0.54nm$ is larger than that of the cases

$L = 1.08nm$ and $L = 2.16nm$. We can explain this phenomenon from the projected density of states (PDOS) on the Si and Ge atoms of the SL NWs. Figure 4.4 and 4.5 show the projected density of states on Si and Ge atoms for p-type and n-type SL NWs,respectively. For the cases $L = 0.27nm$ and $L = 0.54nm$, within the considered energy range, the density of states (DOS) spectra projected on the Si and Ge atoms overlaps with each other perfectly, while for the cases $L = 1.08nm$ and $L = 2.16nm$, the density of states (DOS) spectra projected on the Si and Ge atoms have obvious differences. When the density of states projected on the Si and Ge atoms overlaps each other very perfectly, high transmission is achieved. This is the reason why the transmission for the cases $L = 0.27nm$ and $L = 0.54nm$ is larger than those of the cases $L = 1.08nm$ and $L = 2.16nm$.

After we obtain the hole and electron transmission, the electronic conductance G_e, the Seebeck coefficient S and the thermal power factor P can be achieved. Figure 4.6 and 4.7 show the electronic conductance versus energy in the valence band and the conduction band for both SL NWs and pure Si NWs, respectively. For the pure Si NWs, the charge (hole and electronic) conductance has the plateau, while for the SL NWs, the conductance decreases sharply compared with that of the pure Si NWs. Figure 4.8 and 4.9 show the Seebeck coefficient S versus energy in the valence band and the conduction band, respectively. S decreases with the energy increase for both holes and electrons within most energy range and there are also a series of peaks in the curves, which derive from the peaks in the transmission spectra.

Figure 4.10 and 4.11 show the thermal power factor as a function of energy in the valence band and the conduction band for both SL NWs and pure Si NWs. There

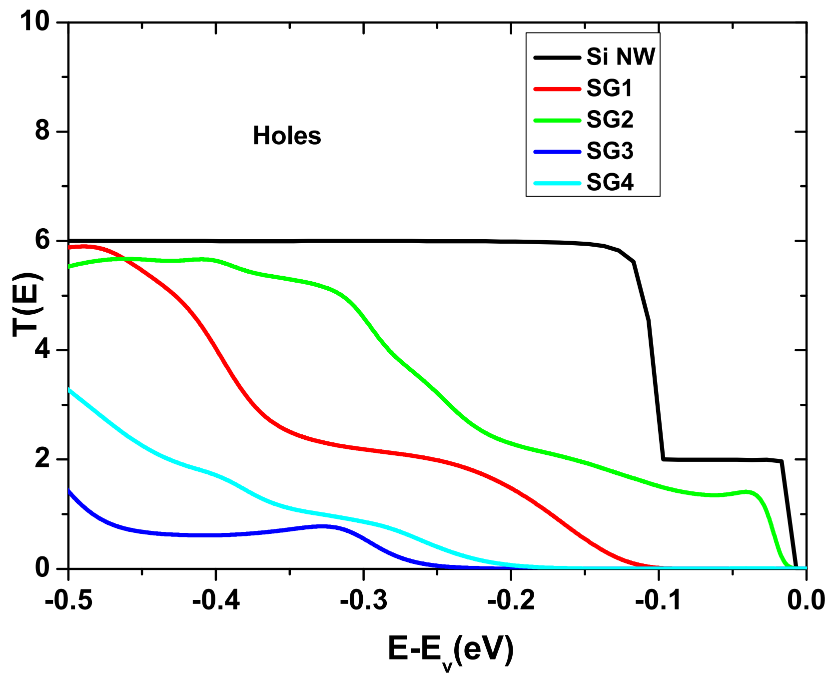

Figure 4.2: The hole transmission for the $Si_{0.5}Ge_{0.5}$ superlattice(SL) nanowires(NWs) and pure Si NWs. The energy scale is relative to the valence band edge.

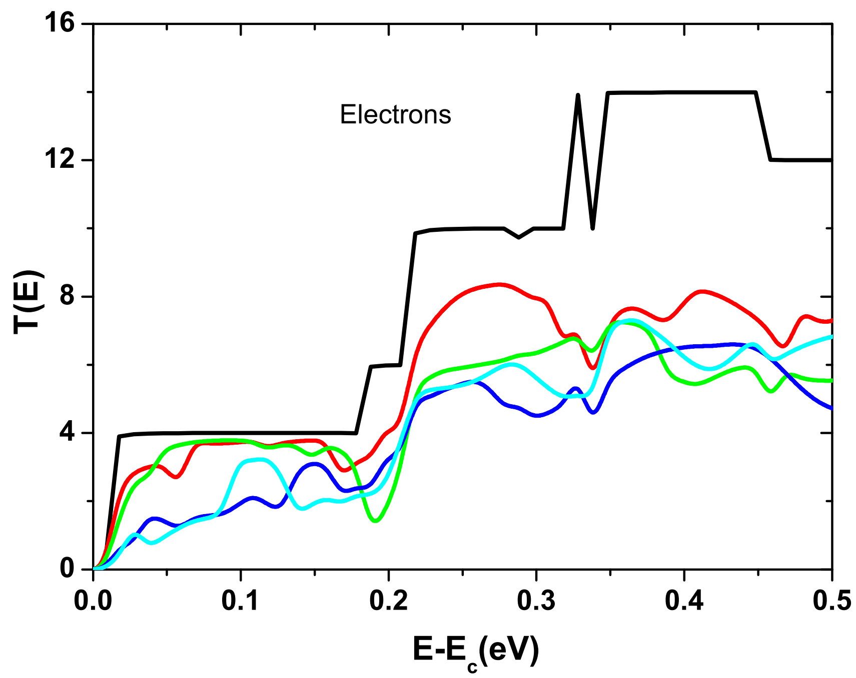

Figure 4.3: The electron transmission for the $Si_{0.5}Ge_{0.5}$ superlattice(SL) nanowires(NWs) and pure Si NWs. The energy scale is relative to the conduction band edge.

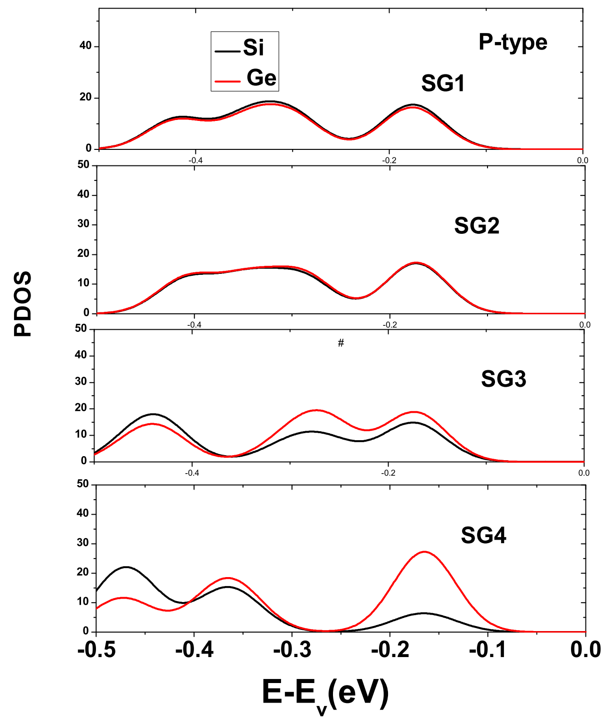

Figure 4.4: Projected density of states (PDOS) on Si and Ge atoms for the p-type SL NWs.The energy scale is relative to the valence band edge.

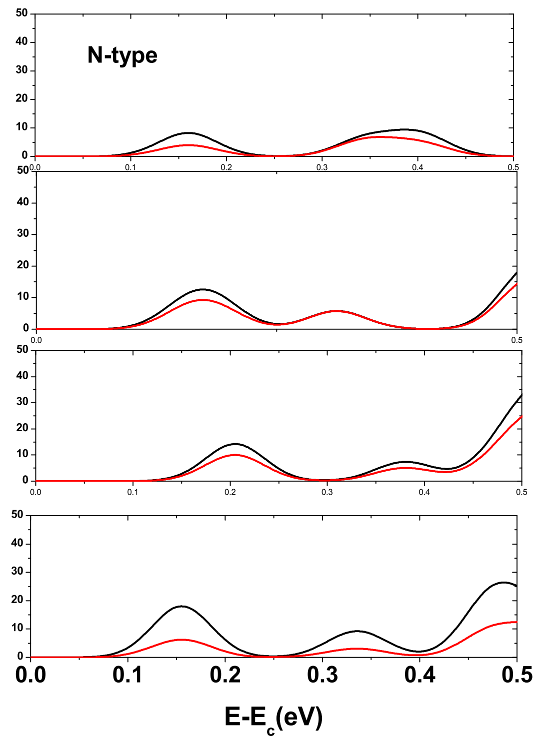

Figure 4.5: Projected density of states (PDOS) on Si and Ge atoms for the n-type SL NWs. The energy scale is relative to the conduction band edge.

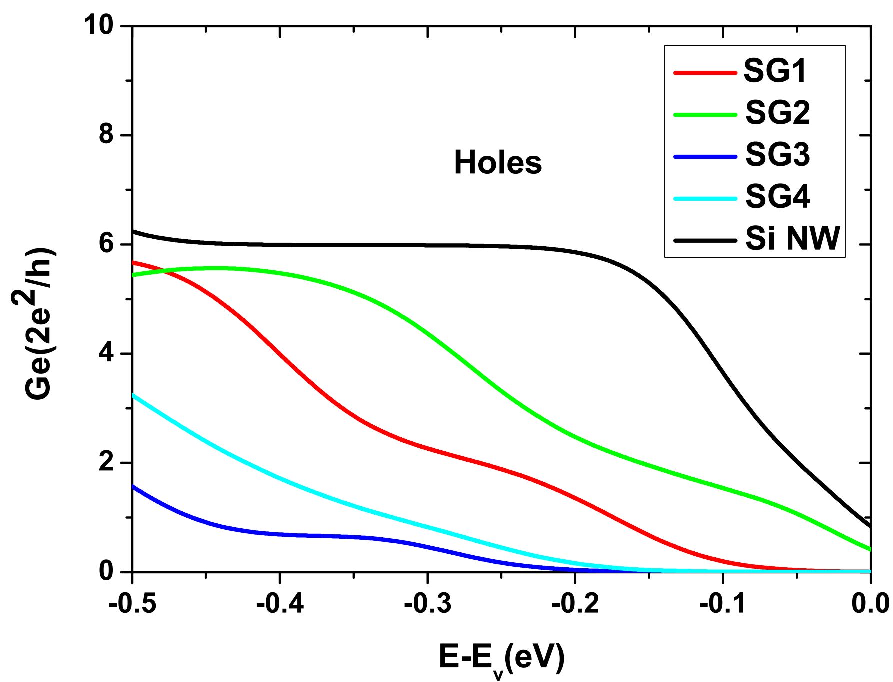

Figure 4.6: The hole conductance for SL NWs and pure Si NWs.The energy scale is relative to the valence band edge.

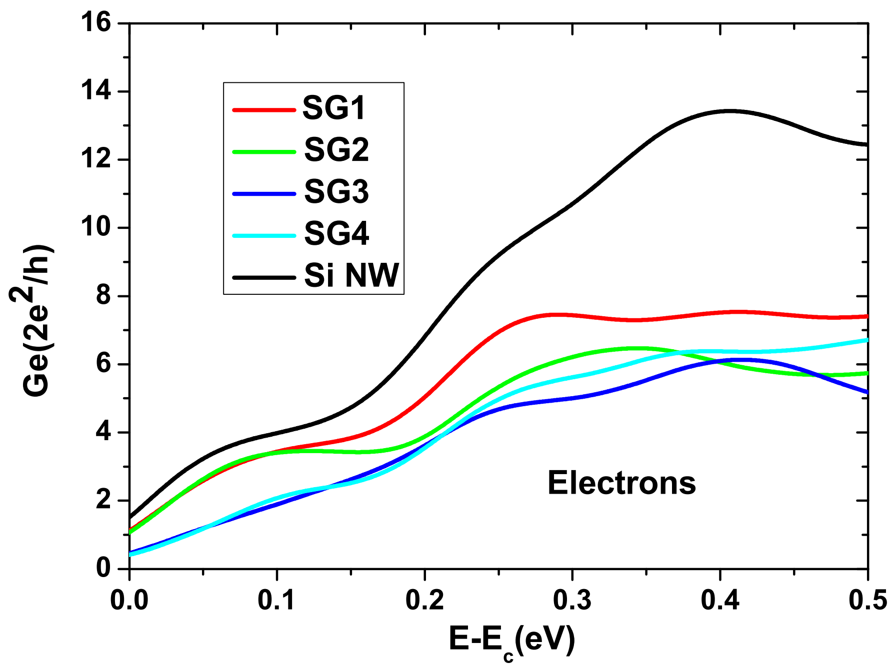

Figure 4.7: The electronic conductance for SL NWs and pure Si NWs. The energy scale is relative to the conduction band edge.

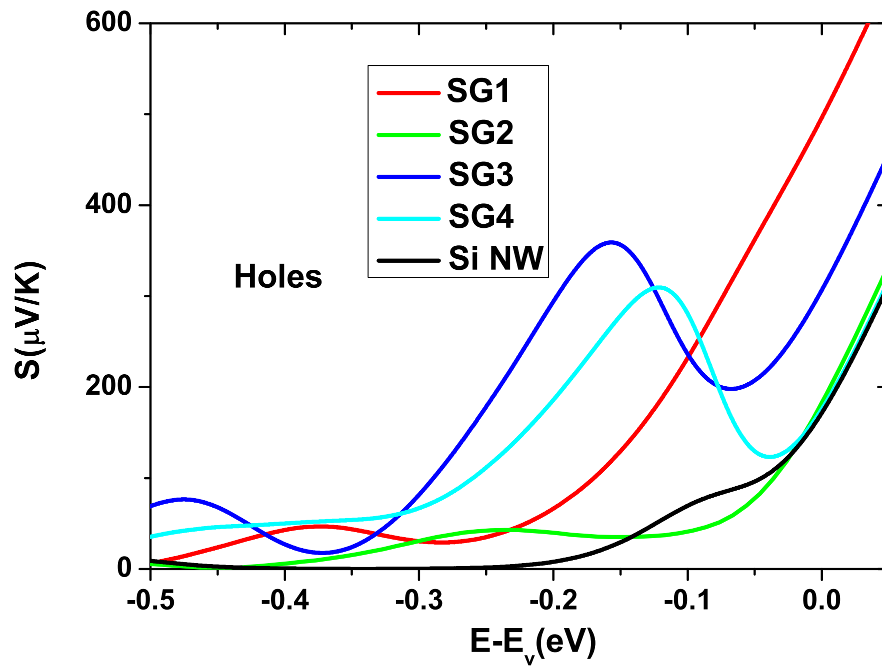

Figure 4.8: The Seebeck coefficient of holes in the valence band for both SL NWs and pure Si NWs. The energy scale is relative to the valence band edge.

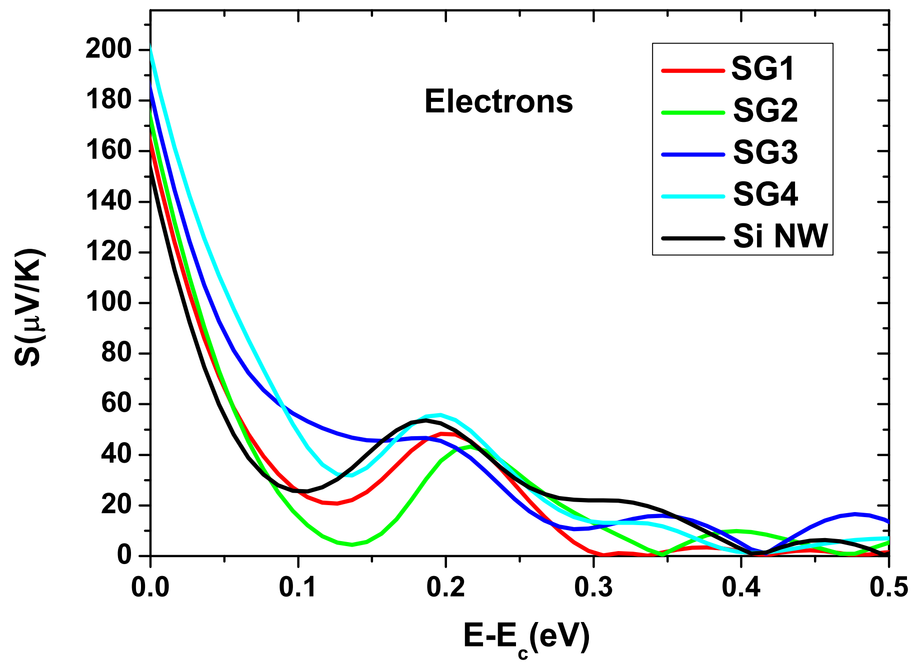

Figure 4.9: The Seebeck coefficient of electrons in the conduction band for both SL NWs and pure Si NWs. The energy scale is relative to the conduction band edge.

is always an optimal energy to achieve the maximum value of thermal power factor P_{max} for both holes and electrons. For the holes case, the optimal energy for pure Si NWs and $SG2(L = 0.54nm)$ occur at the valence band edge, while for electrons case, the optimal energy happens closely to the conduction edges for all the cases referred here. The similar phenomenon has also been found in Ref [110].

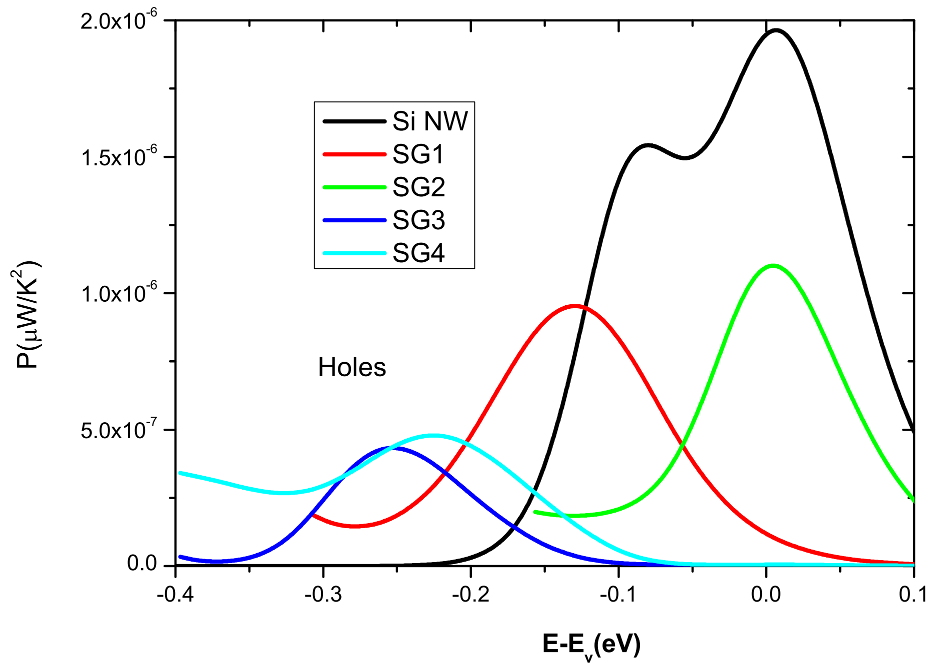

Figure 4.10: The thermal power factor versus energy in the valence band. The energy scale is relative to the valence band edge.

Figure 4.12 show the P_{max} versus period length L for both p-type and n-type cases. For n-type wires, the P_{max} curves firstly increases, reaching the maximum value at $L = 0.54nm$, then decreases and at last increases a bit. The similar behaviors have been found in p-type counterparts, but the values of P_{max} for p-type wires is much smaller than that of n-type ones, about 40% of n-type wires. However, the

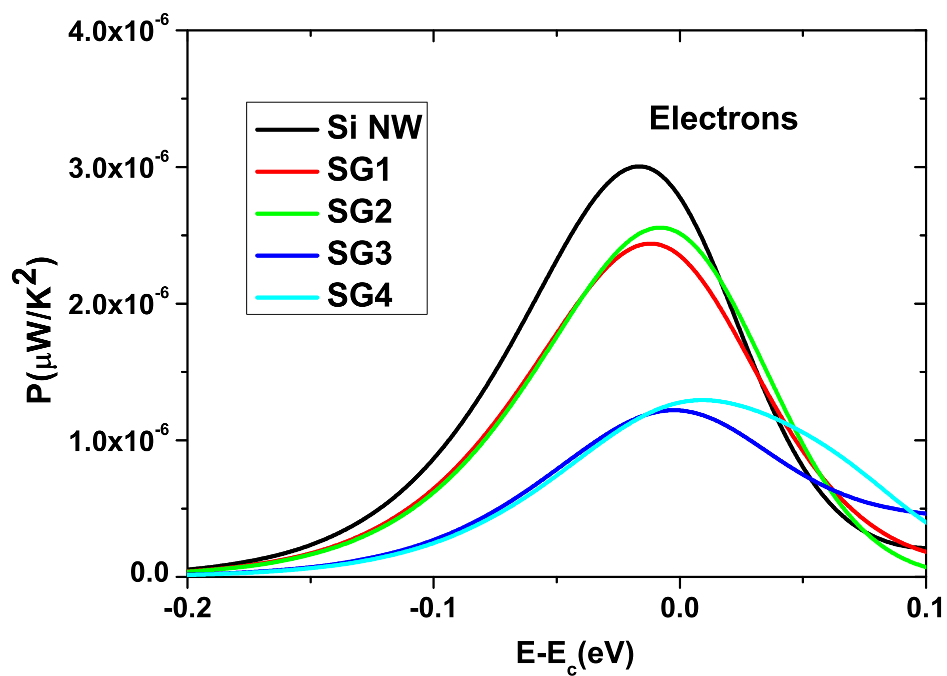

Figure 4.11: The thermal power factor versus energy in the conduction band. The energy scale is relative to the conduction band edge.

values of P_{max} for pure Si NWs are much larger than the cases of SL NWs. The value of P_{max} for n-type Si NWs is $3.03 \times 10^{-6} \mu W/K^2$, which is 1.2 times larger than the maximum value obtained in the SL NWs ($P_{max} = 2.46 \times 10^{-6} \mu W/K^2$ at $L = 0.54nm$) and that for p-type Si NWs is $1.96 \times 10^{-6} \mu W/K^2$, which is almost 1.6 times larger than the maximum value achieved in the SL NW ($P_{max} = 1.25 \times 10^{-6} \mu W/K^2$ at $L = 0.54nm$). The larger P_{max} achieved in Si NWs comes from the higher transmission compared with that in the SL NWs.

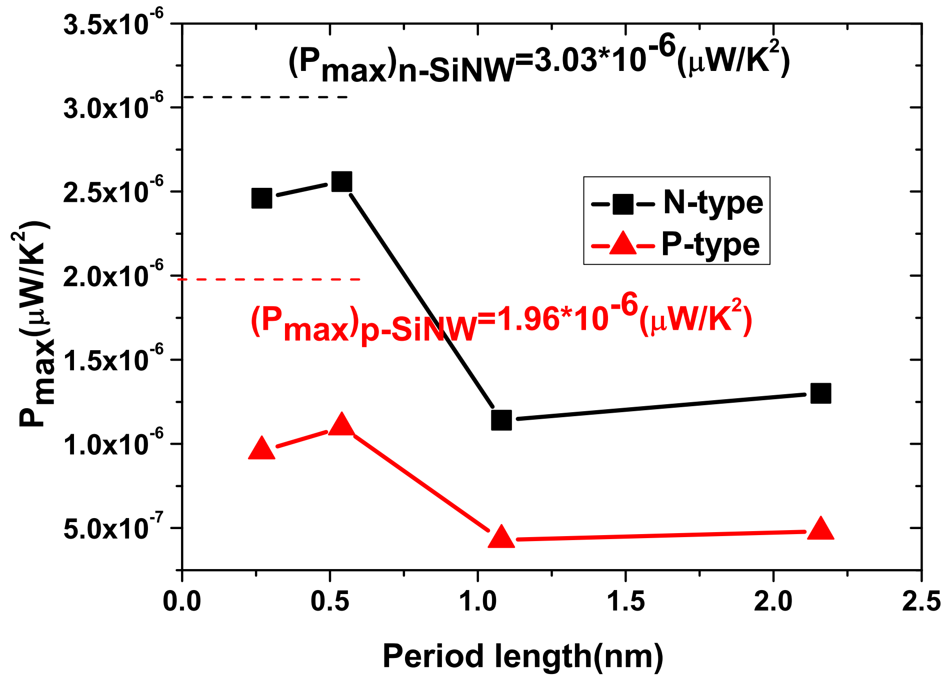

Figure 4.12: The values of P_{max} versus period length L for SL NWs.

The thermal conductance is an important factor in the calculation of ZT and the small thermal conductance leads to large ZT. Both the phonon thermal conductance and the electronic thermal conductance are contributed to the whole thermal

conductance. It is worth pointing out that in our calculation, we neglect electron-phonon and phonon-phonon scattering mechanisms. Considering these scattering mechanisms will result in lower electronic and thermal conductance. Figure 4.13 shows the phonon thermal conductance λ_p and the electronic thermal conductance λ_e versus period length L. The phonon thermal conductance λ_p is largely reduced in the SL NWs compared with that of the pure Si NWs. The maximum value of λ_p achieved in the SL NW at $L = 0.27nm$ is $0.13nW/K$, which is only 16.25% of that of pure Si NW ($\lambda_p = 0.8nW/K$), while the minimum value of λ_p obtained in the SL NW at $L = 0.54nm$ is $0.07nW/K$, which is even 8.75% of that of pure Si NW. And the λ_p curve firstly decreases, reaching a minimum value at a period length $L = 0.54nm$, and then increases with the further increase of the period length. Different cases are obtained for the electronic thermal conductance λ_e for both p-type and n-type wires. The values of λ_e are smaller than that of λ_p. The λ_e curve for p-type wires is similar as that of λ_p curve and the λ_e curve for n-type wires firstly substains and reaches the minimum value at $L = 1.08nm$, then increases with the further increase of the period length L. The values of λ_e for p-type and n-type wires are very close to each other expect at $L = 0.54nm$.

ZT is the most important factor for the thermoelectric materials. Figure 4.14 shows the room-temperature ZT versus the energy μ for both the SL NWs and Si NWs. There is always an optimal energy to achieve the maximum value of ZT in both the valence band and the conduction band. The optimal energy happens closely to the valence band edge and the conduction band edge for both n-type and p-type cases. Figure 4.15 shows the maximum value of ZT (ZT_{max}) versus the period length L for both n-type and p-type wires. The ZT_{max} curve firstly increases, reaches the

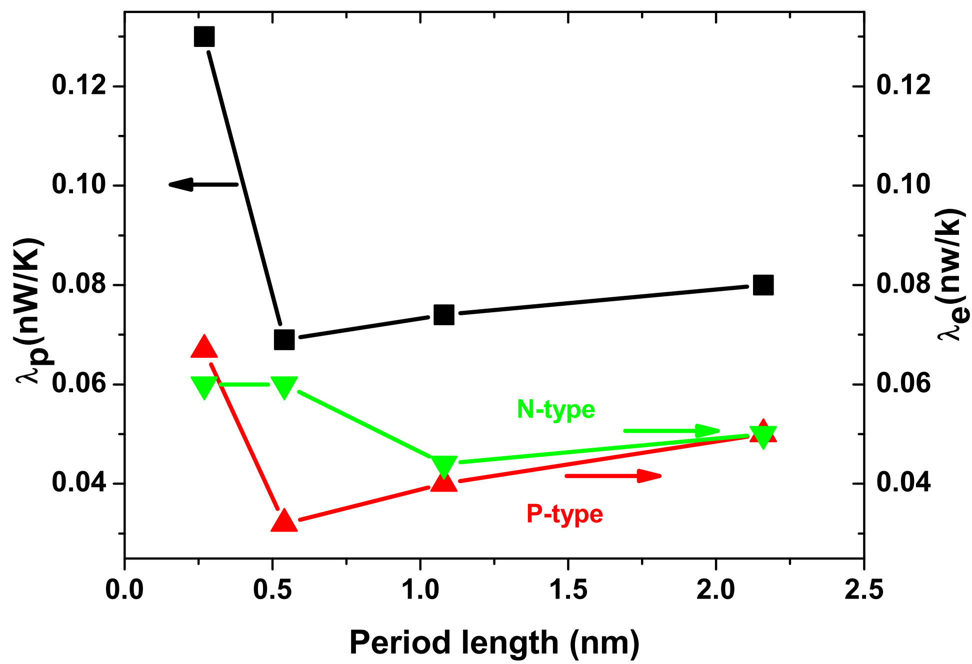

Figure 4.13: λ_p and λ_e versus period length L for SL NWs.

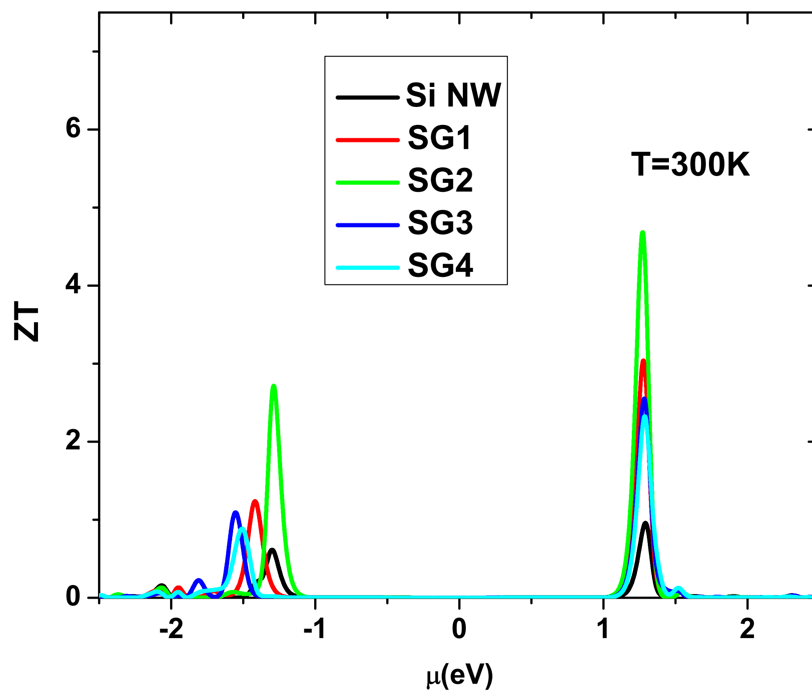

Figure 4.14: ZT versus energy μ for both SL NWs and Si NWs.

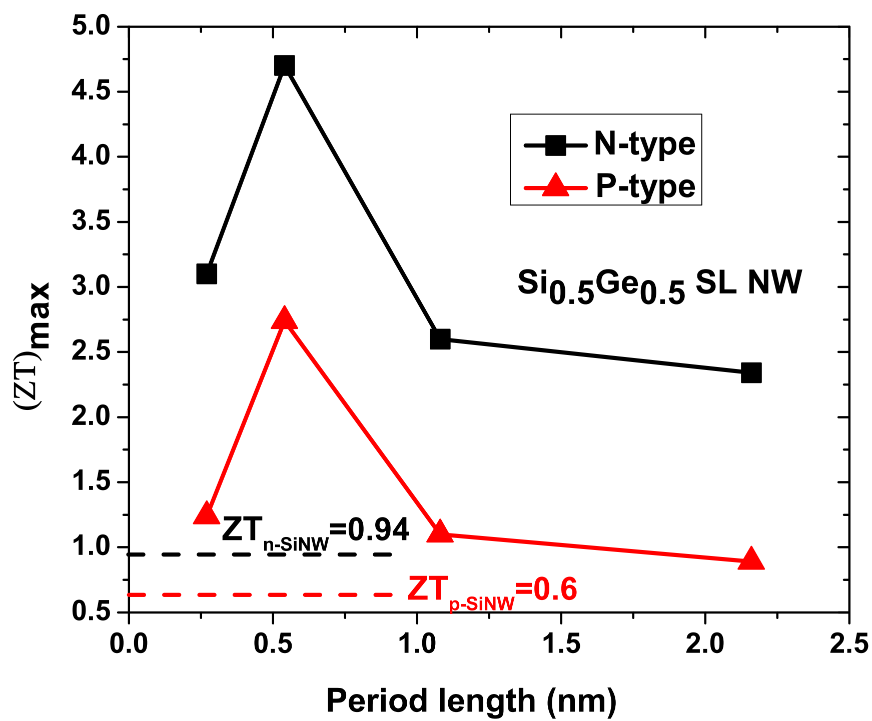

Figure 4.15: The maximum values of ZT (ZT_{max}) versus period length L.

maximum value of ZT_{max} at the period length $L = 0.54nm$ and then decreases with the further increases of the period length. The achieved ZT_{max} for n-type wires is about twice larger than its the p-type counterparts. Moreover, the values of ZT_{max} for SL NWs is much larger than the SiNWs. The maximum value of ZT_{max} for n-type wires is 4.7 at the periodic length $L = 0.54nm$, which is 5.0 times higher than that of n-type Si NWs ($ZT_{max} = 0.94$), while that for p-type wires is 2.7 with the same period length, which is 4.5 times larger than that of p-type Si NWs ($ZT_{max} = 0.6$).

4.2.2 Summary

In this work, we have investigated the thermoelectric properties of [001] $Si_{0.5}Ge_{0.5}$ superlattice nanowires. Our results show that for the charge(holes and electrons) transport, the transmission for the SL NWs decreases sharply compared with the perfect transmission in pure Si NWs. The thermal power factor of pure Si NWs is larger than that of the SL NWs for both p-type and n-type cases. The maximum power factor in the SL NWs increases firstly, reaches the maximum value at a period length $L = 0.54nm$ and then decreases with the further increase of the period length. For the phonon transport, the phonon thermal conductance is largely reduced in the SL NWs compared with that of the pure Si NWs. And the thermal conductance curve firstly decreases, reaches the minimum value at a period length $L = 0.54nm$, and then increases with the further increase of the period length. Compared with the phonon thermal conductance, the electronic thermal conductance is smaller. For both p-type and n-type wires, there is always an

optimal energy to achieve the maximum value of ZT. The optimal energy happens closely to the valence band and conduction band edges. The maximum value of the optimal ZT (ZT_{max}) increases firstly, reaches the maximum value of ZT_{max} at a period length $L = 0.54nm$ and then decreases with the further increase of the period length. The optimal ZT (ZT_{max}) of the SL NWs is enhanced compared with the pure Si NWs. The maximum value of the optimal ZT (ZT_{max}) found for n-type wires is 4.7, which is about 5.0 times higher than that of n-type Si NWs ($ZT_{max} = 0.94$), while for p-type wires, the achieved maximum value of ZT_{max} is 2.7, which is about 4.5 times larger than that of p-type Si NWs ($ZT_{max} = 0.6$).

Chapter 5

Conclusions and Outlook

Semiconductor nanowires have attracted board interest due to its fascinating thermoelectric applications. In my thesis, we have used the first principle method and Boltzmann transport equation (BTE) to investigate the thermoelectric properties of [110]Si NWs, [110]$Si_{1-x}Ge_x$ NWs and [0001]ZnO NWs. We have focused on the size dependent of thermoelectric properties of [110] Si NWs. The NWs with small diameter are preferred for the thermoelectric applications. We also studied the istoping effect on the thermoelectric properties of Si NWs. We have found the enhanced thermoelectric figure of merit in [110] $Si_{1-x}Ge_x$ NWs compared the pure Si NWs. Moreover, the thermoelectric properties of $Si_{1-x}Ge_x$ NWs are strongly dependent on the composition effect.

Besides the convention semiconductor nanowires, such as Si NWs and $Si_{1-x}Ge_x$ NWs, we have also investigated the thermoelectric properties of [0001]ZnO NWs.

We have focused on the impacts of the phase transition and Ga doping effect on the thermoelectric figure of merit in [0001]ZnO NWs. It is found that the thermoelectric figure of merit is dependent on the phase transition and Ga doping effect.

Finally, we have applied the density functional theory (DFT) and nonequilibrium Green's Function (NEGF) to investigate the thermoelectric properties of [001] $Si_{0.5}Ge_{0.5}$ superlattice nanowires. It is found that the thermoelectric figure of merit is largely enhanced in the SL NWs compared with that of pure Si NWs.

5.1 Conclusive Remarks

The investigation of the enhanced thermoelectricity in semiconductor nanowires were discussed in Chapter 2 to Chapter 4.

In Chapter 2, we discussed the Boltzmann Transport Equation (BTE) for diffusive regime and the semiclassical ballistic equation for ballistic regime.

The size dependent thermoelectric properties of Si NWs was studied in Chapter 3. we use the first-principles tight-binding electronic structure calculation and Boltzmann transport equation to investigate the the size dependence of thermoelectric properties of silicon nanowires(SiNWs). With cross section area increasing, the electrical conductivity increases slowly, while the Seebeck coefficient reduces

remarkably. This leads to a quick reduction of cooling power factor with diameter. Moreover, the figure of merit also decreases with transverse size. Our results demonstrate that in thermoelectric application, NW with small diameter is preferred.We also predict that isotopic doping can increase the value of ZT significantly. With 50% ^{29}Si doping ($^{28}Si^{29}_{0.5}Si_{0.5}$NW), the ZT can be increased by 31%.

Chapter 3 also studied composition effects on the thermoelectric properties of silicon-germanium $Si_{1-x}Ge_x$ nanowires (NWs). The power factor and figure of merit in n-type $Si_{1-x}Ge_x$ wires are much larger than those in their p-type counterparts with the same Ge content and doping concentration. Moreover, the maximal obtainable figure of merit can be increased by a factor of 4.3 in n-type $Si_{0.5}Ge_{0.5}$ NWs, compared with the corresponding values in pure silicon nanowires (SiNWs). Given the fact that the measured ZT of n-type SiNW is $0.6 - 1.0$, we expect ZT value of n-type $Si_{1-x}Ge_x$ NWs to be $2.5 - 4.0$.

Chapter 3 turns to consider the impacts of phase transition and Ga doping effect on the thermoelectric figure of merit in [0001] ZnO nanowires. Our results show that the electronic band gap of ZnO NWs for Wurtzite (W) phase is larger than that for Hexagonal (H) phase. For a certain carrier concentration, the Seebeck coefficient S for W-phase is larger than that for H-phase, while electrical conductivity for H Phase is much higher than that for W-Phase because of the higher electron mobility for H-Phase. There is an optimal carrier concentration to achieve the maximum value of power factor P for both W and H phases. The maximum value of P (P_{max}) for H phase ($P_{max} = 1638\mu W/m - K^2$) is larger than that of W phase ($P_{max} = 1213\mu W/m - K^2$) due to its high electrical conductivity, it is referred

that the thermal conductivity for H phase is about 20% larger than that for W phase. Combined the calculations of power factor and the thermal conductivity, the maximum achievable value of figure of merit ZT for H phase is larger than that for W phase (1.1 times).

On the other hand, we have also investigated the Ga doping effect on the thermoelectric properties of [0001] ZnO Nanowires. It is found that the thermoelectric performance of the $Zn_{1-x}Ga_xO$ NWs is strongly dependent on the Ga contents. The maximum achievable room temperature thermoelectric figure of merit in $Zn_{1-x}Ga_xO$ NW can be increased by a factor of 2.5 at Ga content of 0.04, compared with the ZT of pure ZnO NWs. Our work provides design rules for possible ZnO NW arrays based piezoelectric, optoelectronic and thermoelectric hybrid energy generator.

Finally, Chapter 4 discussed the significant enhanced thermoelectric figure of merit in [001] $Si_{0.5}Ge_{0.5}$ superlattice (SL) Nanowires (NWs). In this chapter, on the one hand, we aim to study the interface effect on the thermoelectric properties of the SL NWs. We found that for the charge(electrons and holes) transport, the optimal power factor (P_{max}) curve firstly increases, reaching the maximum value of P_{max} at a period length $L = 0.54nm$ and then decreases a bit with the further increase of the period length. For the phonon transport, the phonon thermal conductance λ_p dominates the whole conductance. The λ_p curve firstly decreases, reaching the minimum value at a period length $L = 0.54nm$ and then increases with the further increase of the period length. Furthermore, the optimal thermoelectric figure of merit ZT (ZT_{max}) curve firstly increases, reaching the maximum value of ZT_{max} at the period length $L = 0.54nm$ and then decreases with the further increase of

the period length. The value of ZT_{max} in n-type wires is larger than its p-type counterparts.

On the other hand, we would like to compare both the charge transport and phonon transport of the SL NWs with that of pure Si NWs. For the charge transport, the optimal thermal power factor (P_{max}) of pure Si NWs is larger than that of the SL NWs, while for the phonon transport, the thermal conductance of pure Si NWs is much larger than that of the SL NWs. Therefore, combing both charge transport and phonon transport, the maximum value of ZT_{max} achieved in n-type wires is 4.7, which is about 5.0 times larger than that of n-type pure Si NWs ($ZT_{max} = 0.94$) and that in p-type wires is 2.7, which is about 4.5 times higher than that of p-type pure Si NWs ($ZT_{max} = 0.6$).

According to the above works I have done, it is evident to conclude that semiconductor nanowires are good candidates for the thermoelectric applications. On the one hand, the smaller NWs are preferred for the achieved high thermoelectric figure of merit ZT. On the other hand, doping is a good way to improve the thermoelectric figure of merit ZT.

5.2 Outlook to Future Research Perspective

I dedicated myself into the investigation of improvement of the thermoelectric figure of merit ZT in semiconductor nanowires throughout my Ph. D. candidature,

with the collaborations of my colleagues, investigations of the improvement of thermoelectric figure of merit ZT in nanowires has not come to an end. Nevertheless, based on my currently obtained results and the methods adopted in my works, there are several directions still open and worthwhile for further studies.

5.2.1 The Phonon-Drag Effect on Thermoelectric Figure of Merit in Semiconductor Nanowires

In recent experiment [15], the phonon-drag effect is considered as a key point for improving the thermoelectric figure of merit ZT. In their work, it is shown that the phonon-drag effect can contribute to the Seebeck coefficient, thus improving the value of ZT. The enhancement of phonon-drag thermopower is found in bilayer graphene[111] and single-layer graphene[112]. Under the condition that at very low temperatures and weakly doped, the phonon-drag thermopower would be significant. In ref [111], at temperatures $T > 10K$, the contribution to thermopower mainly comes from diffusive process and the phonon-drag effect can be ignored, while at very low temperatures $T < 10K$, a phonon-drag peak from phonon-phonon scattering in the temperature dependence of thermopower is found.

As early as in the year 1954, Herring's formulas [113] was used to study the phonon-drag thermopower in $3D$ materials, however, this formulas is so simple that it could not describe $2D$ and $1D$ cases. D.G. Cantrell and P.N. Butcher have successfully proposed a theoretical model to investigate the phonon-drag thermopower in $2D$ electron gas [114] and $1D$ materials [115, 116]. In our future work, we will use

Cantrell-Butcher's theorem to study the phonon-drag thermopower in semiconductor nanowires.

Bibliography

[1] G.S. Nolas, J. Sharp, and H. Goldsmid, *Thermoelectrics: Basic Principles and New Materials Developments*, Springer, New York,(2001).

[2] D. Rowe, ed., *Thermoelectrics Handbook: Macro to Nano*, CRC Press, Boca Raton, (2006).

[3] A. J. Minnich, M. S. Dresselhaus, Z. F. Ren and G. Chen, *Energy Environ. Sci.*, **2**,466C479 (2009).

[4] L. D. Hicks and M. S. Dresslhaus, *Phys. Rev. B***47** 12727 (1993).

[5] H. J. Goldsmid, *Thermoelectric Refrigeration*, Plenum Press, New York 1964.

[6] Majumdar, A. *Science*, **303** 777(2004).

[7] S. G. Volz and G. Chen, *Appl. Phys. Lett.*, **75**, 2056 (1999)

[8] S. G. Volz and G. Chen, *Phys. Rev. B: Condens. Matter Mater. Phys.*, **61**, 2651 (2000).

[9] D. Li, Y. Wu, P. Kim, L. Shi, P. Yang and A. Majumdar, *Appl. Phys. Lett.*, **83**, 2934 (2003).

[10] N. Mingo, L. Yang, D. Li and A. Majumdar, *Nano Lett.*, **3**, 1713 (2003).

[11] Z. Zhong, X. Wang and J. Xu, Numer. *Heat Transfer, Part B*, **46**, 429 (2004).

[12] D. Li, Y. Wu, R. Fan, P. Yang and A. Majumdar, *Appl. Phys. Lett.*, **83**, 3186 (2003).

[13] L. H. Liang and B. Li, *Phys. Rev. B: Condens. Matter Mater. Phys.*,**73**, 153303 (2006).

[14] Hochbaum, A. I.; Chen, R.; Delgado, R. D.; Liang, W.; Garnett, E. C. Najarian, M.; Majumdar, A.; Yang, P. *Nature* **451**, 163 (2008)

[15] Boukai, A. I.; Bunimovich, Y.; Tahir-Kehli, J.; Heath, J. R. *Nature* **451**, 168 (2008).

[16] D. Donadio and G. Galli, *Phys. Rev. Lett*, **102**, 195901 (2009).

[17] C. Chiritescu, D. G. Cahill, N. Nguyen, D. Johnson, A. Bodapati, P. Keblinski and P. Zschack, *Science*, **315**, 351 (2007).

[18] N. Yang, G. Zhang and B. Li, *Nano Lett.*, **8**, 276 (2008).

[19] J.-W. Jiang, J.-S. Wang and B. Li, *Phys. Rev. B: Condens. Matter Mater. Phys.*, **79**, 205418 (2009).

[20] T. Ouyang, Y. P. Chen, K. K. Yang and J. X. Zhong, *Europhys. Lett.*, **88**, 28002 (2009).

[21] J. Chen, G. Zhang and B. Li, *Appl. Phys. Lett.*, **95**, 073117 (2009).

[22] J. Sootsman, H. Kong, C. Uher, J. DAngelo, C. I. Wu, T. Hogan, T. Caillat and M. Kanatzidis, *Angew. Chem., Int. Ed.*, **47**,8618(2008).

[23] *Electron-phonon Interaction in Low-dimensional structures*, Lawrence Challis (2003).

[24] J. M. O. Zide, D. Vashaee, Z. X. Bian, G. Zeng, J. E. Bowers, A. Shakouri and A. C. Gossard, *Phys. Rev. B: Condens. Matter Mater. Phys.*, **74**, 205335 (2006).

[25] J. P. Heremans, C. M. Thrush and D. T. Morelli, *Phys. Rev. B*, **70**, 115334 (2004).

[26] J. P. Heremans, C. M. Thrush and D. T. Morelli, *J. Appl. Phys.*, **98**, 063703 (2005).

[27] G. D. Mahan and J. O. Sofo, *Proc. Natl. Acad. Sci. U. S. A.*, **93**, 7436 (1996).

[28] L. D. Hicks and M. S. Dresslhaus, *Phys. Rev. B* **47**, 16631 (1993).

[29] J. P. Heremans, V. Jovovic, E. S. Toberer, A. Saramat, K. Kurosaki, A. Charoenphakdee, S. Yamanaka and G. J. Snyder, *Science*, **321**, 554 (2008).

[30] L. D. Hicks, T. C. Harman, X. Sun, M. S. Dresselhaus, *Phys. Rev. B:Condens. Matter Mater. Phys.* **53**, R10493 (1996).

[31] Y.-M. Lin, S. B. Cronin, J. Y. Ying, M. S. Dresselhaus, J. P. Heremans, *Appl. Phys. Lett.* **76**, 3944.(2000).

[32] Venkatasubramanian, R.; Siivola, E.; Colpitts, T.; OQuinn, B. *Nature* 413, 597(2001).

[33] Harman, T. C.; Taylor, P. J.; Walsh, M. P.; LaForge, B. E. *Science* **297**, 2229, (2002).

[34] T.T.M. Vo, A.J. Williamson, V. Lordi and G. Galli, *Nano Lett.* **8** (4), 1111-1114 (2008).

[35] K. F. Hsu, S. Loo, F. Guo, W. Chen, J. S. Dyck, C. Uher, T. Hogan, E. K. Polychroniadis, and M. G. Kanatzidis, *Science*, textbf303, 818 (2004).

[36] P. F. P. Poudeu, J. DAngelo, A. D. Downey, J. L. Short, T. P.Hogan, and M. G. Kanatzidis, *Angew. Chem., Int. Ed.* **45**, 3835(2006).

[37] J. R. Sootsman, R. J. Pcionek, H. Kong, C. Uher, and M. G. Kanatzidis, *Chem. Mater.* **18**, 4993 (2006).

[38] J. Androulakis, C. H. Lin, H. J. Kong, C. Uher, C. I. Wu, T. Hogan, B. A. Cook, T. Caillat, K. M. Paraskevopoulos, and M. G. Kanatzidis, *J. Am. Chem. Soc.* **129**, 9780 (2007).

[39] X. W. Wang, H. Lee, Y. C. Lan, G. H. Zhu, G. Joshi, D. Z. Wang, J. Yang, A. J. Muto, M. Y. Tang, J. Klatsky, S. Song, M. S. Dresselhaus, G. Chen, and Z. F. Ren, *Appl. Phys. Lett.* **93**, 193121 (2008).

[40] G. Joshi, H. Lee, Y. C. Lan, X. W. Wang, G. H. Zhu, D. Z. Wang, R. W. Gould, D. C. Cuff, M. Y. Tang, M. S. Dresselhaus, G. Chen, and Z. F. Ren, *Nano Lett.* **8**, 4670 (2008).

[41] G. H. Zhu, H. Lee, Y. C. Lan, X. W. Wang, G. Joshi, D. Z. Wang, J. Yang, D. Vashaee, H. Guilbert, A. Pillitteri, M. S. Dresselhaus, G. Chen, and Z. F. Ren, *Phys. Rev. Lett.* **102**, 196803 (2009).

[42] A. J. Minnich, H. Lee, X. W. Wang, G. Joshi, M. S. Dresselhaus, Z. F. Ren, G. Chen, and D. Vashaee, *Phys. Rev. B*, **80**, 155327 (2009).

[43] Q. Hao, G.H. Zhu, G. Joshi, X.W. Wang, A. Minnich, Z. F. Ren, and G. Chen, *Appl. Phys. Lett.* **97**, 063109(2010).

[44] J.E. Cornett and O. Rabin, *Appl. Phys. Lett.* **98**, 182104 (2011).

[45] J.H. Lee, and J. C. Grossman, *Appl. Phys. Lett.*, **95**, 013106 (2009).

[46] L. H. Shi, D. L. Yao, G. Zhang and B. W. Li, *Appl. Phys. Lett.* **95**, 063102 (2009).

[47] L. H. Shi, D. L. Yao, G. Zhang and B. W. Li, *Appl. Phys. Lett.* **96**,173108 (2010).

[48] L. H. Shi, J. Chen, G. Zhang and B. W. Li, (in submission, 2011).

[49] T. Markussen, A.-P. Jauho and M. Brandbyge, *Phys. Rev. Lett.*, **103**,055502 (2009).

[50] X. Ni, G. Liang, J.-S. Wang and B. Li, *Appl. Phys. Lett.*, **95**,192114 (2009).

[51] P. Hohenburg and W. Kohn, *Phys. Rev.* **136** B864 (1964).

[52] W. Kohn and L. J. Sham, *Phys. Rev.***140** A1133 (1956).

[53] B.L. Wang, J.J. zhao, J.M. Jia, D.N. Shi, J.G. Wan and G.H. Wang, *Appl. Phys. Lett.* **93**, 021918 (2008).

[54] Y. Zhang, Y.H. Wen, J. C. Zheng and Z.Z, Zhu, *Appl. Phys. Lett.* **94**, 113114 (2009).

[55] A. J. Kulkarni and M. Zhou, *Nanotechnology*, **18**, 435706 (2007).

[56] Y. Ma, Q. Hao, B. Poudel, Y. C. Lan, B. Yu, D. Z. Wang, G. Chen, and Z. F. Ren, *Nano Lett.* **8**, 2580 (2008).

[57] Y. Cui, Q. Q. Wei, H. K. Park, and C. M. Lieber, *Science* **293**, 1289 (2001).

[58] Y. Cui and C. M. Lieber, *Science* **291**, 851 (2001).

[59] D. Yao, G. Zhang, and B. Li, *Nano Lett.* **8**, 4557 (2008).

[60] D. D. D. Ma, C. S. Lee, F. C. K. Au, S. Y. Tong, and S. T. Lee, *Science*, **299**, 1874 (2003).

[61] M. Nolan, S. OCallaghan, G. Fagas, and J. C. Greer, *Nano Lett.* **7**, 34 (2007).

[62] G. Zhang and B. Li, *J. Chem. Phys.* **123**, 114714 (2005).

[63] C. W. Chang, D. Okawa, H. Garcia, A. Majumdar, and A. Zettl, *Phys. Rev. Lett.* **101**, 075903 (2008).

[64] R. Y. Wang, J. P. Feser, J.-S. Lee, D. V. Talapin, R. Segalman, and A. Mujumdar, *Nano Lett.* **8**, 2283 (2008).

[65] J. P. Dismukes, L. Ekstrom, E. F. Steigmeier, I. Eudman, and D. S. Beers, *J. Appl. Phys.* **35**, 2899 (1964).

[66] C. B. Vining, *J. Appl. Phys.* **69**, 331 (1991).

[67] G. A. Slack and M. A. Hussain, *J. Appl. Phys.* **70**, 2694 (1991).

[68] O. Yamashita and N. Sadaromi, *Jpn. J. Appl. Phys.*, **Part 1 38**, 6394 (1999).

[69] Z.L. Wang et al. *Science*, **312**, 242 (2006).

[70] M.H. Huang et al. *Science* **292**, 1897 (2001).

[71] H. Cao, J.Y. Xu, D.Z. Zhang, S-H Chang, S.T. Ho, E.W. Seelig, X. Liu and R.P.H. Chang, *Phys. Rev. Lett.*, **84**, 5584 (2000).

[72] D.M. Bagnall et al. *Appl. Phys. Lett.*, **70**, 2230 (1997).

[73] C.H. Lee, G.C. Yi, Y. M. Zuev and P. Kim, *Appl. Phys. Lett.* **94**, 022106 (2009).

[74] M. Ohtaki, K. Araki and K. Yamamoto, *J. Elec. Mater.*, **38**, 1234 (2009).

[75] E. Guilmeau, A. Maignan and C. Martin, *J. Elec. Mater.*, **38**, 1104(2009).

[76] C.K. Ghosh, S. Das and K. K. Chattopadhyay, *Phys. B*, **399** 38-46 (2007).

[77] H. Xu, A. L. Rosa, T. Frauenheim, R. Q. Zhang and S.T. Lee, *Appl. Phys. Lett.* **91**, 031914 (2007).

[78] Y. Zhang, Y.H. Wen, J. C. Zheng and Z. Z. Zhu, *Appl. Phys. Lett.* **94**, 113114 (2009).

[79] H. Xu, W. Fan, A. L. Rosa, R. Q. Zhang and T. Frauenheim, *Phys. Rev. B* **79**, 073402 (2009).

[80] W. Fan, H. Xu, A. L. Posa, T. Frauenheim and R. Q. Zhang, *Phys. Rev. B,* **76**, 073302 (2009) .

[81] R. Q. Zhang, Y. Lifshitz, D. D. D. Ma, Y. L. Zhao, T. Frauenheim, S. T. Lee, and S. Y. Tong, *J. Chem. Phys.* **123**, 144703 (2005).

[82] M. Elstner, D. Porezag, G. Jungnickel, J. Elsner, M. Haugk, T. Frauenheim, S. Suhai, and G. Seifert, *Phys. Rev. B* **58**, 7260 (1998).

[83] T. Frauenheim, G. Seifert, M. Elstner, Z. Hajnal, G. Jungnickel, D. Porezag, S. Suhai, and R. Scholz, *Phys. Status Solidi B* **217**, 41 (2000).

[84] D. Yao, G. Zhang, and B. Li, *Appl. Phys. Lett.* **94**, 113113 (2009).

[85] C. Jacoboni, C. Canali, G. Ottaviani, and A. A. Quaranta, *Solid-State Electron.* **20**, 77 (1977).

[86] T. E. Humphrey and H. Linke, *Phys. Rev. Lett.* **94**, 096601 (2005).

[87] G. Zhang, Q. X. Zhang, C. T. Bui, G. Q. Lo, and B. Li, *Appl. Phys. Lett.* **94**, 213108 (2009).

[88] X. Fan, G. Zeng, C. Labounty, J. E. Bowers, E. Croke, C. C. Ahn, S. Huxtable, A. Majumdar, and A. Shakouri, *Appl. Phys. Lett.* **78**, 1580 (2001).

[89] Y. Zhang, J. Christofferson, A. Shakouri, G. Zeng, J. E. Bowers, and E. T. Croke, *IEEE Trans. Compon. Packag. Technol.* **29**, 395 (2006).

[90] *Thermoelectrics Handbook Macro to Nano*, edited by D. M. Rowe (Taylor Francis, London, 2006).

[91] P. K. Schelling, S. R. Phillpot, and P. Keblinski, *Phys. Rev. B* **65**, 144306 (2002).

[92] L. H. Liang and B. Li, *Phys. Rev. B* **73**, 153303 (2006).

[93] B. Delley, *J. Chem. Phys.* **92**, 508 (1990).

[94] J. P. Perdew, K. Burke, and M. Ernzerhof, *Phys. Rev. Lett.* **77**, 3865 (1996).

[95] J.-E. Yang, C.-B. Jin, C.-J. Kim, and M.-H. Jo, *Nano Lett.* **6**, 2679 (2006).

[96] G. Zhang and C. B. Musgrave, *J. Phys. Chem. A* **111**, 1554 (2007).

[97] L. Bertini and C. Gatti, *J. Chem. Phys.* **121**, 8983 (2004).

[98] F. Cargnoni, E. Nishibori, P. Rabiller, L. Bertini, G. J. Snyder, M. Christensen, C. Catti, and B. B. *Iversen, Chem.-Eur. J.* **10**, 3861 (2004).

[99] D. Wolf, P. Keblinski, S. R. Phillpot and J. Eggebrecht, *J. Chem. Phys.*, **110**, 8254 (1999).

[100] R. P. Wang, A. W. Sleight and D. Cleary, *Chem. Mater.*, **8**, 433-439 (1996).

[101] K. Ellmer and R. Mietus, *Thin Solid Films,* **516**, 4620-4627 (2008).

[102] C. Y. Ren, S. H. Chiou, and C. S. Hsue, *Phys. B* **349**, 136-142 (2004).

[103] M. Snure and A. Tiwari, *J. Appl. Phys.* **101**, 124912 (2007).

[104] D. R. Khanal, J.W. L. Yim, W. Waluwicz and J. Wu, *Nano Lett.* **7**, 1186-1190 (2007).

[105] Y. Wu, R. Fan, and P. Yang, *Nano Lett.* **2**, 83 (2002).

[106] M. S. Gudiksen, L. J. Lauhon, J. Wang, D. C. Smith, and C. M. Lieber, *Nature* (London) **415**, 617 (2002).

[107] M.T. Bjork, B.J. Ohlsson, C. Thelander, A.I. Persson, K. Deppert, L.R. Wallenberg, and L. Samuelson, *Appl. Phys. Lett.* **81**, 4458(2002).

[108] Y. M. Lin and M. S. Dresselhaus, *Phys. Rev. B*, **68**, 075304 (2003).

[109] T. Markussen, A. P. Jauho and M. Brandbyge, *Phys. Rev. B*, **79**, 035415 (2009).

[110] T. Markussen, A. P. Jauho and M. Brandbyge, *Phys. Rev. Lett*, **103**, 055502 (2009).

[111] S.S, Kubakaddi and K.S. Bhargavi, *Phys. Rev. B*, **82**, 155410 (2010).

[112] W.S. Bao, S.Y. Liu and X.L. Lei, *J.Phys.:Condens.Matter*, **22**, 315502 (2010).

[113] C. Herring ,*The Phys. Review* **96**, 1163 (1954).

[114] D.G. Cantrell and P.N. Butcher, *J. Phys. C* **20**, 1985(1987).

[115] J. Vavro et al., *Phys. Rev. Lett.* **90**, 065503-1 (2003).

[116] Hone, et al., *Phys. Rev. Lett.* **80**, 1042 (1998).

Electrical-Thermal Energy Transfer and Energy Conversion in Semiconductor Nanowires

SHI LIHONG

NATIONAL UNIVERSITY OF SINGAPORE

2011